

Copyright
by
Corey Jason Trahan
2003

**The Dissertation Committee for Corey Jason Trahan certifies that this is the
approved version of the following dissertation:**

**Trajectory Integration of the Quantum Hydrodynamic Equations of
Motion**

Committee:

Robert E. Wyatt, Supervisor

David A. Vandebout

Dmitrii E. Makarov

Kent F. Milfeld

Philip L. Varghese

**Trajectory Integration of the Quantum Hydrodynamic Equations of
Motion**

by

Corey Jason Trahan, B.S.

Dissertation

Presented to the Faculty of the Graduate School of

The University of Texas at Austin

in Partial Fulfillment

of the Requirements

for the Degree of

Doctor of Philosophy

The University of Texas at Austin

December 2003

Dedication

This dissertation is dedicated to my mother and father for giving me both the opportunity and the confidence to achieve all my academic aspirations.

Acknowledgements

I would like to thank Robert E. Wyatt for his patience and guidance. In addition, I would like to thank Fernando Sales-Mayor, Kyungsun Na, and Keith Hughes for our many beneficial discussions concerning both science and life. I would also like to thank my two sisters, Ashley and Jerri Trahan, and Paige Oliver for your love and support. Lastly, I would like to thank the National Science Foundation and the Robert Welch Foundation for their financial support.

11/25/2003

Trajectory Integration of the Quantum Hydrodynamic Equations of Motion

Publication No. _____

Corey Jason Trahan, Ph.D.

The University of Texas at Austin, 2003

Supervisor: Robert Eugene Wyatt

Recently, in an effort to solve more realistic problems in quantum dynamics, much attention has been directed into numerically integrating the quantum hydrodynamic equations of motions (QHEM), as opposed to directly solving the time-dependent Schrödinger equation (TDSE). Such efforts have been provoked by the many numerical drawbacks encountered when solving the TDSE on a fixed-grid. In this dissertation, one trajectory method for integrating the QHEM is reviewed, and two novel trajectories methods are described. The first of these, the quantum trajectory method (QTM), was introduced in 1999 and has been used to solve many problems in quantum dynamics since then. However, severe numerical problems are encountered when this method is applied to problems that form wave function nodes. To get around this problem, new methods for numerically integrating the QHEM are needed. In the first novel method described, the arbitrary Lagrangian-Eulerian (ALE) method, particle trajectories are governed by a predetermined equation of motion that is user-supplied. The ALE method remedies inflation and compression problems encountered in the pure Lagrangian QTM.

In the second new method discussed, the derivative propagating method (DPM), single quantum trajectories can be calculated one at a time, as opposed to the ensemble propagation of the QTM and ALE method. Using these two methods, new solutions to the QHEM are obtained where the QTM fails. In addition to solving the QHEM, the DPM is also used to solve the classical Klein-Kramers equation in this dissertation. This equation governs the Markovian phase space evolution of a system coupled to an environment such as a heat bath. This marks the first time single trajectories have been used to solve both the QHEM and the Klein-Kramers equations.

Table of Contents

List of Figures	xi
Chapter 1: Introduction	1
Chapter 2: The Born-Oppenheimer Approximation and Potential Energy Surfaces	8
2.1. The Born-Oppenheimer Approximation	8
2.2. Potential Energy Surfaces	10
Chapter 3: The Quantum Hydrodynamic Equations of Motion	14
3.1. Introduction to Bohmian Mechanics	14
3.2. Derivation of the QHEM	18
3.3. The Quantum Trajectory Method (QTM)	23
3.3.1. QTM background	23
3.3.2. QTM methodology	25
3.3.2.1. Space discretization and derivative approximation	25
3.3.2.2. Time discretization and integration	28
3.3.3. QTM applications	33
3.3.3.1. The free wave packet	33
3.3.3.2. The harmonic oscillator	39
3.3.3.3. The downhill ramp	40
3.3.3.4. The Eckart barrier	49
3.3.4. QTM discussion	55
3.4. The Arbitrary Lagrangian-Eulerian (ALE) Method	56
3.4.1. ALE background	56
3.4.2. ALE methodology	57
3.4.2.1. The equidistribution method and dynamic grids	59
3.4.3. The ALE applied to an uphill ramp	68
3.4.4. ALE discussion	75
3.5. Chapter Conclusion	76

Chapter 4: The Derivative Propagating Method (DPM).....	80
4.1. DPM Background	80
4.2. Derivation of the DPM.....	81
4.3. The DPM and the QHEM	83
4.3.1. Derivation the DPM/QHEM.....	83
4.3.2. Implementation and DPM/QHEM.....	87
4.3.3. Applications of the DPM/QHEM	89
4.3.3.1. The meta-stable well.....	89
4.3.3.2. The Eckart barrier	92
4.3.4. DPM/QHEM discussion	95
4.4. The DPM and Phase Space Dynamics.....	100
4.4.1. Phase space background	100
4.4.2. The Liouville, Langevin, and Klein-Kramers equations	103
4.4.3. The DPM/KK equations of motion.....	107
4.4.4. DPM/KK applications.....	111
4.4.4.1. The damped harmonic oscillator.....	111
4.4.4.2. The meta-stable well.....	115
4.4.5. DPM/KK discussion	119
4.5. Chapter Conclusions	121

Chapter 5: Conclusions	123
Appendix A: Numerical Integration of the Time-Dependent Schrödinger Equation	128
Appendix B: The Finite Difference Method	131
Appendix C: The Moving Weighted Least Squares Method (MWLS)	134
Appendix D: Radial Basis Function Interpolation	137
Appendix E: Atomic Units	141
Appendix F: Example QTM Code	143
Bibliography	147
VITA	153

List of Figures

- Figure 2.1.** This plot displays the Morse potential for a generic diatomic molecule (in pink). The blue curve is the low-energy quadratic polynomial fit to the Morse potential. 11
- Figure 2.2.** This figure gives details on a tri-atomic chemical reaction. The most commonly used coordinate set for this problem is given in plot (a). If the reaction angle, θ , is fixed at 180° , then the potential energy surface in these coordinates is given in plot (b). Plot (c) displays the Eckart barrier, obtained by following the minimum energy path on the potential surface. 13
- Figure 3.2.** A plot of the quantum potential (a) and quantum force (b) for a free 1D wave packet. These solutions were obtained using the QTM. 38
- Figure 3.3.** This plot displays the time-evolution of the trajectory initially located at the center of the wave packet. The contour lines represent the anisotropic classical potential that guides the particle. This same trajectory was obtained when Newton's equations of motion were solved for this potential 41
- Figure 3.4.** Plot (a) displays the x -dependent oscillator trajectories at the $y = 0$ cross section. Plot (b) shows the y -dependent trajectories at the $x = 0$ cross section. Both plots were calculated using the QTM. 42
- Figure 3.5.** Plot (a) displays the x -dependent oscillator trajectories at the $y = 0$ cross section. Plot (b) shows the y -dependent trajectories at the $x = 0$ cross section. Both plots were calculated using Newton's equations of motion for the harmonic oscillator. 43
- Figure 3.6.** Downhill ramp potential energy surface and initial Gaussian wave packet position used in the second QTM application. 45

Figure 3.7. Plot (a) of this figure displays the time-dependent transmission probabilities obtained by applying the QTM to the uphill ramp problem. Four different energy wave packets were propagated. In plot (b), trajectories are plotted for the wave packet with an initial energy of 1500 cm^{-1} . 46

Figure 3.8. The time-dependence of the quantum potential for the downhill ramp. 48

Figure 3.9. The Eckart barrier potential and initial Gaussian used in the last QTM application. 51

Figure 3.10. In the bottom part of this figure, QTM trajectories for the Eckart barrier problem are plotted in time until numerical breakdown occurs. At the point of breakdown, the density is plotted vs. position (the top part). The solid blue curve in the top plot is the probability density as calculated from the TDSE. The solid yellow line indicates the Eckart barrier maximum. A pseudo-node is circled in red. 52

Figure 3.11. In this figure, the region of the pseudo-node is further examined. In the top plot, a close-up on the probability density is given. The pink dots indicated values obtained from the QTM, and the solid blue line displays results obtained from solving the TDSE. In the bottom plot, the quantum force is plotted at the same breakdown time. Here, the quantum force was calculated by integrating the TDSE. 53

Figure 3.12. Spring setup for inclusion of the minimum separation parameter, δx_{\min} . 64

Figure 3.13. An example of a monitor function, $M(x)$, and the new coordinates calculated using the spring system algorithm *with the separation parameter*. The impulses represent particle spacing. Notice that the grid points do not collapse to zero separation as $M(x)$ increases. 66

Figure 3.14. The initial Gaussian wave packet and the uphill ramp potential. 69

Figure 3.15. Transmission probabilities for the uphill ramp with four barrier heights calculated using the ALE/spring method. These values were obtained using an initial wave packet translation energy of 8000 cm^{-1} . 71

Figure 3.16. Density plots at $t = 125 \text{ fs}$ for the uphill ramp potential of maximum height 6000.0 cm^{-1} . Part (a) displays the results obtained with the ALE/spring method, while part (b) shows results obtained using the Eulerian (fixed-grid) method. The Eulerian results (solid line) were obtained using 4th order Runge-Kutta for time integration and 4th order finite differences for spatial derivatives. The circles connected by linear splines represent the results of the ALE/spring method and are the positions of the grid points at this time. 73

Figure 3.17. Density plots at $t = 110 \text{ fs}$ for the uphill ramp potential with a height of 6000 cm^{-1} . Part (a) shows the results for the ALE/spring method with 251 grid points, while part (b) displays the results for the ALE/spring method with 151 grid points. The solid line was calculated from a fixed-grid, finite difference method with 7,150 grid points. 74

Figure 3.18. A pictorial description of the hybrid method used by Wyatt and Hughes to calculate wave packet dynamics in nodal regions. Particle grid velocities calculated using the QTM were Lagrangian (QHEM), while the particles velocities inside the ψ – windows were non-Lagrangian (TDSE). 78

Figure 4.1. The cubic potential used to study the decay of a metastable state (the potential is in cm^{-1}). The initial Gaussian wave function (multiplied by 10^3 and then shifted up by 253 cm^{-1}) is also shown. 91

Figure 4.2. This figure displays the correlation function calculated at one point by the Eulerian version of the DPM for the cubic potential. The real and imaginary parts of $C(t)$ are shown by dashed and dotted lines, respectively. 93

Figure 4.3. This figure displays the correlation function for the Eckart barrier. The real part of the correlation is in red, and the imaginary part is in blue. 96

- Figure 4.4.** Energy resolved transmission probabilities for the Eckart barrier (barrier height $V_o = 3000 \text{ cm}^{-1}$). Second order (dots) and third order (dashed curve) DPM results are compared with the analytic result (solid curve). 98
- Figure 4.5.** Mean energy decay for the Klein-Kramers harmonic oscillator problem. Part (a) displays the energy decay in the low friction limit as a function of the dimensionless friction parameter γ_o , and part (b) displays the same in the high friction limit. 113
- Figure 4.6.** Density maps at four time steps for the DPM solution of the Klein-Kramers equation for a harmonic potential ($\gamma_o = 100$). 114
- Figure 4.7.** This figure displays the time decay of the probability inside the meta-stable well as a function of the dimensionless friction parameter γ_o . In the low friction limit, the decay rate is *proportional* to the friction parameter as shown in plot (a). In the high friction limit, plot (b), the decay rate becomes *inversely proportional* to γ_o . 117
- Figure 4.8.** This figure displays the time evolution of a phase space Gaussian wave packet in a meta-stable well. The Gaussian is coupled to a thermal bath using a dimensionless friction parameter of $\gamma_o = 10$. For these results, the DPM was used to integrate the Klein-Kramers equation. 118
- Figure 4.9.** This figure plots the rate constant against the dimensionless friction parameter for the cubic potential. The DPM results are shown by solid squares, and the continuous curve is a fit through these points. Kramers' turnover occurs around $\gamma_o = 2.5$. 120

Chapter 1: Introduction

A central goal of chemistry is to understand molecular change. How do molecules interact with each other and evolve into new chemical species? For those who study molecular dynamics, the answer to this question is the ‘holy grail’. By understanding the detailed mechanical processes that govern the dynamics of a chemical reaction, ‘controls’ can be used to suppress, enhance, or completely alter its productivity. In turn, this understanding can result in more efficient, safe, and economical methods of production. In addition to controlling the desired evolution, the study of molecular dynamics offers a refined means for learning about the behavior of the systems themselves.

In most molecular reactions, quantum mechanical effects such as tunneling, interference, and non-adiabatic excitations cannot be ignored. In fact, the study of molecular dynamics on its most fundamental level leads to the study of quantum dynamics. In quantum mechanics, the time-dependent Schrödinger equation (TDSE) is used to study the evolution of a molecular species. Unfortunately, few analytic solutions to this equation of motion are available, especially for complicated potential energy surfaces and numerous coupled degrees of freedom. Because of this, the majority of the TDSE’s solutions are obtained through numerical methods. Traditional numerical techniques involve solving the TDSE using spatial grids (see Appendix A), basis sets, or combinations thereof. This is followed by the use of efficient propagation methods, such as expansions of the evolution operator in Chebyshev or other special functions. The multi-configurational time-dependent Hartree method is an example where impressive

results have been reported [1]. The efficiency and accuracy of some of these methods are compared by Truong, Lesyng, and Hoffman [2]. In addition to solving the exact quantum dynamics of a system, semi-classical methods [3] continue to receive considerable attention. Despite many recent advances in theoretical and numerical approaches, the current state-of-the-art full-dimensional quantum mechanical calculations have only been performed for up to four-atom systems. This is in contrast to classical methods of molecular dynamics, which are applicable to large-scale molecular reactions. The difference between the two is the equation of motion solved. In classical mechanics, Newton's equations of motion are solved, and single trajectories are evolved independently without requiring information from surrounding particles. These particles evolve according to a preassigned potential energy function. On the other hand, when solving the TDSE, single trajectories cannot be calculated so easily, since this equation has a nonlocal kinetic energy term that requires simultaneous information from surrounding particles. When propagating Newton's equations, the computational storage and CPU time scale linearly with the system's dimensionality. When solving the TDSE, the storage and CPU time scale exponentially with the system's dimensionality. Because of this scaling and the importance of quantum effects, there is motivation to discover alternative numerical methods for solving problems in quantum dynamics.

Over the past several years, computational approaches based upon the hydrodynamic formulation of quantum mechanics have been actively pursued. In this new formalism, two coupled nonlinear partial differential equations (PDE) governing the evolution of the wave function amplitude and phase are used. This is in contrast to evolving the complex wave function with the TDSE. These equations of motion are

called the quantum hydrodynamic equations of motion (QHEM), and were first introduced by Madelung [4], de Broglie [5], Takabayasi [119], and Bohm [6]. The QHEM are derived directly from the TDSE, and their solutions are equivalent to it. Because of its numerous advantages over the TDSE (these will be discussed in Chapter 3), many recent efforts have been focused on developing robust algorithms for numerical integration of the QHEM. Three examples of such methods are the quantum trajectory method (QTM), the arbitrary Lagrangian-Eulerian (ALE) method, and the derivative propagation method (DPM).

The first of these methods, the quantum trajectory method, was introduced by Wyatt and coworkers in 1999 [7]. (Rabitz and coworkers developed a related approach, *quantum fluid dynamics* (QFD), which was also reported in the same year [20]). In the QTM, the wave function probability density is discretized and propagated in time as a compressible fluid according to the QHEM. An ensemble of particles, each representing a possible location and momentum of the system, must be simultaneously propagated in order to evaluate the spatial derivatives in the nonlocal terms of the hydrodynamic equations of motion. The particles in this ensemble move in time according to the flow velocity of the probability fluid and are called fluid elements. The trajectories of many of the fluid elements follow regions of significant wave function density, and computation is consequently concentrated in regions of interesting dynamics. Over the past few years, the QTM has been used to solve many quantum problems [7-24]. For the first half of Chapter three in this dissertation, the theory behind the QTM will be discussed and four of its applications will be reviewed. Using these applications, the advantages and disadvantages of this method will be described.

In order to remedy some of the inadequacies of the QTM, the arbitrary Lagrangian-Eulerian method was introduced as another method for integrating the QHEM in 2002 [25-28]. This numerical scheme is quite similar to the QTM, only instead of propagating the QHEM in the Lagrangian frame, the particle velocities in the ensemble are governed according to a user-defined equation of motion. This velocity guidance equation is completely arbitrary and can, for example, be used to guide the particles according to the evolving hydrodynamic fields. Although this method has only been applied to a few problems, the results obtained with ALE method are very promising. The second half of Chapter three is devoted to the theory and applications of this method.

The third and most recent method for numerically integrating the QHEM is the derivative propagating method. This method was recently developed by Trahan, Hughes, and Wyatt in 2003 [29] and then later used by Bittner in combination with the initial value representation [30]. In the DPM, equations of motion for the spatial derivatives that appear in the QHEM are derived, and these derivatives are propagated along quantum trajectories concurrently with the hydrodynamic fields themselves. The various orders of derivatives are coupled together in an infinite hierarchy, but low order truncations of this set leads to useful and relatively accurate approximations. An enormous benefit of the DPM is that single quantum trajectories may be propagated instead of ensembles, and fitting is no longer required to compute the spatial derivatives needed to integrate the equations of motion. This, in turn, can lead to a reduction in CPU time. Because this method was developed very recently, it has only been applied to the

QHEM for a few problems. In the first half of Chapter four, the theory and methodology of the DPM is discussed, and it is used to solve the QHEM for two chemical problems.

One attribute of the DPM is that it is not limited in application to the QHEM. In fact, it will be shown that the DPM can be applied to any evolutionary partial differential equation (PDE), as long as its solutions are not highly oscillating functions in space or time. In the second half of Chapter four, the DPM is used to obtain solutions to a completely different initial value PDE. In these sections, the DPM is used to obtain trajectory solutions for the classical Klein-Kramers (KK) equation. This equation governs the deterministic Markovian evolution of a phase space distribution for a subsystem in contact with an environment, the heat bath, which is maintained at some equilibrium temperature. In these sections, a brief introduction of phase space is given, and the DPM is used to obtain solutions to the KK equation for the relaxation of an oscillator in contact with a thermal bath and for the decay of a meta-stable state.

In each of these applications, quantum mechanical Gaussian wave packets are used as the initial wave function amplitude (or probability distribution in the KK problem). These packets are frequently used to model a free particle with a finite uncertainty in both position and momentum. (In a given experiment there is probably some idea of where the particle is and how fast it is moving.) The numerical propagation of these wave packets can yield considerable insight into many chemical problems, such as reactive scattering, photodissociation, electronic nonadiabatic dynamics, and the overall field of femtochemistry [31]. Mathematically, the free particle wave packet is created by superimposing plane waves of different frequencies (or momenta) using a Fourier transform. These plane waves destructively and constructively interfere so that

the wave function becomes localized in one region of space. In the laboratory, nonstationary wave packets can now be created and observed using femtosecond laser pulses. Recently, controls have been used to modify the initiation and observation of these quantum wave packets in molecular systems. In these experiments, a laser pulse can be used to control a quantum system's degrees of freedom. When a laser pulse is used to control a molecule, for example, the electromagnetic field may drive electronic excitations through a dipole interaction. These excitations may be transferred to the molecule's vibrational or rotational degrees of freedom. In this manner, techniques such as 'pump-probe' spectroscopy can be used to direct the products into a desired chemical species. Although these methods are only in their infancy, the number of successful experiments using femtosecond pulses to create and control quantum mechanical wave packets is on the rise. Ideally, computer simulations of wave packet dynamics should be used to guide experimental procedures, since this may be much less expensive.

The purposes of this dissertation are to review the QTM and to describe and apply the newly developed ALE method and the DPM. All three of these methods will be used to simulate the evolution of nuclear wave packets. The overall goal is to develop a numerical algorithm that will robustly solve the nuclear dynamics of any multi-dimensional quantum problem. This is indeed a difficult objective to accomplish, due to the aforementioned scaling problems encountered in the TDSE (and to a much lesser extent, the QHEM). Nevertheless, with the computational advancements that are being made today and a successful numerical algorithm that can alleviate the scaling dilemma, it is a goal that may be attained.

Before further discussing these three methods in detail, an appropriate way to simplify the full molecular Schrödinger equation must be given. Chapter two of this dissertation reviews the adiabatic and Born-Oppenheimer approximations. These approximations are used to separate the full quantum Hamiltonian into its nuclear and electronic parts. This is an important approximation, unless one intends to solve for the electronic and nuclear degrees of freedom simultaneously! In addition to this, chapter two also reviews some of the most widely used potential energy surfaces. These surfaces will be used as tests problems for the three methods discussed.

Chapter 2: The Born-Oppenheimer Approximation and Potential Energy Surfaces

2.1. THE BORN-OPPENHEIMER APPROXIMATION

The full non-relativistic Hamiltonian for a molecule can be written as a sum of five terms,

$$\hat{H} = -\frac{\hbar^2}{2m} \sum_i \nabla_i^2 - \sum_A \frac{\hbar^2}{2M_A} \nabla_A^2 - \sum_{A,i} \frac{Z_A e^2}{\vec{r}_{A,i}} + \sum_{A>B} \frac{Z_A Z_B e^2}{\vec{R}_{A,B}} + \sum_{i>j} \frac{e^2}{\vec{r}_{i,j}}, \quad (2.1)$$

where i, j refer to the molecules electrons and A, B refer to the nuclei. This can be written in more compact operator notation as

$$\hat{H} = \hat{T}_N(\vec{R}) + \hat{T}_e(\vec{r}) + \hat{V}_{e,N}(\vec{r}, \vec{R}) + \hat{V}_{N,N}(\vec{R}) + \hat{V}_{e,e}(\vec{r}), \quad (2.2)$$

where \vec{R} is the set of nuclear coordinates and \vec{r} is the set of electronic coordinates. A general method for solving multi-dimensional differential equations such as the TDSE is to separate the solution into product functions, isolating uncoupled degrees of freedom. This procedure greatly simplifies the process of obtaining both analytical and numerical solutions to complicated equations of motion. Unfortunately, the $\hat{V}_{e,N}(\vec{r}, \vec{R})$ terms prevent separation in the solution of the above Hamiltonian. If the coupling terms are absent, however, the Schrödinger equation can be separated, and the molecular wave function can be written as a product of its nuclear and electronic components, $\Psi(\vec{r}, \vec{R}) = \chi(\vec{r})\psi(\vec{R})$. Since these terms are generally too large to be neglected, another approximation must be made.

The most widely accepted method of separating the Schrödinger equation is the Born-Oppenheimer approximation. This approximation uses the fact that the nuclei are

much more massive than the electrons and are relatively motionless with respect to the electron's velocities. Since, within this approximation, the reaction of the electrons to any nuclear movement is nearly instantaneous, the coupling term is now *parametrically dependent* on the nuclear coordinates, $\hat{V}_{e,N}(\vec{r};\vec{R})$. This vital feature allows a solution of the Schrödinger equation in two steps. The first step is to calculate the electronic energy for many values of the parameter \vec{R} using the electronic part of Eq. (2.2),

$$\hat{H}_{el}\chi_n(\vec{r};\vec{R}) = E_n\chi_n(\vec{r};\vec{R}), \quad (2.3)$$

where

$$\hat{H}_{el} = \hat{T}_e(\vec{r}) + \hat{V}_{e,N}(\vec{r};\vec{R}) + \hat{V}_{N,N}(\vec{R}) + \hat{V}_{e,e}(\vec{r}). \quad (2.4)$$

(note: the nuclear-nuclear repulsion term is included here though it depends only on the parametric \vec{R} value. It is sometimes neglected when solving the electronic Hamiltonian, since its effect is to only shift eigenvalues by some constant). Step two involves solving the nuclear part of the total Hamiltonian, $\hat{H}_{nuc} = \hat{T}_N(\vec{R}) + V(\vec{R})$, utilizing the electronic potential energy surface, $V(\vec{R})$, constructed from the energies E_n obtained from step one.

Simply put, both the Born-Oppenheimer approximation eliminates any coupling between the electronic eigenstates determined from Eq. (2.3). This allows for solutions of the nuclear Hamiltonian on individual potential energy surfaces. For ground states and low-energy excited states, where the energy spacing is relatively large, this is a decent approximation. However, for high-energy excited states, where the spacings are smaller,

coupling between electronic energy surfaces are likely to occur, and one must make the appropriate corrections.

For the rest of this dissertation, this approximation will be assumed and the subscripts on the nuclear Hamiltonian dropped (i.e. $\hat{H}_{nuc} = \hat{H}$). Since the focus here is on nuclear dynamics, the hereafter-utilized electronic potentials are assumed to be calculated prior via Eq. (2.3). As mentioned previously, some electronic potentials for certain models are used as “test potentials” for new numerical methods. These model potentials are typically simple in functional form and are usually only an approximate to the true potential energy surface. In the following section, some commonly used model potentials are discussed.

2.2. POTENTIAL ENERGY SURFACES

One method of approximating a potential energy surface is by fitting an analytical function (such a low order polynomial) to the discrete electronic energy data obtain from solving the \vec{R} -parametric electronic Hamiltonian. For example, the potential for a vibrating diatomic oscillator is given by a Morse potential seen in Fig. 2.1. As long as the total wave function energy is much less than the dissociation energy of the molecule, this electronic potential can be fit to a quadratic polynomial, $V(\vec{R}) = 1/2 k \vec{R}^2$, where k is the harmonic oscillator force constant.

Most of the time, multi-dimensional potential energy surfaces are required for realistic problems. In order to make numerical integration of these problems feasible,

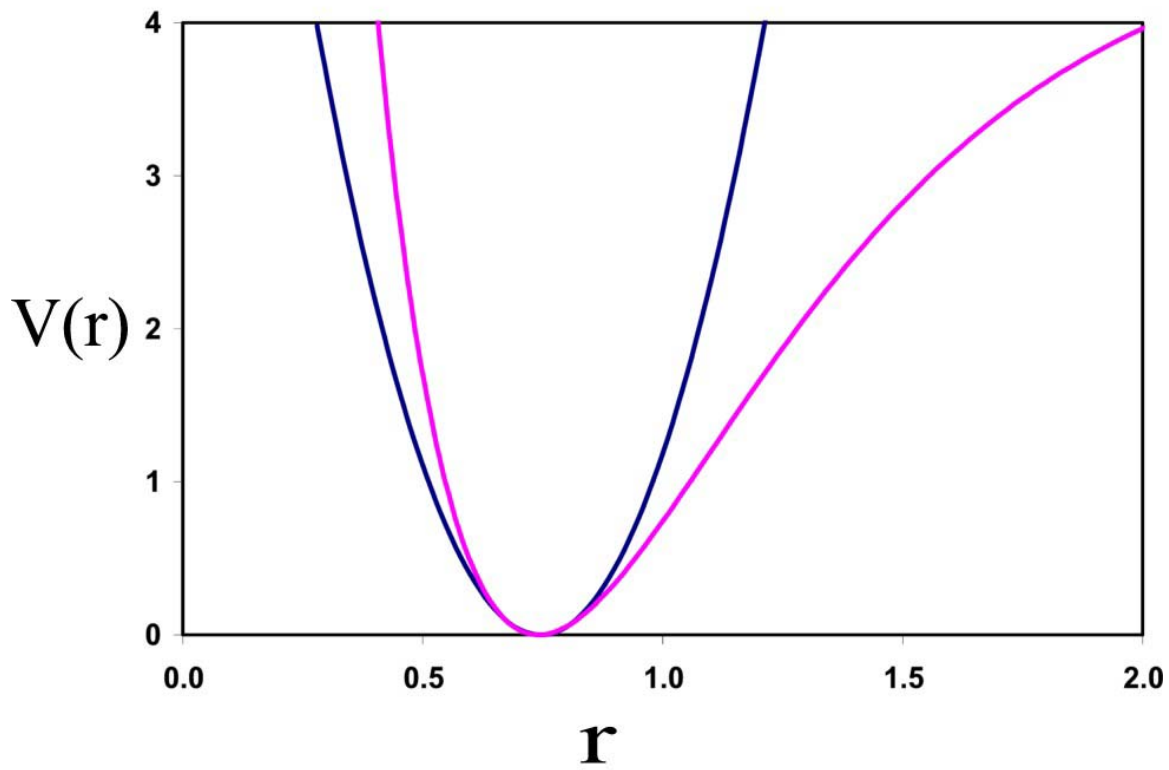


Figure 2.1. This plot displays the Morse potential for a generic diatomic molecule (in pink). The blue curve is the low-energy quadratic polynomial fit to the Morse potential.

certain degrees of freedom are frozen to reduce the dimensionality of the problem. An important example of this is the dynamics of a three-atom (A, B, and C) reaction. The most common coordinate system in this problem are R_{BC} , R_{AB} , and θ , representing the two bond lengths and the bond angle between the BC and AB bonds (see Fig. 2.2, plot (a)). The potential energy surface for the three-atom system is therefore function of three coordinates. However, if the bond angle is fixed at $\theta = 180^\circ$, the reaction is collinear, and the potential energy can be plotted as a function of two bond lengths as seen in Fig. 2.2, plot (b). An even further simplification is to follow the dynamics only along the minimum energy path (represented by the dashed line in this figure). This path is what is known as the reaction coordinate. The variation of the potential along this path is the well-known one-dimensional Eckart barrier. An example Eckart potential is displayed in Fig. 2.2, plot (c).

Many other model potential energy surfaces will be referenced throughout the remainder of this dissertation due to their simple functional form and in *some cases* their analytic solutions. Although only low-dimensional potential energy surfaces are used in this dissertation, all three of the methods discussed can be applied to problems with many degrees of freedom, though easier than others. The total dimensionality applicable for each method depends on a number of factors. Some of these include the particular potential energy surface, the method of integration itself, and of course, the computer used to solve the problem.

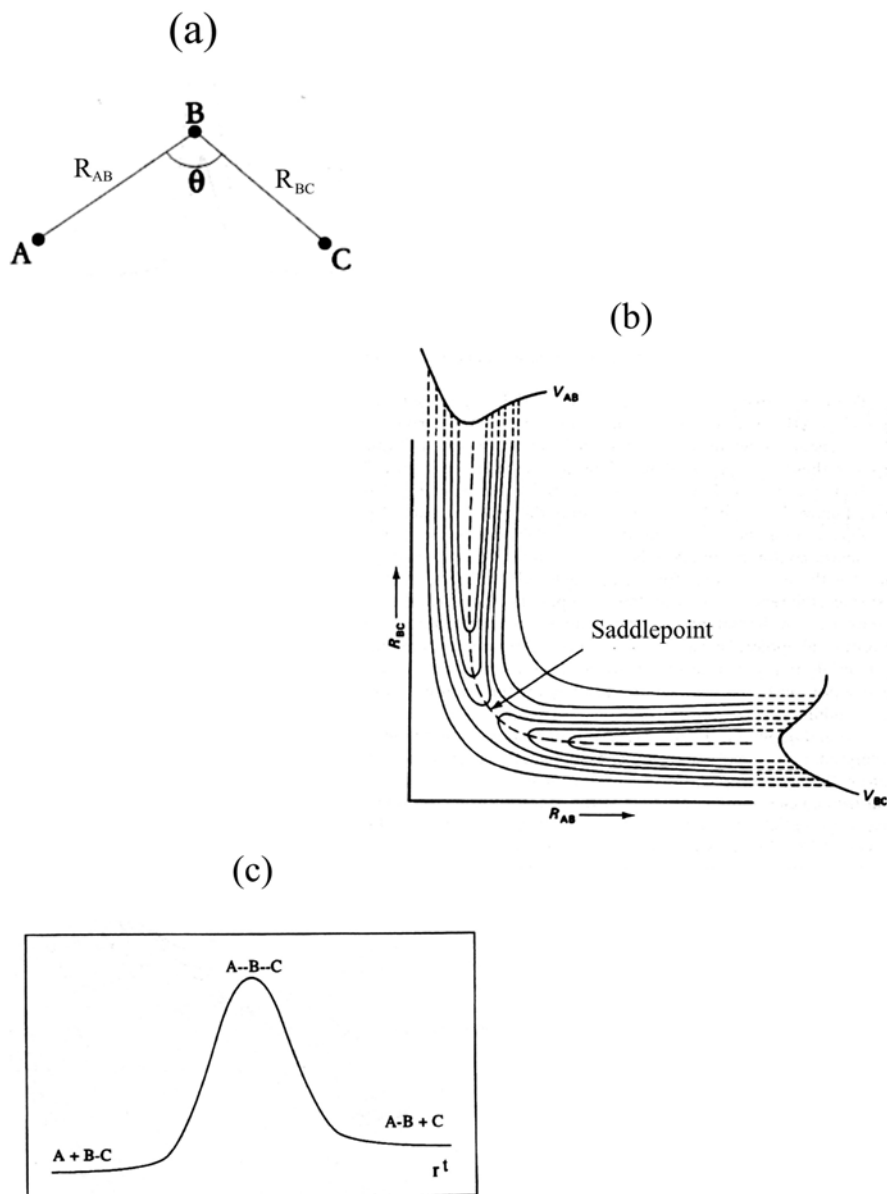


Figure 2.2. This figure gives details on a tri-atomic chemical reaction. The most commonly used coordinate set for this problem is given in plot (a). If the reaction angle, θ , is fixed at 180° , then the potential energy surface in these coordinates is given in plot (b). Plot (c) displays the Eckart barrier, obtained by following the minimum energy path on the potential surface.

Chapter 3: The Quantum Hydrodynamic Equations of Motion

3.1. INTRODUCTION TO BOHMIAN MECHANICS

Bohr once stated [32], “There is no quantum world, there is only an abstract quantum physical description. It is wrong to think the task of physics is to find out how nature is. Physics only concerns what we can say about nature.” As one of the principal founders of the Copenhagen interpretation of quantum mechanics, Bohr, along with Heisenberg and Von Neumann, assumed “completeness” of the wave function and emphasized its intrinsic indeterministic nature. By completeness, it was understood that the wave function is associated with an individual physical system and provides the most detailed and complete description of the system that is possible. This description is purely a statistical one, and the TDSE governs the dynamics of the wave function, which in turn, contains all the information needed to compute probabilities of measuring physical observables, as opposed to individual particles. Bohr recognized that if the wave function is complete, then a statistical representation of the quantum world is all there truly is. He thus believed that it is impossible to question *how nature is*, since the individual processes governing the statistics are not described by the wave function or the Schrödinger equation. After coming to this conclusion, Bohr gave up on any attempt to interpret the quantum world in a deterministic or causal way, and he believed that any attempt at doing so through the “complete” Copenhagen formulation would eventually lead to “ambiguity and confusion.”

Bohr’s completeness postulate was very controversial, however, since it took for granted the theory developed was closed and would not be advanced any further. In

addition, there was much dissatisfaction with the untraditional interpretation of such a fundamental physical theory. The problem being that many are not satisfied with simply knowing what nature can tell them in probabilities, indeed, many strive to know exactly how nature truly is. Einstein, for example, once said (as quoted by Holland [33]), “God does not play dice.” In this statement, Einstein expressed his dissatisfaction with Bohr’s elimination of determinism from fundamental physics. If the wave function is considered complete, then classical concepts such as “particles”, “trajectories”, or “forces” have no place in its interpretation, and they must be abandoned to unphysical and abstract statistical descriptions. For example, in the purely statistical representation, the term “electron” means nothing more than a mathematical function.

Instead of accepting the completeness postulate, many regard the “incompleteness” of the wave function, or its inability to describe individual processes, and they search for a causal formulation of quantum mechanics not based upon statistics or “dice”. Even today, the search for a quantum theory that can be understood from a more classical, deterministic perspective goes on, and some often turn to hidden variable and pilot wave theories for classical insight into quantum phenomenon. One of the most persistent of these theories is the de Broglie-Bohm causal hydrodynamic formulation of quantum mechanics, often called *Bohmian mechanics*.

In Bohmian mechanics the completeness postulate is discarded, and there is an attempt to delve into the heart of what governs the statistics of the Schrödinger formalism. This formalism entertains the notion that the quantum mechanical wave function is not just a statistical tool for predicting quantum outcomes, but it has a direct significance in individual processes. In fact, the statistical meaning of the wave function

can even be considered a secondary property in this approach. The fundamental ideas of Bohmian mechanics can be summarized by the following postulates [33]:

1. An individual physical system comprises a wave propagating in space and time together with a point particle, which moves continuously under the guidance of the wave.
2. The wave is mathematically described by $\psi(\vec{r}, t)$, and it is a solution to the Schrödinger equation.
3. The velocity of the particle depends on the gradient of the wave function phase, $S(\vec{r}, t)$. More specifically, the particle motion is obtained as the solution to the equation, $\dot{\vec{r}} = \vec{v} = \frac{1}{m} \vec{\nabla} S(\vec{r}, t)$. To solve this equation, initial conditions are needed (\vec{r}_o). This specification constitutes the only extra information introduced by the theory that is not contained in ψ (the initial velocity is fixed once we know S). An ensemble of possible motions associated with the same wave is generated by varying \vec{r}_o .
4. The probability that a particle in the ensemble lies between the points \vec{r} and $d\vec{r}$ at time t is given by $\psi^* \psi dr$.

In the first two postulates, the completeness of the Copenhagen interpretation is abandoned and *the particle is introduced*. The total Bohmian system now constitutes both the complex-valued wave function and the particle. The TDSE determines both the space-time dependence of the ψ -field *and* how the physical properties of the particle associated with that field evolve. In this respect, Bohmian mechanics is called a pilot

wave theory, since the wave function acts as a guide for the particle according to the dynamics of the Schrödinger equation. Because the particle moves under the guidance of the ψ -field, which is non-local by definition, Bohmian mechanics is also considered a non-local theory. This means that there is no arbitrary division into subject and object, or observer and observed. In classical mechanics, measurements can be made on a system without perturbing its state, and the system can be considered completely independent of the observer. In quantum mechanics, however, the observer plays a fundamental role in the state of the system, and any action to measure the system's properties will affect its subsequent evolution. This feature yields what Bohm called "the undivided universe". This non-locality will become more apparent when the quantum hydrodynamic equations of motion are derived later in this chapter.

In postulate three, an additional equation of motion governing the particle's trajectory in space is given. This equation is called the guidance condition and must be solved simultaneously along with the TDSE (or as will soon be shown, the QHEM). According to this condition, the particle is guided by the gradient of the wave function phase. Through this equation of motion, the particle is linked to the wave, and the two are interdependent on one another. To integrate this equation along a trajectory, initial particle positions must be given.

Within postulates 1-3, a new formalism is developed that gives further insight into our understanding of the quantum world. In this formalism, particles follow deterministic dynamics guided by the wave function. This is true, however, only if the particles described in this postulate actually do exist and have simultaneously well-defined positions and momenta. Many argue that this contradicts the Heisenberg uncertainty

principle, which states that a system is not allowed to be in a state where the momentum and position are simultaneously known, since \hat{x} and \hat{p} do not commute, $[\hat{x}, \hat{p}] \neq 0$. However, in his book, Holland [33] offers an explanation of this discrepancy. He states that quantum mechanics is constructed so that one cannot *observe* position and momentum simultaneously, but this fact does not have any bearing on whether a particle actually *exists* in a well-defined track in reality. In this respect, though one cannot make an exact measurement on a quantum trajectory, these trajectories could in fact exist in reality as “hidden variables”.

Although it is devoid of anything other than a statistical representation of the quantum world, the quantum mechanical wave function has proven to be a valuable and accurate resource for outcome predictions. Since Bohmian mechanics incorporates the Schrödinger equation and the wave function as part of its fundamental structure, it must not, and does not, violate their corresponding statistical results. Postulate four insures the compatibility of Bohmian mechanics with the statistics of the Schrödinger formalism.

3.2. DERIVATION OF THE QHEM

Inherent to Bohmian mechanics are the quantum hydrodynamic equations of motion (QHEM), derived directly from the TDSE. It is these equations that allow Bohm’s formalism to be interpreted in a classical-like manner and form the heart of the Bohmian mechanics. In this section, the QHEM will be derived and further mathematical details of the above postulates will be described. For the rest of chapter three and part of chapter four, three novel numerical integration methods will be used to solve these equations of motion.

To derive the QHEM for a particle of mass, m , in an external potential $V(\vec{r}, t)$ (this potential may be an adiabatic electronic energy surface for example), the polar form of the complex-valued wave function, $\Psi(\vec{r}, t) = R(\vec{r}, t)e^{iS(\vec{r}, t)/\hbar}$, is substituted into the time-dependent *nuclear* Schrödinger equation,

$$\left(\frac{-\hbar^2}{2m} \nabla^2 + V(\vec{r}, t) \right) \Psi(\vec{r}, t) = i\hbar \frac{\partial \Psi(\vec{r}, t)}{\partial t}, \quad (3.1)$$

and separated into real and imaginary parts. The result is the coupled pair of *nonlinear* PDEs

$$\text{(real part)} \quad \frac{\partial S(\vec{r}, t)}{\partial t} + \frac{(\vec{\nabla} S(\vec{r}, t))^2}{2m} - \frac{\hbar^2}{2m} \frac{\nabla^2 (\rho(\vec{r}, t))^{1/2}}{\rho(\vec{r}, t)^{1/2}} + V(\vec{r}, t) = 0, \quad (3.2)$$

$$\text{(imaginary part)} \quad \frac{\partial \rho(\vec{r}, t)}{\partial t} + \vec{\nabla} \cdot (\rho(\vec{r}, t) \frac{\vec{\nabla} S(\vec{r}, t)}{m}) = 0, \quad (3.3)$$

where the probability density is defined as the square of the wave function amplitude, $\rho(\vec{r}, t) = R(\vec{r}, t)^2$.

The first of the two equations is called the *quantum Hamilton-Jacobi equation* and is identical in form to its classical counterpart except for the addition of the purely quantum term

$$Q(\vec{r}, t) = -\frac{\hbar^2}{2m} \frac{\nabla^2 \{\rho(\vec{r}, t)\}^{1/2}}{\rho(\vec{r}, t)^{1/2}} = -\frac{\hbar^2}{2m} \frac{\nabla^2 R(\vec{r}, t)}{R(\vec{r}, t)}. \quad (3.4)$$

David Bohm has named this term the quantum potential [34]. To show that it is consistent to call this term a potential, the gradient operator can be applied to Eq. (3.2), and after some rearrangement, this equation can be given in Newton's form (i.e. $F = -\nabla V$),

$$\left[\frac{\partial}{\partial t} + \frac{1}{m} \nabla S \cdot \nabla \right] \nabla S = -\nabla(V + Q) = \frac{d}{dt}(m\dot{\vec{r}}). \quad (3.5)$$

Here, postulate 3 was used to relate the phase-gradients to the particle's velocity, and the total or substantial time derivative, $d/dt = \partial/\partial t + \dot{\vec{x}} \cdot \vec{\nabla}$, was substituted so that the particle now moves along a trajectory guided by the probability density flow velocity, $\dot{\vec{x}} = v(\vec{r}, t)$. (For this case, that which the speed of the particle, $\dot{\vec{x}}$, is equal to the density flow velocity, the particles are often called “fluid elements” and the associated dynamics are Lagrangian “go with the flow” dynamics. Alternative particle speeds are discussed later in the section on arbitrary Lagrangian-Eulerian dynamics.)

The quantum potential is the source of all quantum effects in Eq. (3.2), since it is the only term in this equation with an \hbar , and in the limit that $Q \rightarrow 0$, the classical Hamilton-Jacobi equation is recovered. It is a mysterious addition to the classical equations of motion, since the source of this potential is unknown. However, a few things can be deduced from its form. One important feature of Q is that it depends only on the curvature of the wave function amplitude and not on its magnitude, and therefore amplitude scaling does not alter it. This means that a particle does not respond to the intensity of the wave in its vicinity, but instead on its form. Because of this, the quantum potential can have a complicated structure in regions where the wave function amplitude becomes insignificant. Also imbedded in this term, due to its R -field second order spatial derivative, is a mathematical representation of the non-locality intrinsic in Bohmian mechanics. Derivatives are non-local by nature, and whenever they are present in an equation of motion, the solutions at discrete points are allowed to “interact” or

“communicate” with one another through these terms. Particles can, for example, borrow energy from one another to surmount otherwise insurmountable potential energy barriers. (Such is the Bohmian mechanics explanation of how quantum tunneling occurs in some systems [13]). It should be noted that because of this non-local “borrowing”, some system properties, such as energy in the tunneling example, are not conserved along a particular Bohmian trajectory, as they would be classically. Instead, these properties are only globally conserved. Another feature of the quantum potential is that it is not a preassigned function of the coordinates and does not remain separated from the process it influences, such as the classical potential. As the system evolves in time, the quantum potential is aware of the wave function’s evolution and can have an infinite number of different forms for the same physical problem.

The second of the two equations obtained from separating the Schrödinger equation, Eq. (3.3), is called the *quantum continuity equation*. This equation acts to globally conserve probability density. This is an important property of Bohmian mechanics, since its equivalence to the Schrödinger formalism requires unitarity. Once again, because of the non-local spatial derivatives present in this equation, density may not be conserved along individual trajectories.

Great efforts have been focused on solving Eqs. (3.2) and (3.3) for two reasons. The first, and most important reason, is the *numerical benefit* of propagating the smooth (non-oscillating) functions R and S , as opposed to propagating the highly oscillating ψ in time. It will be shown that fitting and interpolation methods are often used to obtain spatial derivatives needed for substitution into the QHEM at each time step. These methods are much more accurate and require fewer grid points when the solutions are

smooth in space. *Generally*, R and S are a great deal smoother in time and space than ψ . Because of this, relatively low-resolution spatial grids are needed to accurately capture wave packet dynamics when solving the QHEM. This is a marvelous benefit when solutions are required for multi-dimensional, high-energy, and unbound problems.

Another numerical benefit of the solving the QHEM relies on its inherent Lagrangian framework. Because particles are not fixed in space and are able to move along with the dynamics of the wave packet, the spatial domain needed for propagation is *much smaller* than in typical Eulerian fixed-grid problems. For these algorithms (see Appendix A), a finely resolved grid or lattice must be constructed over the entire range of the wave packet propagation¹. At each time step in the Eulerian scheme, many calculations are wasted on regions where nothing interesting is happening. Because of this, the usual methods for propagating ψ are only feasible for up to four-dimensional problems. Beyond four dimensions, problems with data storage and calculation times can become overwhelming. For example, if 100 grid points are need to capture the oscillating functional form of ψ in each dimension, a 4-dimensional problem would need one-hundred million grid points! Even for today's computers, this can become quite a burden.

The second reason why efforts have been focused on solving the QHEM is that their solutions give insight into the causal dynamics of an individual system, as discussed previously. In Bohmian mechanics, classical descriptions such as “forces”, “particles”, and “trajectories” have actual physical meanings that are derived directly from the

¹ Although, some studies have incorporated grid adaptation into ψ – propagators [27].

QHEM. This is a very important contribution to our understanding of quantum mechanics, since the Schrödinger equation gives no detail on individual dynamics.

Unfortunately, few analytic solutions of the QHEM are available, and a suitable numerical algorithm must be used to solve these nonlinear equations. In 1999, the quantum trajectory method (QTM) was introduced by Loprore and Wyatt as a means for doing just this [12]. This method will now be described in detail.

3.3. THE QUANTUM TRAJECTORY METHOD (QTM)

3.3.1. QTM background

In the QTM, the continuous probability distribution $\rho(x,t)$ is space-discretized into np grid points or particles² at $t = 0$. Each particle has a mass equal to that of the system, a unique initial value location $\vec{r}_i(t=0)$, and is identified by a descriptor, $D_i(t) = \{r_i, v_i, \rho_i, S_i, etc\}$, which stores the i th state of the particle at future times. These particles can be conceived as pursuing a definite, continuous track in space and time according to the discrete version of the guidance equation given in postulate three of Bohmian mechanics,

$$\dot{\vec{r}}_i = \vec{v}_i = \frac{1}{m} \vec{\nabla} S_i(\vec{r}, t). \quad (3.6)$$

An important feature of the QTM is that upon discretization, Eq. (3.6) provides a description of an ensemble of *coupled* trajectories, each with different initial conditions.

These trajectories are coupled by the non-local quantum potential defined in Eq. (3.4).

² The terms “grid points” and “particles” will be used interchangeably throughout this dissertation. This is in contrast to “fluid element”, which is only used to describe particles moving in the Lagrangian frame of reference.

Along each particle's trajectory the density and phase are obtained by integrating the discrete, Lagrangian versions of Eqs. (3.2) and (3.3),

$$\frac{dS_i}{dt} = \frac{(\vec{\nabla}S_i)^2}{2m} + \frac{\hbar^2}{2m} \frac{\nabla^2 R_i}{R_i} - V_i = 0, \quad (3.7)$$

$$\frac{d\rho_i}{dt} = -(\vec{\nabla} \cdot \vec{v}_i)\rho_i. \quad (3.8)$$

A few remarks must be made concerning Eqs. (3.6)-(3.8). Although the phase function S_i is multi-valued, $\vec{\nabla}S_i$ is a single-valued function of position. This means, from Eq. (3.6), that the particle velocities are also single-valued, and consequently, only one trajectory can pass through a given point in space at each instant. Bohmian trajectories, therefore, cannot cross or overlap. In addition, no Lagrangian particle is allowed to pass through a wave function node (where $\psi = 0$), since at these points, the quantum potential becomes singular and the quantum forces and particle velocities are undefined. Frequently, these conditions are used to qualitatively evaluate the accuracy of a quantum trajectory algorithm. For example, if trajectories cross at some instant, then numerical errors have developed and the solution may not be reliable.

To concurrently propagate Eqs. (3.6)-(3.8), an appropriate time-integrator and a suitable method for approximating spatial derivatives from discrete data must be used. Some numerical algorithms for accomplishing both of these tasks will be presented now.

3.3.2. QTM methodology

3.3.2.1. Space discretization and derivative approximation

A key element of the QTM is accurately approximating at each time step the spatial derivatives needed in the QHEM (i.e. $\vec{\nabla}S$, $\nabla^2 R$, etc.). These derivatives must be calculated given only the discrete particle locations and their corresponding function values. *This is, by far, the most challenging facet of the QTM.* The challenge comes from estimating derivatives on the unstructured grid encountered from the Lagrangian dynamics. More specifically, in regions where the amplitude has a large curvature, the quantum potential and quantum forces can be extremely large, resulting in complicated and “stiff” particle dynamics³. These regions may form around amplitude nodes or quasi-nodes, where the wave function amplitude is either zero or approaching so. The quantum potential around these nodes can become nearly singular and is very difficult to handle numerically. Under-sampling, or *inflation* occurs in these nodal regions, since the particles are forced away from the nodes at high velocities. Ironically, these regions sometimes occur where most of the interesting quantum effects (producing interference and thus nodes) are taking place. The results of particle inflation are fitting errors that accumulate and propagate in time throughout the grid until numerical breakdown terminates the algorithm. In the opposite scenario, over-sampling or *compression* may occur in regions where the particles are forced together. The excessive clustering decreases the minimum distance between the grid points until a violation in the time-integrator stability requirement between r_{\min} and Δt can occur. Also, as the trajectories

³ The term “stiff” is used here to describe a solution that is not smooth in time. Trajectories, for example, could make hard turns or be highly oscillatory. Stiff solutions create integration problems.

are forced very close together, global errors from the time integrators and derivative approximations can ‘wash out’ grid resolution until trajectory crossing occurs, leading to numerical break down. More difficulties emerge when spatial fitting subroutines require the solution of a linear system involving collocation matrices (i.e. polynomial least squares and radial basis function interpolation). As the particle separations decrease, the collocation matrix rows/columns become numerically less independent, resulting in a poorly conditioned system of equations and unreliable derivative approximations.

One of the most widely used methods for obtaining function and derivative approximations in the QTM has been the moving weighted least squares algorithm using a local polynomial basis. In this method, like all non-local methods for derivative approximation, a stencil or small collection of data points closely surrounding the data point of interest is used. Each of the points can be weighted according to a preassigned weight function dependent on the radial distance from the point of expansion. Low order polynomials (quadratic, cubic, etc.) are fit to these stencil points so that an overall error function is minimized. After fitting, analytical derivatives are then taken of the approximate polynomial function. For further details on the method of weighted least squares, see Appendix C.

The weighted least squares method has been quite accurate for a limited number of models in the QTM (see Lopreore and Wyatt’s publications on electronic transitions with quantum trajectories [14-15], Bittner’s analysis of the double well potential [17], Wyatt and Na’s analysis of multimode subsystem-bath dynamics [10-18], and Sales-Mayor et. al. work on the molecular photodissociation [20]). However, some problems can arise while using polynomials that present possible limitations to its application.

According to Kansa [35], two drawbacks to polynomial schemes include polynomial oscillations in higher order approximations, leading to poor derivative estimates, and the slow convergence of low order polynomial approximations. Also, as the dimensionality of the model increases, the number of polynomial basis functions increases exponentially, significantly slowing down the solution of the linear system in multi-dimensional problems. Lastly, polynomial methods often give poor derivative estimates at the grid edges, since there are not outer grid points to ‘lock’ down the approximate.

Because of the difficulties associated with polynomial methods, other derivative approximation schemes have been investigated for use in the QTM. One such method includes radial basis function interpolation first investigated by Hu, Ho, and Rabitz [21] and then later studied by Trahan and Wyatt [19]. Radial basis function interpolation will be used for various applications throughout this dissertation. The details of this method are given in Appendix D. Other methods involve fitting the quantum potential to a linear combination of Gaussian functions [36-37], trial optimization of the non-classical component of the momentum operator [38], and obtaining derivatives using distributed approximating functionals [9].

In the past, to further alleviate the difficulty of obtaining accurate derivatives for substitution into the equations of motion, the function $C = \ln(R)$ has been propagated instead of the amplitude directly. This transformation can be beneficial for two reasons. First, C can sometimes be represented by low-order polynomials. For example, the typical Gaussian wave packet reduces to a quadratic polynomial if the logarithm is taken. Secondly, the range of C may be much smaller than R . For example, if R ranges from

$10^{-7} \leq R \leq 1$, the range for the C is only $-16 \leq R \leq 0$. Using the C -amplitude, the Lagrangian QHEM become

$$\frac{dC(\vec{r}, t)}{dt} = -\frac{1}{2m} \nabla^2 S, \quad (3.9)$$

$$\frac{dS(\vec{r}, t)}{dt} = \frac{1}{2m} \vec{\nabla} S \cdot \vec{\nabla} S + \frac{\hbar^2}{2m} (\nabla^2 C + \vec{\nabla} C \cdot \vec{\nabla} C) - V. \quad (3.10)$$

In Eq. (3.10), the quantum potential is the negative of the term containing \hbar . For all problems addressed in this dissertation, the amplitude will be propagated in C -space. When discussing the derivative propagating method in Chapter four, this transformation will become a necessity.

3.3.2.2. Time discretization and integration

After spatial discretization, Eqs. (3.6), (3.9), and (3.10) become a set of ordinary differential equations in time and can be numerically integrated using one of the many ODE integrators available. Five of these integrators were studied and compared to test their accuracy and time efficiency in the QTM. To do this, a symmetric 2D free Gaussian wave packet, initially of the form

$$\Psi(x, y, 0) = \sqrt{\frac{1}{2\pi\sigma^2}} \exp[i(k_x x + k_y y)] \exp\left[-\frac{1}{4\sigma}(x^2 + y^2)\right], \quad (3.11)$$

was propagated using the QTM. According to the De Broglie relation, \vec{k} in Eq. (3.11) is related to the velocity of the wave packet by $\vec{v} = \hbar\vec{k}/m$. For this free packet the following parameters were used; $m = 2000$, $v_x = v_y = 0.0045$, and $\sigma = 0.18$ (All units in this dissertation are atomic unless otherwise mentioned. Conversion to atomic units are given in Appendix E).

At each time step, the QTM solutions to the QHEM were compared to the analytical solutions for the 2D free wave packet. These analytical solutions are discussed in detail in the QTM applications section of this chapter. It will be shown that for a free wave packet, the C -amplitude and phase are quadratic at all times, and the spatial derivatives needed in both the C and S equations of motion can be exactly fit to a 2D quadratic polynomial basis. Because of this, all errors accumulated in time larger than round-off error were isolated as time-integration errors.

The accuracies of the five time integrators tested are compared in Table I. Average errors were calculated according to the equation

$$error = \frac{1}{np} \sum_{i=1}^{np} \left| e^{C(x,y,t)^{exact}} - e^{C(x,y,t)^{calculated}} \right|. \quad (3.12)$$

Also, all methods described as being implicit in Table I are only implicit in the amplitude update. The new phase, position, and velocities are obtained explicitly by the integrator labeled before the backward slash. The amplitude can be updated implicitly by evaluating $\nabla^2 S$ of Eq. (3.10) using the updated phase values. Typically, when multiple schemes are used to integrate coupled partial differential equations, the overall accuracy of the algorithm is that of the least accurate integrator. For this reason, all of the integration given in this table can be considered explicit.

Table I. A comparison of five time integrators for a 2D free wave packet.

Integration Scheme	Error*
Euler / trapezoid **	1.0078×10^{-4}
Leap Frog (multi-step) ***	2.6352×10^{-7}
4 th Order Adams-Bashforth (multi-step)	1.9777×10^{-10}
4 th Order Adams-Bashforth / Adams-Moulton (multi-step) **	1.5274×10^{-10}
4 th Order Runge-Kutta	1.7718×10^{-12}

* Errors are taken after 2500 time steps.

** These time integrators use implicit routines for amplitude update.

*** Multi-step integrators initiated with analytical solution for a free 2D wave packet.

The first time-integrator studied, the Euler/trapezoid method, was very time efficient. However, it was also the least accurate, having a truncation error of $O(\Delta t)$. In this method, an equation of motion of the form $df/dt = F(x, t; f', f'', \text{etc.})$ is discretized in time and approximated by

$$f(t + \Delta t) = f(t) + F(x, t)\Delta t. \quad (3.13)$$

Because initiating steps or intermediate steps are not needed, the Euler/trapezoid code can be executed as fast as the spatial discretization and derivative evaluations will allow. Unfortunately, very small time steps may be needed if the phase and amplitude become less smooth in time. By decreasing the time step, the time-efficiency of the Euler/trapezoid method can be compromised to the point where it could no longer be a viable integration technique. Such was the motivation for studying more accurate integration methods.

Another commonly used method of integration is the “leap frog” technique [39]. It is one of the many multi-step methods utilizing information from previous time steps to advance the solution to new times. Other examples of multi-step methods include the explicit Adams-Bashforth and implicit Adams-Moulton algorithms. Such methods are particularly attractive since a predetermined order of accuracy can be obtained by increasing the number of prior time steps used in the extrapolation. The difficulty in the multi-step methods, however, is initiating the integrator. Depending on the order of accuracy needed, a given number of steps must be initiated with the same order of accuracy by either a highly accurate one-step method, or by taking many smaller Euler steps within the given time step. In the results of Table I, the analytical time-dependent

expressions for the phase and amplitude are used to propagate the wave packet to obtain the initial time steps needed for extrapolation. According to the results obtained, the increased accuracy of the “leap frog” two-step routine over the Euler/trapezoid method is approximately three orders of magnitude. The increased accuracy is primarily due to the two-step method having a truncation error of $O(\Delta t^2)$ instead of $O(\Delta t)$. On moving from the two-step “leap frog” method to the four-step Adam’s-Bashforth/Adam’s-Moulton method, the accuracy was increased by approximately six orders of magnitude from the Euler/trapezoid method, a very dramatic improvement due to the new truncation error of $O(\Delta t^4)$. It should be emphasized that apart from initiating the above multi-step algorithms, each requires about the same propagation time as an Euler/trapezoid step.

The last numerical integration method studied was the fourth order Runge-Kutta (RK4) algorithm. Although RK4 is the least time efficient of the five methods studied, requiring four spatial derivative evaluations at each time step, it is a one-step procedure and does not need to be initiated. More importantly, RK4 is known for its robust ability to obtain accurate results for PDEs with smooth to relatively stiff solutions [39]. As can be seen from the table, RK4 produced highly accurate solutions for the free 2D wave packet. Although the results obtained using this method were the best of all the algorithms tried, it was not often used as a primary time integrator, since evaluating four spatial derivatives at each time step can become very time consuming when fitting and interpolation methods are required.

For most of the problems discussed in this dissertation, the Euler or multi-step integrators were used. When needed, Runge-Kutta methods were used to initiate the

multi-step integrators. These integrators were chosen for their relatively fast and accurate solutions. In Chapter four of this dissertation, more accurate time-integrators are needed for the derivative propagation method, and the time-adaptive Cash-Karp/Runge-Kutta method was used. In time-adaptive methods, an approximate error is calculated at the end of each time-step, and the preceding time step is chosen to reduce this error below a user-defined tolerance. For more information on the Cash-Karp/Runge-Kutta method, see Numerical Recipes in FORTRAN 90 [39].

3.3.3. QTM applications

In this section, the QTM results for four problems will be reviewed. These are the free wave packet, the harmonic oscillator, the downhill ramp, and the Eckart barrier. The first three of these examples were chosen because the solutions are smooth enough to accurately apply the QTM without significant spatial fitting errors. Excellent results for these problems have been obtained in numerous studies. The Eckart barrier example, on the other hand, gives poor QTM results. This problem will be used to point out the setbacks encountered in the QTM when nodes begin to form in the wave function amplitude.

3.3.3.1. The free wave packet

In the time-integration section, the evolution of a free 2D wave packet was used as a test. This is because the unconstrained, free translation of a particle in space is one of the most well-known and easily solved problems in quantum mechanics. Of course, analytic solutions of the QHEM for the free wave packet are known. However, before

more sophisticated potential energy surfaces are discussed, the free wave packet problem presents a good solid ground on which to make future leaps with the QTM.

The solutions to R and S are given analytically for an initial D-dimensional Gaussian distribution by

$$C(\{x_i\}, t) = -\frac{1}{2} \sum_{i=1}^D \left\{ \frac{1}{2} \ln \left[\pi \left[\sigma_i^2 + \left(\frac{t}{\sigma_i m_i} \right)^2 \right] \right] + \frac{(x_i - x_{o,i} - v_{o,i} t)^2}{\sigma_i^2 + \left(\frac{t}{\sigma_i m_i} \right)^2} \right\}, \quad (3.14)$$

$$S(\{x_i\}, t) = \sum_{i=1}^D \left\{ p_{o,i} (x_i - x_{o,i}) + \theta_i(t) + \frac{t}{2m_i} \left[\frac{(x_i - x_{o,i} - v_{o,i} t)^2}{\sigma_i^2 \left[\sigma_i^2 + \left(\frac{t}{\sigma_i m_i} \right)^2 \right]} - p_{o,i}^2 \right] \right\}, \quad (3.15)$$

with

$$\theta_i(t) = \frac{1}{2} \tan \left(-\frac{t}{\sigma_i^2 m_i} \right). \quad (3.16)$$

In the above equations, m_i , $v_{o,i}$, $p_{o,i}$, $x_{o,i}$ and σ_i are the mass, initial velocity, momentum, position, and RMS positions widths along dimension i , respectively. All units are in atomic units described in Appendix E. From Eq. (3.14) it can be seen that if the initial amplitude is a Gaussian distribution, then it remains so for all subsequent times. In addition, the C – amplitude and the phase are both quadratic functions in space for all times. According to the gradient of Eq. (3.15), the free particle velocity field, $\vec{v} = (1/m) \vec{\nabla} S(\vec{r}, t)$, is linear in space. Each of these functions can be exactly represented by D-dimensional quadratic polynomial interpolation.

In this section, the QTM will be applied to an initial 1D stationary Gaussian wave packet (i.e. $v_o = 0$). The system mass used was $m = 2000$, and the RMS width of the initial Gaussian was $\sigma = 0.18$. Since the free packet solutions are smooth in time, a relatively large time step of 1 *a.u.* was used along with an Euler time-integrator. To obtain spatial derivatives, the MWLS algorithm described in Appendix C was used with a quadratic basis set and a unitary weight matrix for exact interpolation. Figure 3.1, plot (a) displays the particle trajectories obtained using the QTM for this problem. The analytical solution to these trajectories is given by

$$x(t) = v_o t + x_o \sqrt{1 + \left(\frac{\hbar t}{2m\sigma^2}\right)^2} = x_o \sqrt{1 + \left(\frac{\hbar t}{2m\sigma^2}\right)^2}. \quad (3.17)$$

The first term on the right hand side of Eq. (3.17), $v_o t$, is the classical translation of a particle with initial conditions x_o and v_o . This term is set to zero in this problem, since the initial wave packet is at rest. The remaining term involving the square root is a result of the wave packet “spreading” in space as it evolves in time. This amplitude spreading is displayed in Fig. 3.1, plot (b). If the wave packet remains free, then it will continue to spread until it is completely delocalized. This is a well-known attribute of quantum mechanical wave packets.

To understand the origin of these mysterious (non-classical) particle accelerations leading to wave packet spreading, the free packet quantum potential is given in Fig. 3.2,

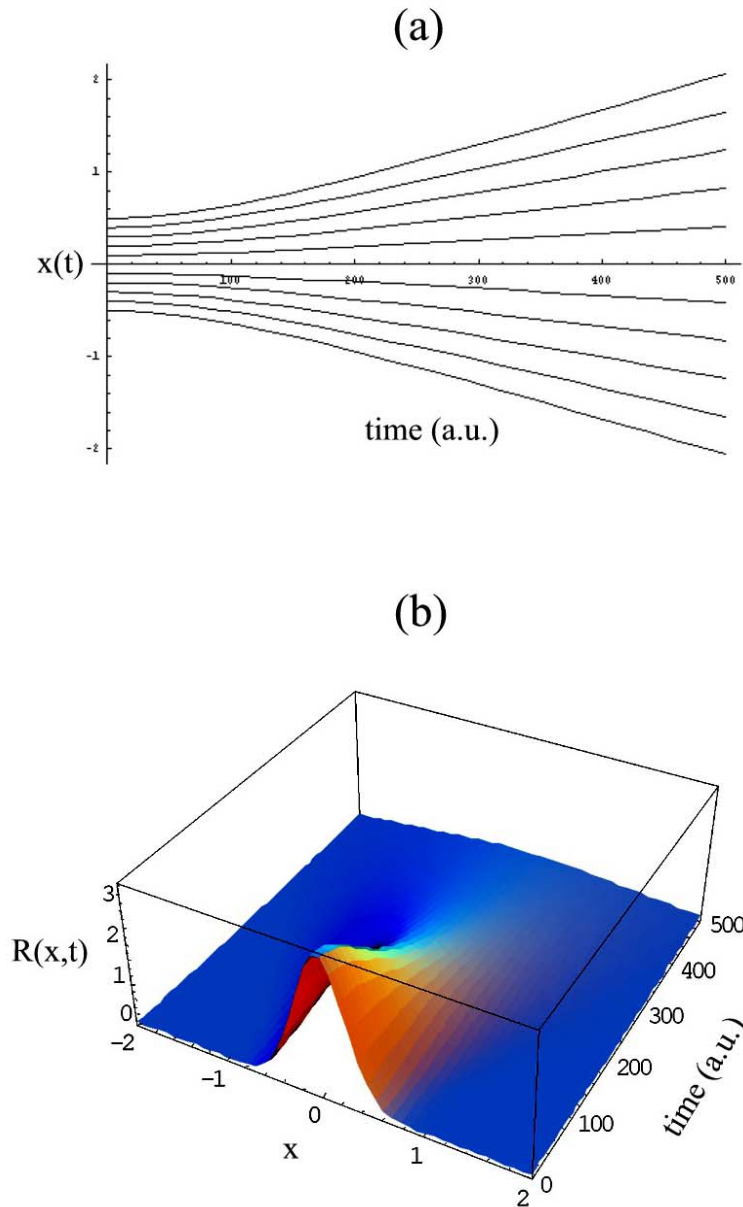


Figure 3.1. Trajectory (a) and amplitude (b) plot for a free 1D wave packet. These solutions were obtained using the QTM. (Unless otherwise stated, all units in each of the figures in this dissertation are atomic.)

plot (a). From the quantum potential, the total force acting on a particle can be obtained using

$$f_{total} = f_C + f_Q = -\frac{\partial}{\partial x}(V + Q) = -\frac{\partial Q}{\partial x}. \quad (3.18)$$

The analytical solution for the 1D free packet quantum force is given as

$$f_Q = \frac{\hbar^2}{4m\sigma^4}(x - v_0 t). \quad (3.19)$$

A plot of this function in time is given in Fig. 3.2, plot (b). In this figure, the arrows indicate the direction of the force. From Eq. (3.19) it can be seen that the magnitude of the quantum force acting on a particle at location x increases as the RMS width of the packet decreases. This means that as the wave packet spreads in space, the quantum force decreases in magnitude, as depicted in Fig. 3.2 (b). Also, according to this figure and Eq. (3.19), the quantum force is greater as the particles are positioned further away from the wave packet center. At the exact center of the wave packet, the quantum force is zero, and any motion of a particle at this location is purely classical. In this problem, the center particle is initially at rest, and because there is no classical force, it does not move in time.

It is important to note that all particle accelerations in this problem are a direct result of the quantum potential. Classically, each particle would remain at rest until acted upon by an external force. It is the quantum potential that causes the particle trajectories to diverge from one another and the wave packet amplitude to spread in space.

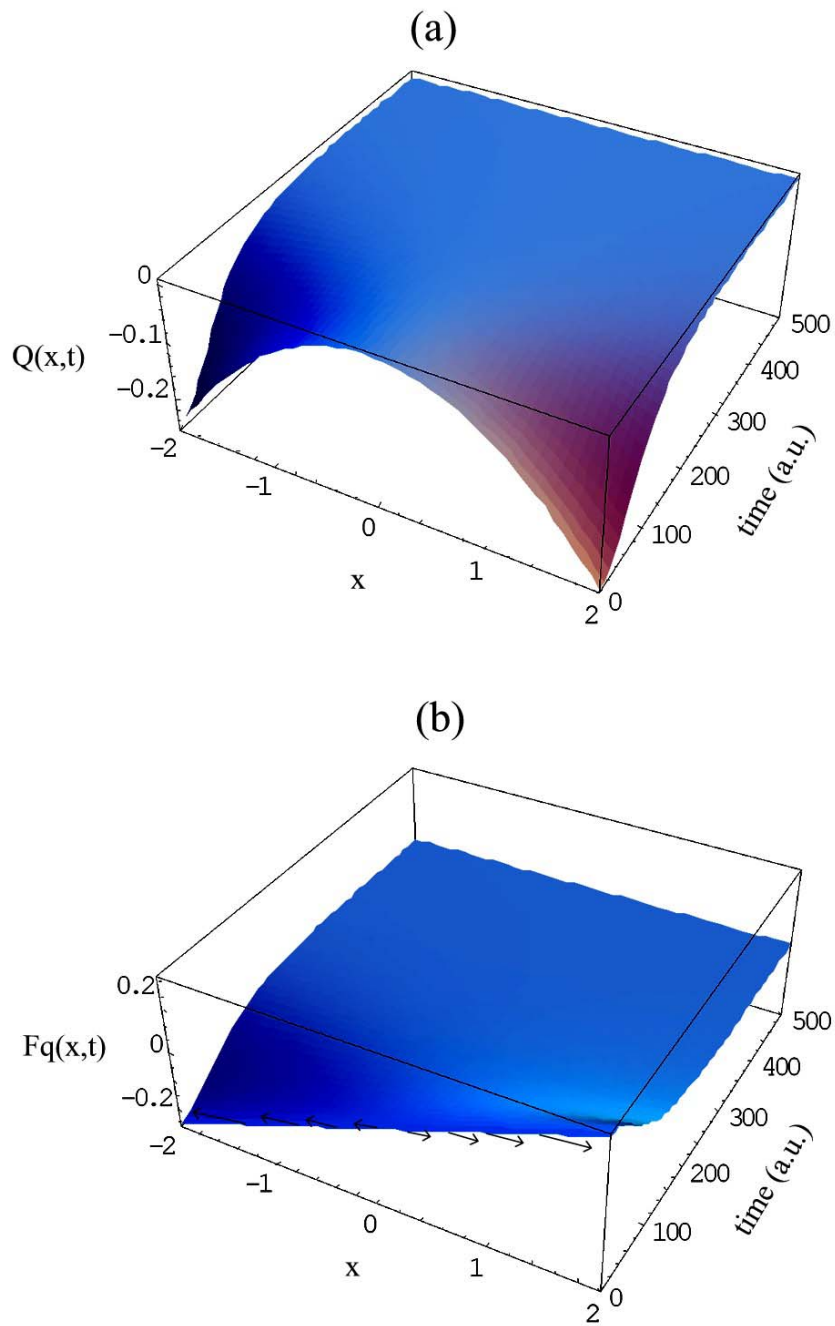


Figure 3.2. A plot of the quantum potential (a) and quantum force (b) for a free 1D wave packet. These solutions were obtained using the QTM.

3.3.3.2. *The harmonic oscillator*

For the second QTM example, a two-dimensional Gaussian wave packet was propagated inside an anisotropic harmonic oscillator potential of the form

$$V(x, y) = k_1 x^2 + k_2 y^2, \quad (3.20)$$

with force constants $k_1 = 0.009$ and $k_2 = 0.036$ (in a.u.). The wave packet was initially centered at the potential minimum $(0,0)$ and given initial velocities $v_x = 3000$ and $v_y = 5000$. The RMS widths of the initial 2D Gaussian were $\sigma_x = \sigma_y = 0.25$, and the mass of the system was set to $m = 2000$. The same time-integration and derivative approximation methods used to propagate the free wave packet were used in this problem. Once again, analytical solutions to the QHEM for this potential have been previously obtained [33].

Since, in this case, there is an external potential present, the overall force acting on the QTM particles is a combination of both the quantum and classical forces,

$$\vec{f}_{total} = \vec{f}_C + \vec{f}_Q = -\vec{\nabla}(V + Q). \quad (3.21)$$

It is well known that for this problem (as it will be for all problems with a linear or constant classical force), an initial Gaussian amplitude will remain so for all times, just as for the free packet. Consequently, the quantum potential remains parabolic, and the quantum force is a linear function equal to zero at the wave packet center. Since the classical and quantum forces for a harmonic oscillator are linear, then the total force acting on each particle is a linear function in space, just as for the free packet. Once again, the further the particles are away from the center of the packet, the greater the

quantum force acting on that particle. The center particle will again follow a purely classical trajectory, since the quantum force is zero along this path. This center-particle trajectory for this problem was calculated using the QTM and is displayed in Fig. 3.3. The same trajectory was obtained when Newton's equations of motion were solved for this anisotropic oscillator problem.

The results of the time propagation can be seen in Fig. 3.4, plots (a) and (b). In these plots, two cross-sections are shown emphasizing the anisotropic symmetry of the harmonic well. Upon comparison, the x-trajectories of the y cross-section have larger amplitudes and a shorter period than the y-trajectories of the x cross-section. This was expected since the x-width of the oscillator potential is larger than that of the y-width. An important feature of Bohmian mechanics is that trajectories are not allowed to cross. This feature can be seen by comparing the results of the QTM with those obtained classically from Newton's equations of motion (see Fig. 3.5). In the classical solution to this problem, all trajectories cross at focus points located at the peaks and troughs of the oscillations. This does not occur with the Bohmian trajectories. Also, the maximum and minimum amplitudes of the classical trajectories are significantly smaller than that of the Bohmian trajectories. This is due to the additional quantum forces acting on those particles away from the wave packet center.

3.3.3.3. *The downhill ramp*

In the third example, the QTM was used to follow the evolution of an initial 1D Gaussian wave packet on a downhill ramp potential energy surface of the form

$$V(x) = \frac{V_o}{1 + e^{-2.5(x-1)}} , \quad (3.22)$$

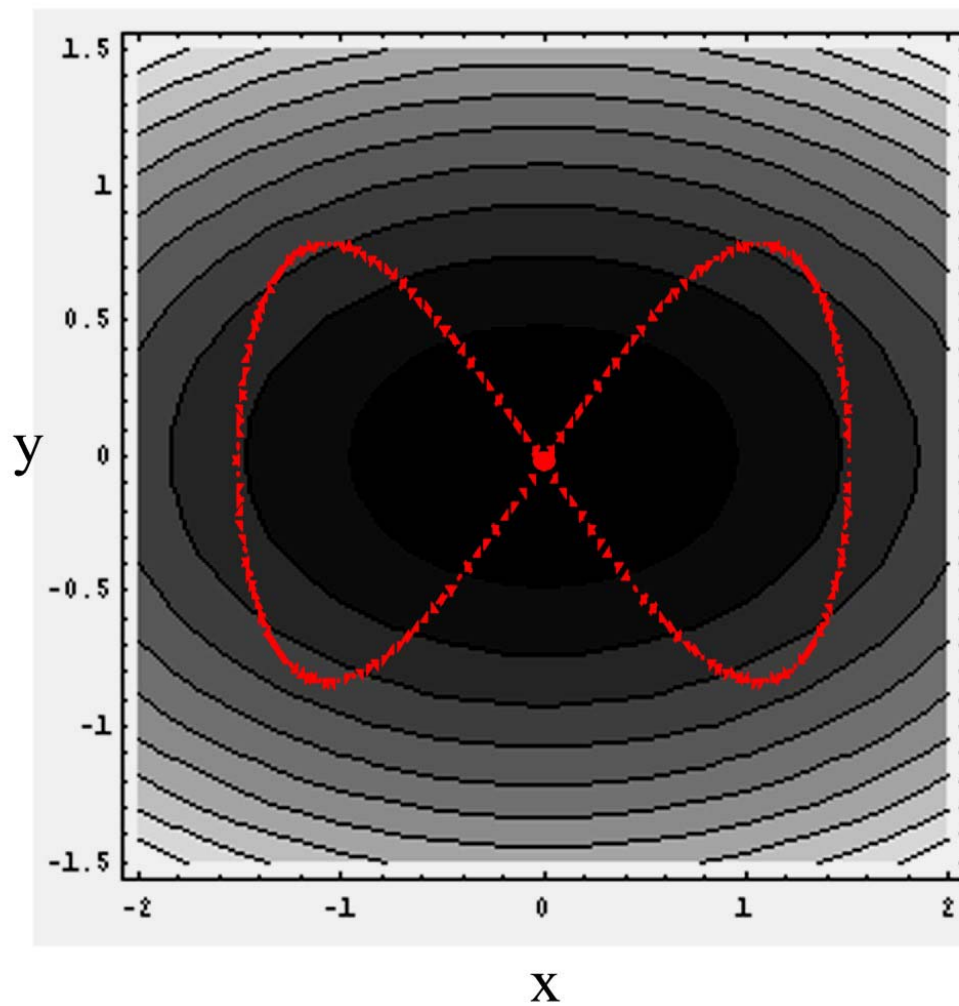


Figure 3.3. This plot displays the time-evolution of the trajectory initially located at the center of the wave packet. The contour lines represent the anisotropic classical potential that guides the particle. This same trajectory was obtained when Newton's equations of motion were solved for this potential

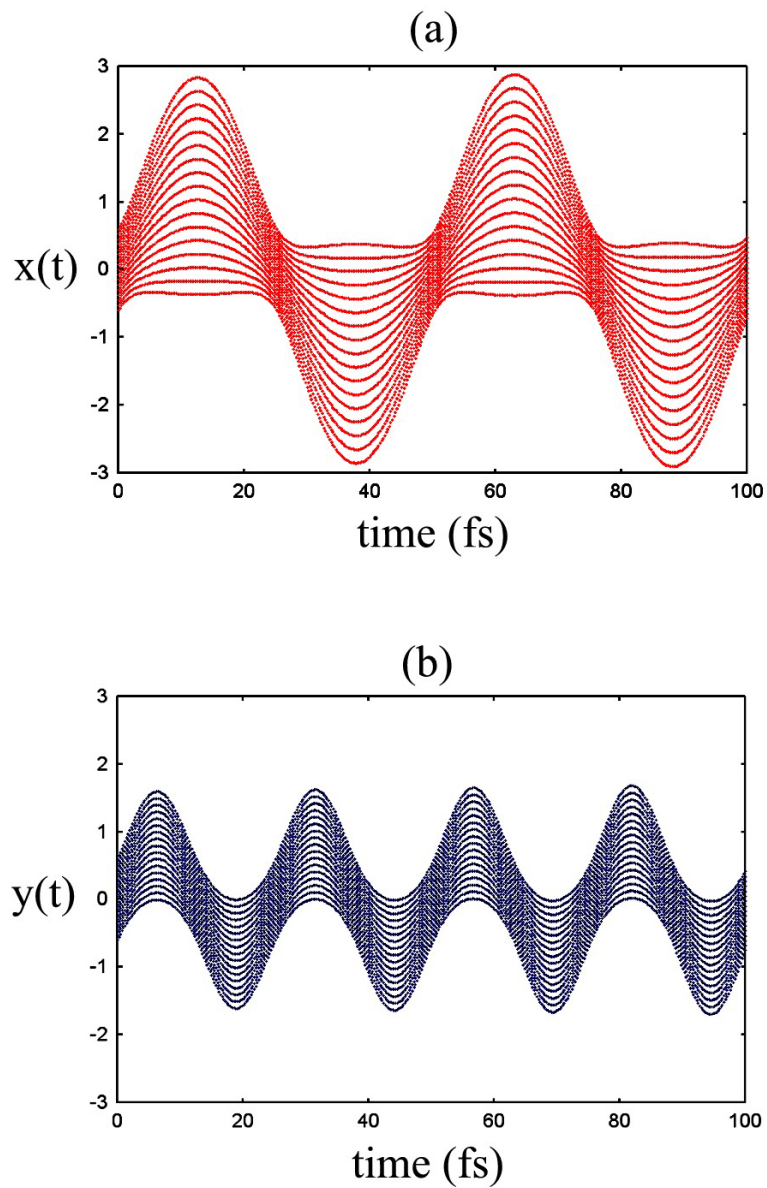


Figure 3.4. Plot (a) displays the x -dependent oscillator trajectories at the $y = 0$ cross section. Plot (b) shows the y -dependent trajectories at the $x = 0$ cross section. Both plots were calculated using the QTM.

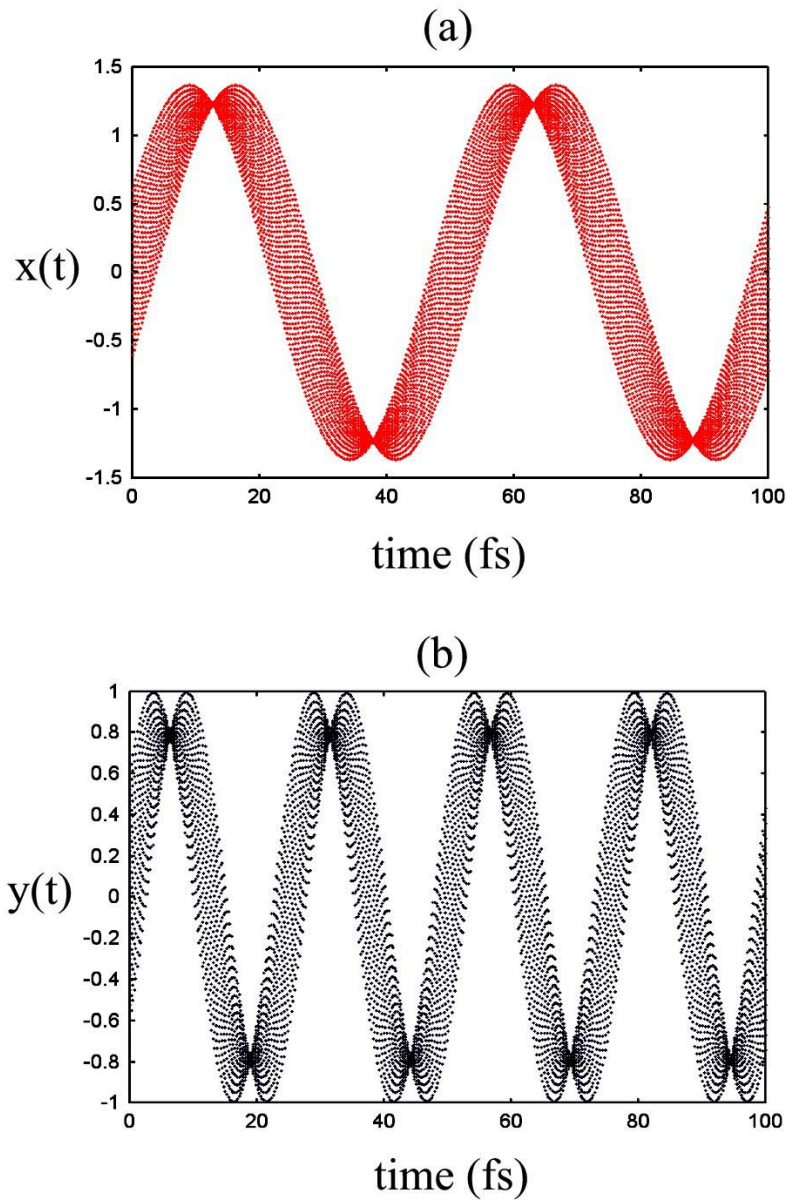


Figure 3.5. Plot (a) displays the x -dependent oscillator trajectories at the $y = 0$ cross section. Plot (b) shows the y -dependent trajectories at the $x = 0$ cross section. Both plots were calculated using Newton's equations of motion for the harmonic oscillator.

with $V_o = -1500 \text{ cm}^{-1}$ (see Fig. 3.6). This particular model provides insight into the nature of exothermic chemical reactions and photodissociations on excited state potential energy surfaces. For this problem, four wave packets, initially centered at $(0,0)$, were launched with energies of 0, 500, 1500, and 8000 cm^{-1} . A total of merely 17 particles were used for each wave packet! (This number is many orders of magnitude smaller than what would be needed with a ψ -propagator for the same unbound problem.) The RMS width of each initial 1D Gaussian was $\sigma = 0.25$, and the system mass used was $m = 2000$. To integrate the QHEM for this potential in time, the Adam's Bashforth multi-step procedure, initiated with RK4, was used with a time step of $dt = 0.5$. To obtain the spatial derivatives at each time step, radial basis function interpolation was used (see Appendix D).

The time-dependent transmission probabilities for each of the four wave packets are shown in Fig. 3.7, plot (a). To calculate this, the trapezoid method was used for integration. In this numerical procedure, calculation of the time-dependent transmission probabilities is given by

$$P_{trans}(t) = \int_{x_b}^{\infty} \rho(x,t) dx = \sum_i \rho_i(x_{i+1} - x_i) \text{ for all } x_i > x_b = 2.2. \quad (3.23)$$

The solid line in Fig. 3.7, plot (a) refers to results obtained using a fixed grid, ψ -propagator (see Appendix A). The two curves are in excellent agreement. This plot displays results for only 70 fs. After this time, inaccuracies in the trapezoid method give incorrect transmission probabilities, though the actual QTM solutions were fine. This is

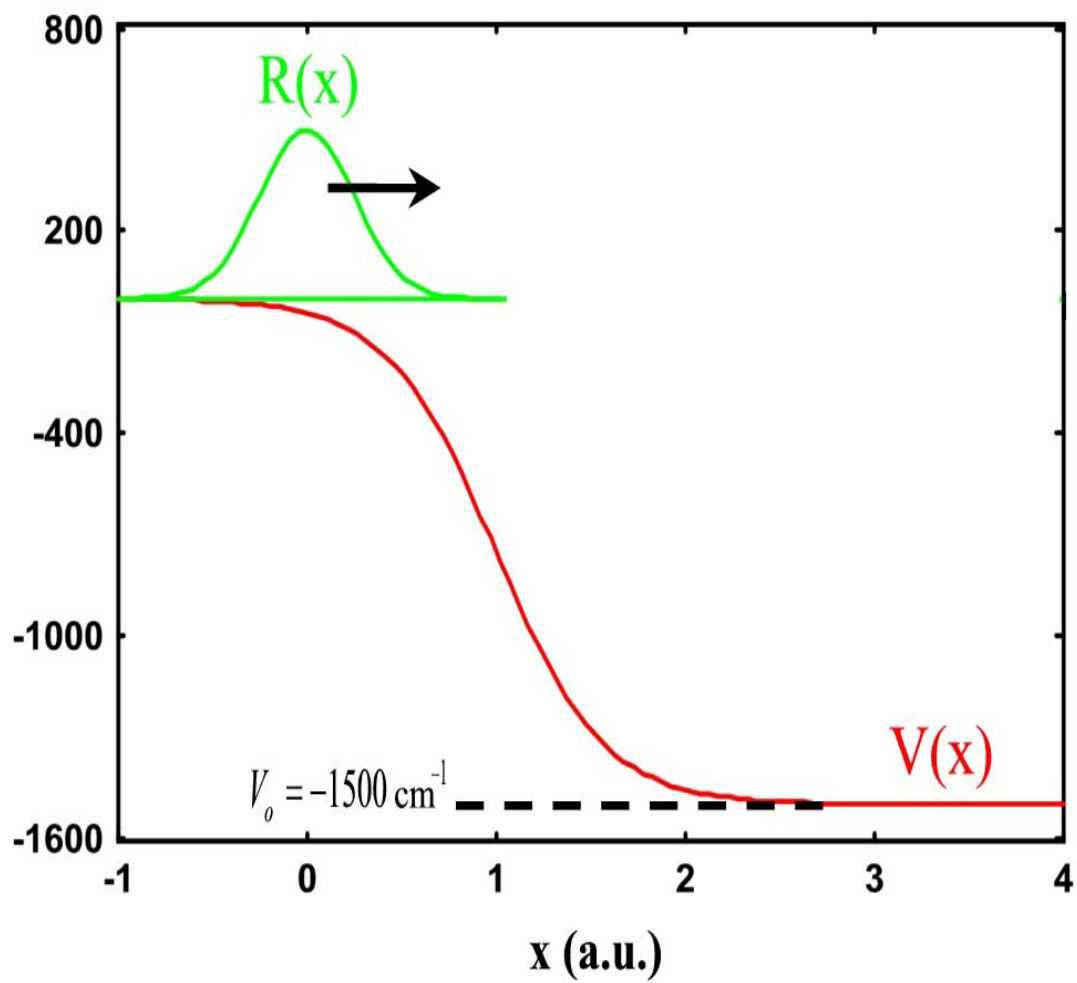


Figure 3.6. Downhill ramp potential energy surface and initial Gaussian wave packet position used in the second QTM application.

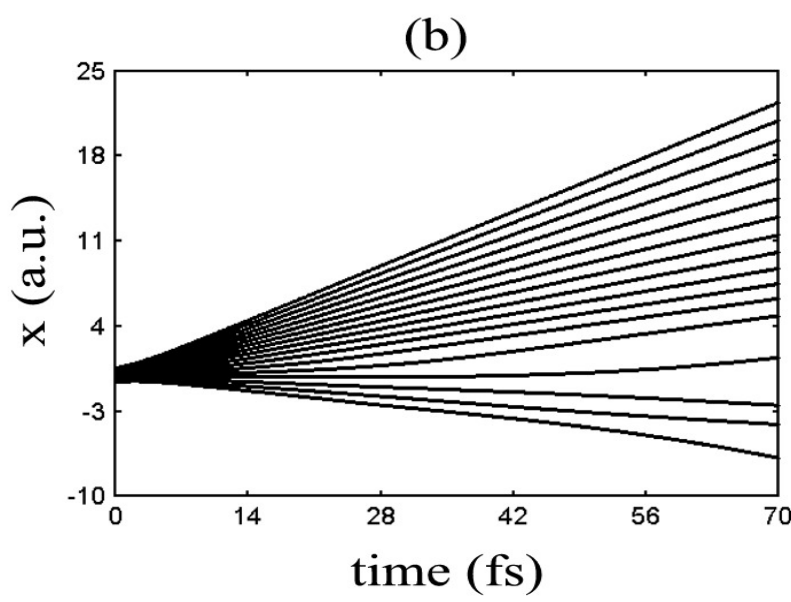
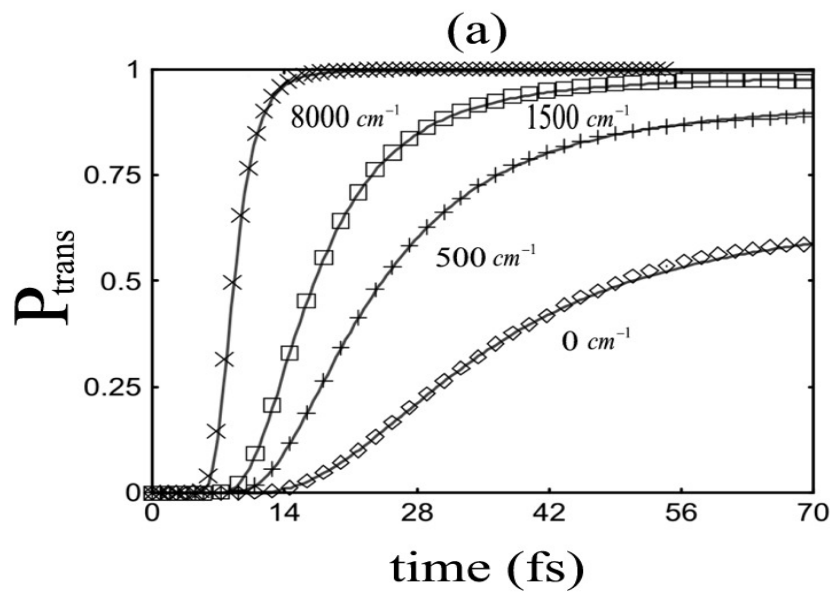


Figure 3.7. Plot (a) of this figure displays the time-dependent transmission probabilities obtained by applying the QTM to the uphill ramp problem. Four different energy wave packets were propagated. In plot (b), trajectories are plotted for the wave packet with an initial energy of 1500 cm^{-1} .

because the accuracy of the trapezoid method is determined by the particle spacings, and when these spacings become large, errors can develop. As time moves on, the particles spread apart due to the quantum potential, causing numerical breakdown of the trapezoid method. If accurate transmission probabilities are needed for longer times, either more particles can be used to decrease spacings or more accurate density integration methods can be used.

Plot (b) of Fig. 3.7 shows trajectories for the wave packet with an energy of 1500 cm^{-1} . One important feature of this plot is the reflection of the first three particles to the $-x$ direction. Two asymmetric ensembles are formed from this bifurcation, representing the reflected and transmitted portion of the wave packet amplitude. Classically, there is no turning point, and all the particles will proceed down the potential ramp with increasing velocity. However, it is well known that in the quantum case, above the barrier reflection can occur, resulting in only partial transmission of the total probability. These unusual accelerations on the reflected particles are due to the quantum potential displayed in Fig. 3.8. Initially, the quantum potential is similar to that of a free wave packet, and the corresponding quantum forces work to spread the packet in space. According to Lopreore and Wyatt [13], it is the initial boost in kinetic energy, resulting from the quantum force, that pushes some particles in the $-x$ direction, thus preventing them from transmitting at future times. Whether the particle is transmitted or not depends upon its initial velocity and this push from the quantum force. If the particle is given enough positive velocity to overcome the quantum forces acting against it, it will transmit. If not, the particle will reflect.

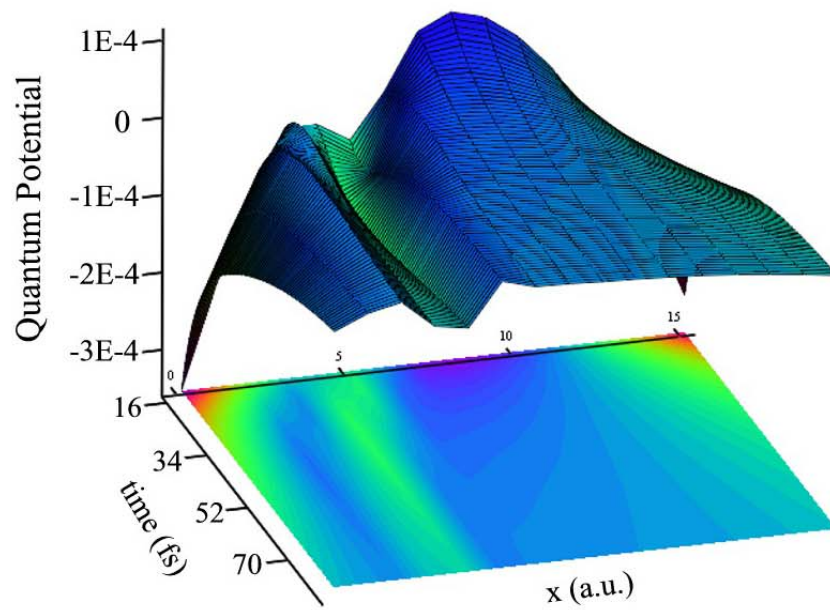
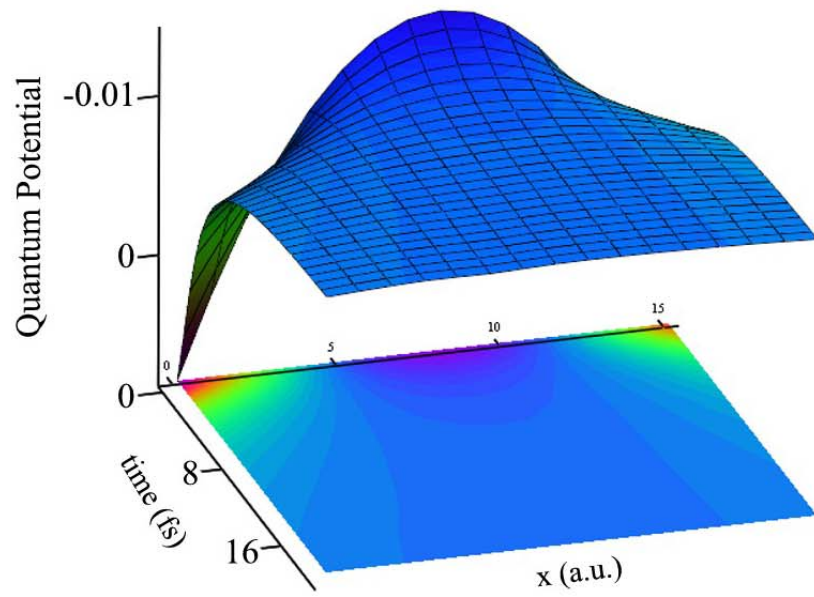


Figure 3.8. The time-dependence of the quantum potential for the downhill ramp.

As the quantum potential evolves in time, it loses magnitude and ripples begin to form in the region of reflected amplitude. In the transmitted regions, on the other hand, the quantum potential remains approximately quadratic. Although it is not shown here, the quantum force also has ripples in the reflected region. These ripples form due to amplitude interference between the remaining incoming waves and those already reflected. In such regions of interference, particles can have very complicated dynamics, and solutions to the QHEM can be difficult to calculate numerically, even though good results were obtained in this example.

3.3.3.4. *The Eckart barrier*

For the applications discussed so far, the QTM numerically dominates over integration of the TDSE on a fixed grid. This is because very few particles were used to obtain extremely accurate solutions to the QHEM. This is especially so for the unbound, uphill ramp potential, since propagating the complex wave function in this case requires many grid points spread over a large highly-resolved lattice. In addition, relatively large time steps were used to integrate the QHEM for these problems. In fact, for the first two cases, the hydrodynamic solutions were smooth enough in time to use the first order accurate Euler integrator. The QTM in these applications thus outperforms direct numerical integration of the TDSE on various computational fronts. We will now see, however, that the QTM does not always yield such superiority. In fact, for the last application presented, exact converging solutions to the QHEM have not yet been obtained using the QTM.

In this application, an Eckart barrier potential of the form

$$V(x) = V_o \operatorname{sech}^2[a(x - x_b)], \quad (3.24)$$

was used. This potential represents the variation of 2D reaction potential along its minimum energy path, as discussed in Chapter two. In this problem, the barrier height is $V_o = 8000 \text{ cm}^{-1}$, the center of the barrier is located at $x_b = 6$, and the width of the barrier is $a = 0.5$. An initial 1D Gaussian wave packet with energy $E = 8000 \text{ cm}^{-1}$ was launched in the direction of the barrier. This setup is displayed in Fig. 3.9. The wave packet parameters were $m = 2000$, $v = 0.006$, and $\sigma = 0.16$. The same time-integration and derivative approximation methods used to solve the uphill ramp problem were used in this problem. The QTM FORTRAN 90 code used to solve this problem is given in Appendix F.

For the first 45 fs of the QTM calculation of the Eckart barrier problem, the solutions are very accurate. However, after 47 fs, the algorithm “blows-up” and the propagation is thereafter terminated. Typically, blow-ups occur when numerical solutions become unstable or there is division by a number close to zero. To investigate why this happens in the Eckart problem, the probability density is followed in time up to the point where strange things start to happen. In Fig. 3.10, the density is plotted at 47 fs. The solid blue line in this plot is the density obtained by numerically solving the TDSE equation. From this plot, it is easy to see the source of the blow-up.

Encircled in red in Fig. 3.10 is a density pseudo-node. One important attribute of the QHEM is that in these nodal regions, the quantum potential and the quantum force have extremely large magnitudes⁴. The quantum force in this nodal region can be seen in

⁴ At a true node, the quantum potential is singular and the quantum force is undefined.

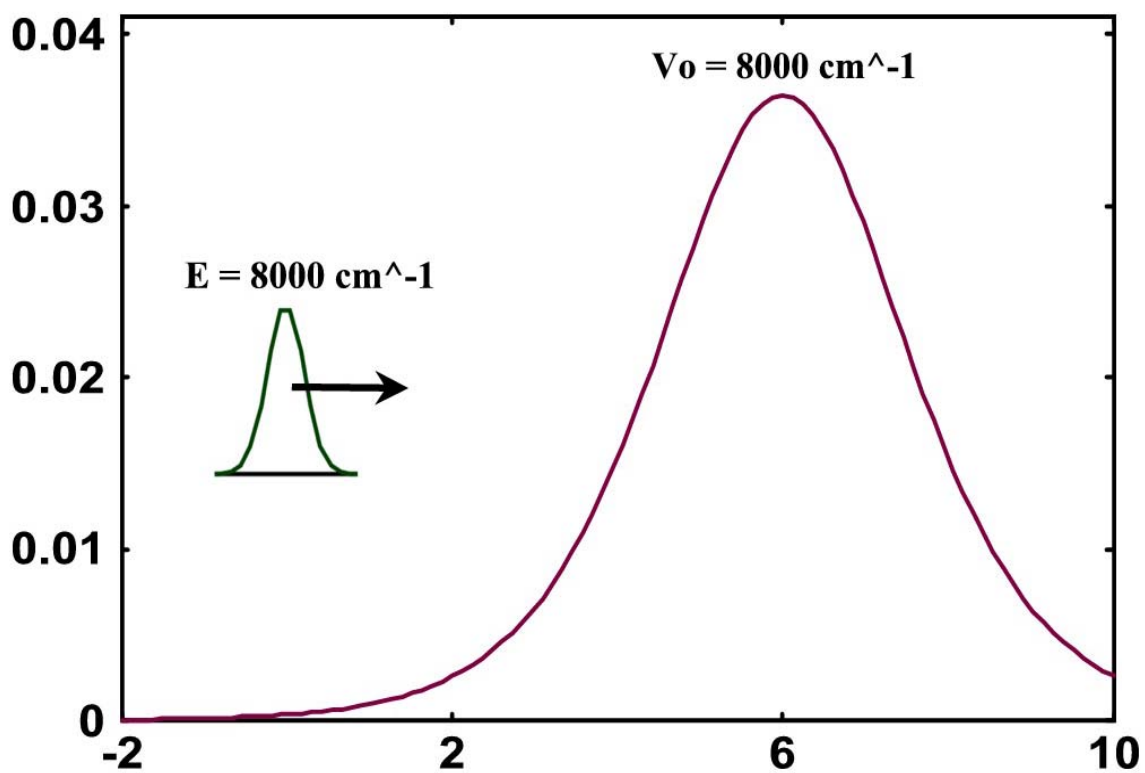


Figure 3.9. The Eckart barrier potential and initial Gaussian used in the last QTM application.

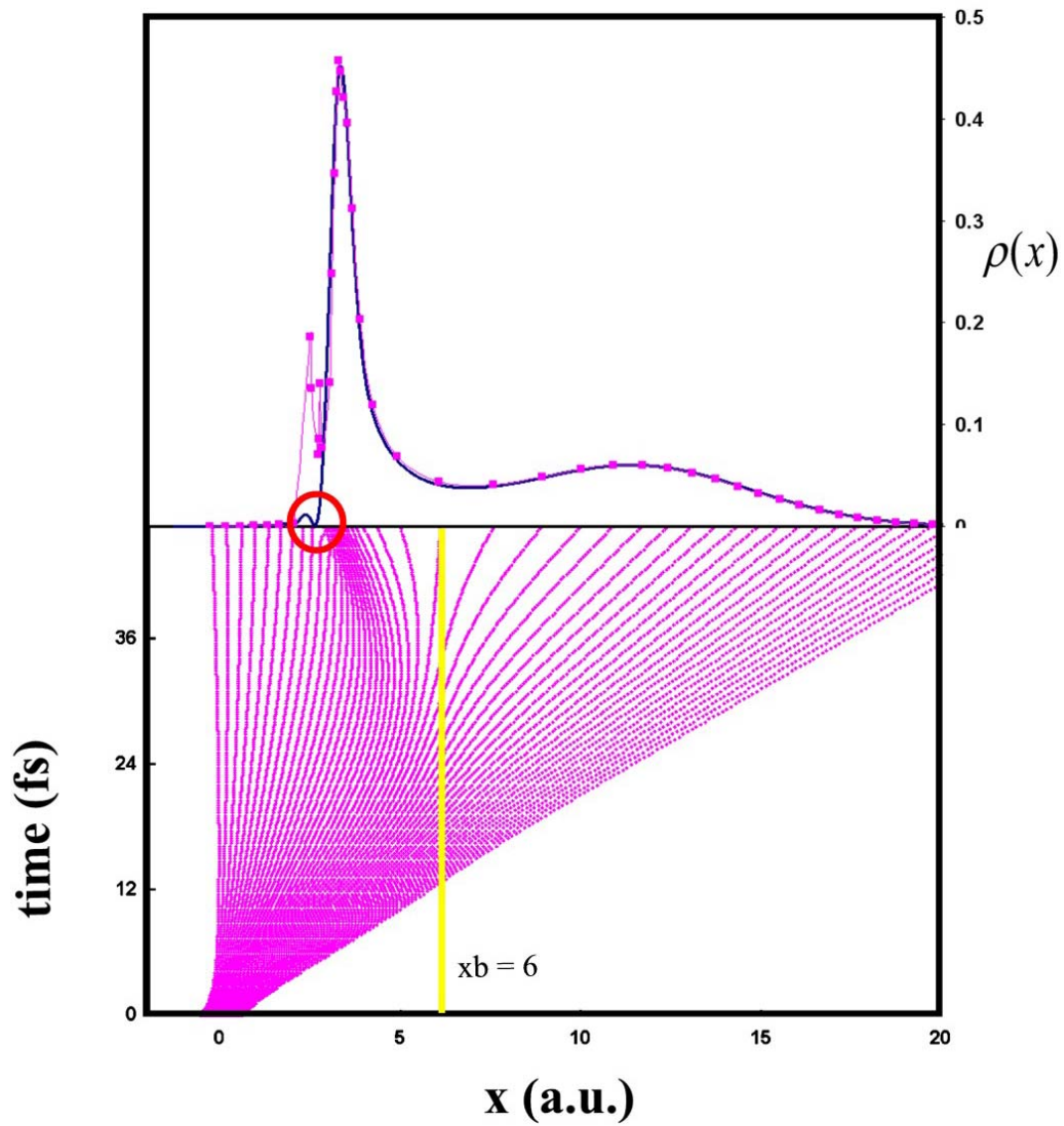


Figure 3.10. In the bottom part of this figure, QTM trajectories for the Eckart barrier problem are plotted in time until numerical breakdown occurs. At the point of breakdown, the density is plotted vs. position (the top part). The solid blue curve in the top plot is the probability density as calculated from the TDSE. The solid yellow line indicates the Eckart barrier maximum. A pseudo-node is circled in red.

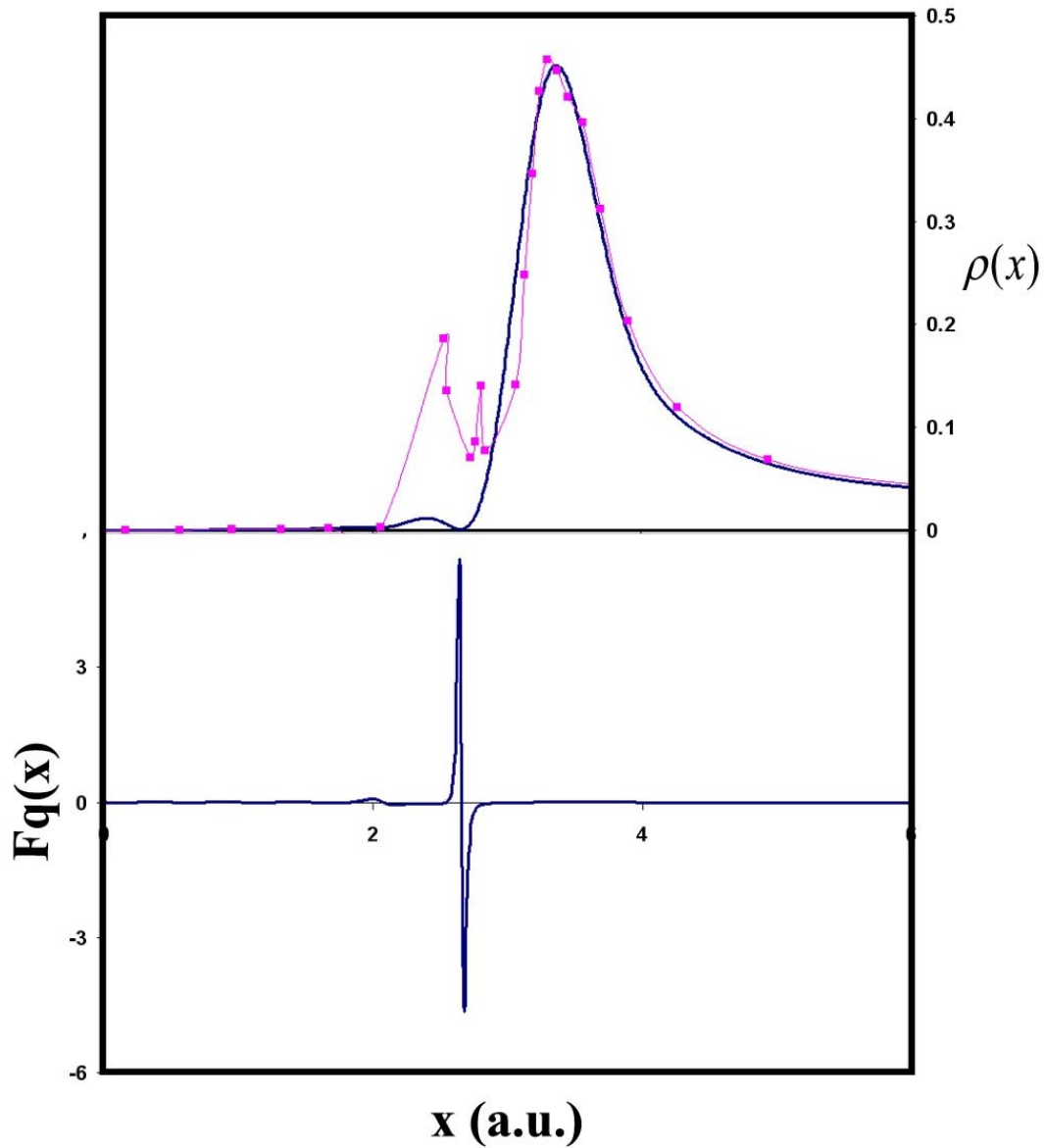


Figure 3.11. In this figure, the region of the pseudo-node is further examined. In the top plot, a close-up on the probability density is given. The pink dots indicated values obtained from the QTM, and the solid blue line displays results obtained from solving the TDSE. In the bottom plot, the quantum force is plotted at the same breakdown time. Here, the quantum force was calculated by integrating the TDSE.

Fig. 3.11. This plot was calculated from the wave function solutions obtained by integrating the TDSE on a very fine grid. The results are indeed not pretty. The quantum potential is no better. The unfortunate effects of the quantum potential and force in the region of the pseudo-node can be further examined by looking at the particle trajectories.

If the trajectories are followed in time up to the breakdown point, a number of things can be deduced. Until approximately 30 fs, the particles sweep out very smooth paths in space. After this time, wave packet bifurcation begins to occur, and some of the inner trajectories are reflected from the center position of the barrier, represented by the yellow solid line. As times moves on, the pseudo-node begins to develop and particles are forced away from this region as well. After 40 fs, the trajectories are squeezed between the potential barrier and the node. These trajectories are trapped in this region until the node disappears and they are free to reflect. In the ‘trapped’ region, compression occurs, meaning that the particle density is large. Around the barrier center, inflation occurs, meaning that there are too few particles. Both of these can give problems when trying to obtain spatial derivatives from fitting and interpolation methods. In addition, because this node forms rather quickly, stiff equations of motion for the C and S fields are encountered. Consequently, even if a suitable method for derivative approximation could be found that gave accurate fits in this region, an implicit time-integrator would be needed. This would significantly slow down the computational time, since implicit integrators require the decomposition of a matrix. Also, for multi-dimensional problems, implicit solvers can be impractical.

In this problem, time-stiff trajectories in the compressed region and the large amplitude gradients and curvatures in the pseudo-nodal region cause numerical

breakdown of the QTM. The Eckart barrier is just one of the many potential energy surfaces in which these problems can arise. It is important to note that problems in nodal regions are not encountered when integrating the TDSE. These problems are solely due to the quantum potential encountered in the QHEM.

3.3.4. QTM discussion

In the preceding sections of this chapter, a novel numerical method for integrating the quantum hydrodynamic equations of motion was discussed. This method, the QTM, was used to solve the QHEM for four model potential energy surfaces. In the first three models, excellent results were obtained with fewer grid points and larger time steps than needed when integrating the TDSE on a fixed grid. Of these three models, the only amplitude interferences encountered were in the uphill ramp problem, and these were very small in magnitude and only truly visible when looking at the quantum potential. No nodes or pseudo-nodes were obtained.

In the last example given, a wave packet was propagated into an Eckart barrier potential. In this problem, the QTM gave early numerical breakdown, and a convergent transmission probability was not obtained. One source of the numerical blow-up was interpolation errors resulting from compression and inflation in the vicinities of the pseudo-nodes and the potential barrier center. In addition, the hydrodynamic solutions in these regions were stiff in time, and explicit time-integrators may have exacerbated interpolation errors.

To fully cure the problems associated with the QTM, both derivative approximation and time-integration problems near nodal regions must be addressed.

However, it is speculated that the immediate source of the numerical errors in the QTM arises from fitting or interpolation. If this is indeed the case, better results might be obtained if a new method is developed that would allow for more accurate derivative approximations. In the next section, a new numerical method for integrating the QHEM is discussed that eliminates the compression and inflation problems encountered in the QTM. This method is called the arbitrary Lagrangian Eulerian (ALE) method. Using this method, more accurate derivative approximations can be made, and the propagation time of the QHEM solutions can be lengthened tremendously.

3.4. THE ARBITRARY LAGRANGIAN-EULERIAN (ALE) METHOD

3.4.1. ALE background

To alleviate the inflation and compression complications encountered in the Lagrangian QTM, a suitable control on the particle trajectories must be implemented. Ideally, one would like to eliminate under-sampling and clustering while guiding the particles to locations that will help minimize fitting errors in the approximate spatial derivatives (i.e. guiding the grid points to regions where gradients and curvatures are large). It is quite obvious that this cannot be done using the Lagrangian QTM, however, for the arbitrary Lagrangian Eulerian (ALE) method, *in which the particle velocities are not equal to the flow velocity of the probability fluid*, absolute control over the particle's trajectory can be obtained. Using the ALE, particle velocities can be specified in various ways, including coupling to a boundary velocity, adaptive adjustment at the end of each time step, or through some combination of the above. ALE methods have proven extremely successful in many classical fluid and solid dynamical problems [40-49].

3.4.2. ALE methodology

Recall the fixed-grid versions of the QHEM given in Eqs. (3.2) and (3.3). To move this grid in time, a suitable transformation from the partial derivative to the total time derivative must be made. By introduction of a *grid velocity* term, $\dot{\vec{x}}$, which is *not* necessarily equal to the flow velocity of the probability fluid, the relationship between the two time-derivatives becomes

$$\frac{d}{dt} = \frac{\partial}{\partial t} + \dot{\vec{x}} \cdot \vec{\nabla}. \quad (3.25)$$

Upon substitution of this total time derivative, the *moving grid form of the hydrodynamic equations of motion* become

$$\frac{dS(\vec{r}, t)}{dt} = (\dot{\vec{x}} - \vec{v}) \cdot (m\vec{v}) + L_Q, \quad (3.26)$$

$$\frac{d\rho(\vec{r}, t)}{dt} = (\dot{\vec{x}} - \vec{v}) \cdot \vec{\nabla}\rho - \rho\vec{\nabla} \cdot \vec{v}, \quad (3.27)$$

where L_Q is the quantum Lagrangian defined as

$$L_Q = \frac{1}{2} m\vec{v} \cdot \vec{v}^T - (V + Q). \quad (3.28)$$

Both Eqs. (3.26) and (3.27) contain the term $\vec{w} = \dot{\vec{x}} - \vec{v}$ called the *slip velocity*. When the slip is non-zero, the particle either falls behind or advances on the Lagrangian fluid elements. Three conditions that depend upon the slip velocity can arise:

1. $\vec{w} = -\vec{v}$, $\dot{\vec{x}} = 0$, (3.29)
2. $\vec{w} = 0$, $\dot{\vec{x}} = \vec{v}$,
3. $\vec{w} \neq -\vec{v}$ and $\vec{w} \neq 0$, $\dot{\vec{x}} \neq \vec{v}$ and $\dot{\vec{x}} \neq 0$,

Under the first condition the grid point locations are fixed in time, and the original equations for the action and amplitude update, Eqs. (3.2) and (3.3), are recovered. Fixed-grid Eulerian schemes can provide very accurate solutions. However, as stated before, they often require large grid-lattice and can be computationally inefficient in regions of low wave function activity. In unbound problems, very large grids are needed for long time propagations, and if a high resolution is required for the wave function dynamics in certain regions, that resolution is often used throughout the entire grid domain. This is not computationally efficient, since such resolution may not be required throughout the entire domain. This problem becomes greatly amplified for long wave packet propagation times, high-energy dynamics, and high dimensionality problems.

In the second condition, the grid points are locked in concerted motion with the fluid and move along with the flow velocity. Under this Lagrangian condition, fewer grid points are needed, as the trajectories tend to follow regions of high density and complex dynamics. This condition gives Eqs. (3.7) and (3.8) and leads to the QTM. One advantage of employing the QTM in this way is that Bohmian trajectories are governed by a physical law and can be subject to physical interpretations. However, as mentioned previously, this method does not always provide a robust algorithm for obtaining solutions of wave packet dynamics, and the stability and accuracy of the method are almost completely governed by the dynamics of the trajectories as time proceeds.

Lastly, it is condition three, the ALE method, which will help resolve many of the problems encountered in the pure Lagrangian version of the QTM, while maintaining its superiority over fixed-grid methods in the relatively small number of grid points needed for wave packet propagation. In the ALE method, grid velocities can be assigned to

dynamically adapt to the hydrodynamic fields as they advance in time. This technique is also denoted by the term *r-refinement* [50] (redistribute or relocate), and it often involves coupling a new partial differential equation for solving the grid velocities at each time step to the original equations of motion. It should be noted that the paths taken by the grid points in the ALE method are no longer the physical Bohmian trajectories encountered in the pure Lagrangian scheme, since the grid velocities are not given by Eq. (3.6). This is a small sacrifice, since it is now possible to have *complete control* (via the grid velocities) over when and where the grid points dynamically react to the solution.

Once the moving path transformations of the QHEM are derived, it is then left to determine exactly how to prescribe the particle velocities in time. There are many ways of doing this. One of the most popular ways of calculating these velocities is by using the equidistribution method. Using this scheme, grid points can dynamically adapt in time according to properties of the solution (i.e. it's gradient, curvature, etc.). This method will now be described in detail.

3.4.2.1. *The equidistribution method and dynamic grids*

Consider $np + 1$ time-dependent grid points defining a one-dimensional spatial grid at $t > 0$ with the ordering $x_i(t) < x_{i+1}(t)$ for $i = 1, 2, \dots, np - 1$. A number of studies [50-56] have shown that spatial fitting errors can be reduced by distributing the grid points so that a positive weight or *monitor* function is equally distributed over the field,

$$\int_{x_i}^{x_{i+1}} M(x) dx = \text{constant}, \quad (3.30)$$

or in its discrete form,

$$M_i(x_{i+1} - x_i) = \text{constant} . \quad (3.31)$$

This equidistribution method is equivalent to the equilibrium conditions for a system of classical springs where the monitor functions play the role of *spring constants*. Spring analogies for spatial adaptation have been recently used to obtain solutions of the Navier-Stokes equations for a number of classical fluid dynamic problems. A few examples of these include the following: the utilization of tension and torsion springs for two and three-dimensional adaptive grids in fluid flow simulations [53,55,51]; springs used for spatial adaptation of the coupled equations resulting from an unsteady, compressible fluid flow over a rigid-body [56]; springs used for a grid adaptation algorithm simulating the laminar flow of perfect gas [54]; and spring systems combined with “pseudo-pressure” penalty terms for preventing mesh overlapping in a 1-D shock tube and in 2-D and 3-D steady flow calculations [50].

To obtain the equilibrium positions, $\{x_i\}$, a homogenous tri-diagonal system of equations of dimension $np \times np$ must be solved. The elements of the spring coefficient matrix will depend on the monitor values at the corresponding grid points. By solving this system of equations, the grid points can be instantaneously adapted according to the specific monitor function used.

Most monitors are designed to sense specific information about the hydrodynamic fields at each time step, and subsequently, use this information to redistribute the positions of the grid points. It is the non-uniformity in the nearest neighbor monitor values, M_{i-1} and M_{i+1} , that cause the grid points to move relative to one another. For example, if the monitor function is gradient/curvature dependent, then the grid points will

be redistributed with a greater density in regions of large gradients/curvatures. If all of the monitor functions are set to the same value, the grid points will sweep out paths with equal spacing, thus forming an expanding/contracting uniform grid of spacing $h(t)$. Some typical monitor functions are the following: (1) $h^k \|u^{k+1}\|$; (2) $1 + \beta(\partial u / \partial x)$; (3) $1 + \beta(\partial^2 u / \partial x^2)$; and (4) the truncation error of the solution divided by h (where u^k indicates the k -th x-derivative of the solution, h is the local point spacing, and β is an input parameter).

Initially, an algorithm was developed to solve the hydrodynamic equations of motion with the equidistribution method using monitor functions (2) and (3) using $u = C = \ln(R)$. The algorithm was implemented in the following way:

- I. A *predictor* step was taken to advance the grid points in time from $x(t) \rightarrow x^L(t + \Delta t)$, where x^L is the new temporary coordinate found using the density flow velocities, \vec{v} . This is the trajectory that a particle would follow in the pure Lagrangian description. It is not likely that the new particle positions, $\{x_i^L\}$, create the optimal configuration of grid points (the optimal configuration can be defined as the grid point distribution that minimizes fit or interpolation errors).
- II. The tri-diagonal system representing the discrete equidistribution equations, Eqs. (3.31), were then solved with given monitor functions, $M_i(t)$. The boundary conditions for particles 1 and np in the spring

equations were set to be the solutions of the pure Lagrangian equations of motion, i.e. $x_1(t + \Delta t) = x_1^L(t + \Delta t)$ and $x_{np}(t + \Delta t) = x_{np}^L(t + \Delta t)$. All of the internal $(np - 2)$ grid points were distributed according to the monitor function.

- III. This is the *corrector* step. After predicting where the grid point positions should be at $t + \Delta t$ from step 2, the grid velocities were then calculated. If the $\{x_i\}$ are the adapted positions from step 2, and $\{x_i^L\}$ are the positions developed along the pure Lagrangian trajectories, the grid velocities can be calculated from the equation,

$$\dot{x}_i = v_i + \frac{x_i - x_i^L}{\Delta t}, \quad (3.32)$$

where the second term is an approximation of the slip velocity.

Step two of the above algorithm lead to problems, however, since there is no limit placed on the separation between adjacent grid points. Since Bohmian trajectories are not allowed to cross, any grid velocity equations coupled to the hydrodynamic equations of motion should also satisfy this condition. In fact, as can be seen from the pure Lagrangian version of the QTM, computational problems are encountered even as the trajectories become close to one another. Ideally, grid velocity equations should be devised to keep the grid points a minimum distance away from one another while simultaneously adapting the grid to the evolving hydrodynamic fields. It was therefore

determined that a new set of equations for obtaining the adapted positions, $\{x_i\}$, must be derived to restrict the particles to a minimum separation, $x_{i+1} - x_i > \delta x_{\min}$.

For this purpose, consider the three grid points $\{x_{i-1}, x_i, x_{i+1}\}$ and a set of two harmonic potentials of the form

$$V_L(x_i) = \frac{1}{2}(x_i - x_o^{left})^2, \quad (3.33)$$

$$V_R(x_i) = \frac{1}{2}(x_i - x_o^{right})^2. \quad (3.34)$$

To derive equations for the $\{x_i\}$ that include a minimum separation parameter, x_o^{left} is defined in the limit that $M_{i+1}/M_{i-1} \rightarrow 0$ for $M_{i-1} > M_{i+1}$ to be

$$x_o^{left} = X_{left} = x_{i-1} + \delta x_{\min}. \quad (3.35)$$

Likewise, in the limit that $M_{i-1}/M_{i+1} \rightarrow 0$ for $M_{i+1} > M_{i-1}$

$$x_o^{right} = X_{right} = x_{i+1} - \delta x_{\min}. \quad (3.36)$$

For $M_{i+1}/M_{i-1} \neq 0$ and $M_{i-1}/M_{i+1} \neq 0$, the two potential minima can be set such that

$X_{left} < x_o^{left} < X_o$ and $X_o < x_o^{right} < X_{right}$, where the midpoint is $X_o = 1/2(x_{i-1} + x_{i+1})$

(see Fig. 3.12).

If the centers of the quadratic potentials are defined as

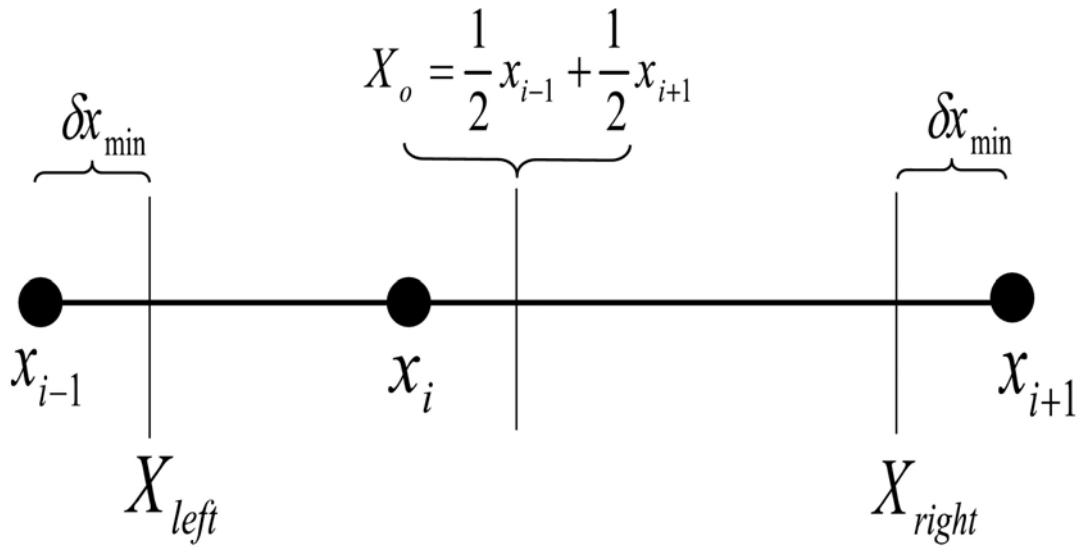


Figure 3.12. Spring setup for inclusion of the minimum separation parameter, δx_{\min} .

$$x_o^{left} = X_{left} + \frac{M_{i+1}}{M_{i-1}}(X_o - X_{left}), \text{ for } M_{i-1} \geq M_{i+1}, \quad (3.37)$$

and

$$x_o^{right} = X_{right} - \frac{M_{i-1}}{M_{i+1}}(X_{right} - X_o), \text{ for } M_{i-1} \leq M_{i+1}, \quad (3.38)$$

then either Eq. (3.37) or (3.38) can be solved for its minimum (i.e. setting $-\partial V_i / \partial x_i = 0$). It should be emphasized that *either* of these equations is solved for the position x_i , depending on the larger value of M_{i+1} or M_{i-1} . By utilizing the same boundary conditions as before, a tri-diagonal system of equations of dimension $np \times np$ was derived and incorporated into step two of the algorithm for determining grid velocities. Figure 3.13 displays an example of how the grid points are allocated using the above spring system according to an analytical and arbitrary monitor function. At this point it should be stated that although the ratios M_{i+1}/M_{i-1} and M_{i-1}/M_{i+1} were used to obtain the computational results discussed later in this study, they are very sensitive to small variations between the two adjacent monitor functions, and small differences can lead to large shifts in the grid point positions. This is not desirable, since excessive movement in the grid points destroys the smooth time progression of the solutions to the equations of motion. In the future, Gaussian functions of the form $f(M_{i-1}, M_{i+1}) = \exp[-\beta(M_{i-1} - M_{i+1})^2]$ could be used instead of the previously used ratio as long as the appropriate limits are upheld. In this function, β can be used as a parameter affecting the magnitude of the grid point shift towards adjacent grid points.

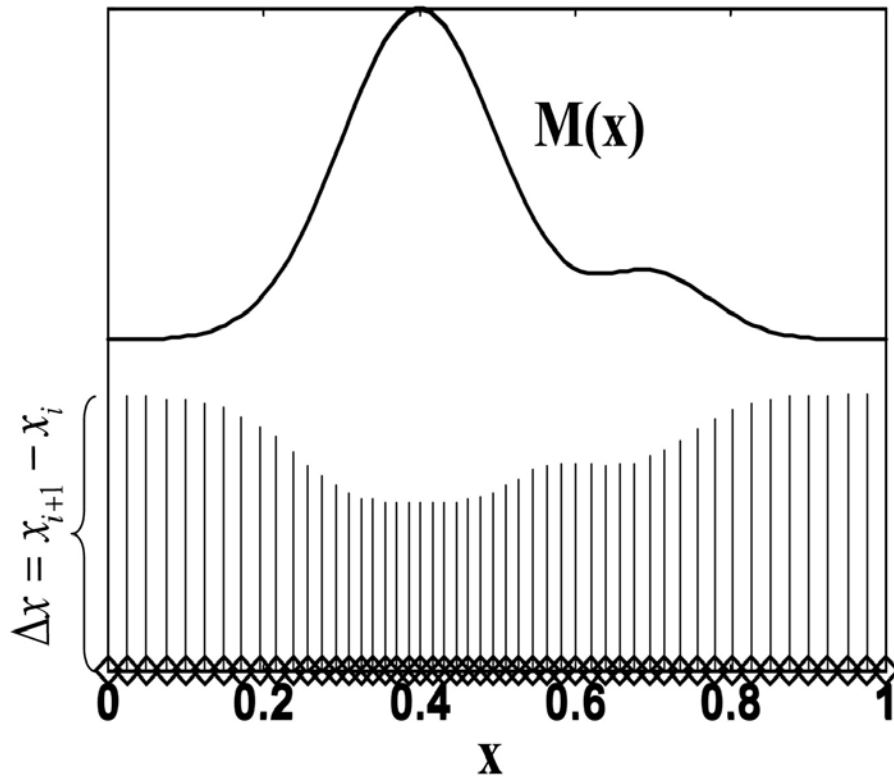


Figure 3.13. An example of a monitor function, $M(x)$, and the new coordinates calculated using the spring system algorithm *with the separation parameter*. The impulses represent particle spacing. Notice that the grid points do not collapse to zero separation as $M(x)$ increases.

Results from a number of trials of different separation parameters indicated that a time-dependent parameter, $\delta x_{\min}(t)$, was better suited for unbound problems. An explanation for this would be that initially the wave packet domain is relatively compact, and a small parameter is needed. As time advances, however, global errors increase, as does the grid size, and the original minimal separation may not be resolvable. The only restriction on the choice of δx_{\min} is that

$$(np - 1) \times \delta x_{\min}(t + \Delta t) < x_{np}^L(t + \Delta t) - x_1^L(t + \Delta t). \quad (3.39)$$

By setting the separation parameter to some fraction of the logical grid spacing, i.e.

$$\delta x_{\min}(t + \Delta t) = F \left[\frac{x_{np}^L(t + \Delta t) - x_1^L(t + \Delta t)}{np - 1} \right], \quad (3.40)$$

where $0 < F \leq 1$, then a time-dependent separation parameter was created.

For the ALE results described in the next section, the predictor/corrector algorithm was used along with the matrix forms of Eqs. (3.37) and (3.38). The monitor function used was $M(x) = 1 + \beta \|\partial^2 u / \partial x^2\|$, with $u = C = \ln R$. This particular monitor function was well suited for the time-evolution of an initial Gaussian wave packet for two reasons. In *Log* space, the Gaussian is a quadratic function and can be exactly fit for spatial derivatives. No spatial adaptation is therefore needed as long as the packet is Gaussian, and since $\partial^2 C / \partial x^2$ is reduced to the same constant for all monitor values, the grid points will follow equally spaced paths until some deviation from this form occurs. Another reason this monitor was used was to eliminate the need for “pre-processing” of the grid points. Because the initial wave packet form was Gaussian, a regular spaced grid

was all that was required for initialization, and redistribution of the initial grid point locations was not needed before launching the grid points.

3.4.3. The ALE applied to an uphill ramp

As mentioned previously, many quantum mechanical problems have not yet been treated successfully using the pure Lagrangian QTM. An example in which difficulties have emerged and resulted in the computational breakdown of this method include wave packet scattering from steep uphill ramps. Typically, in these problems, the wave packet is ‘squeezed’ against the ramp (resulting in compression of the particles), and a portion of the density is reflected backwards, sometimes resulting in the formation of ‘ripples’ in the tail of the reflected wave packet. Although the transmitted density is generally smooth in space, the dynamics of those particles reflected from the barrier can be extremely complicated due to the large quantum forces, and inflation/compression can occur. To emphasize the advantages of the ALE/spring method over the Lagrangian QTM in such scattering problems, a ‘steep’ uphill ramp potential of the form

$$V(x) = \frac{V_o}{1 + e^{-1.5(x-1)}}, \quad (3.40)$$

was substituted into the QHEM (V_o is the potential maximum at large values of x , see Fig. 3.14). The equations of motion were then solved using the adaptive ALE/spring algorithm with a one-dimensional initial Gaussian wave packet

$$\psi(x,0) = \left(\frac{1}{2\pi\sigma^2} \right)^{1/4} \exp\left[-\frac{1}{4\sigma^2}(x-x_o)^2\right] \cdot \exp[ik(x-x_o)]. \quad (3.41)$$

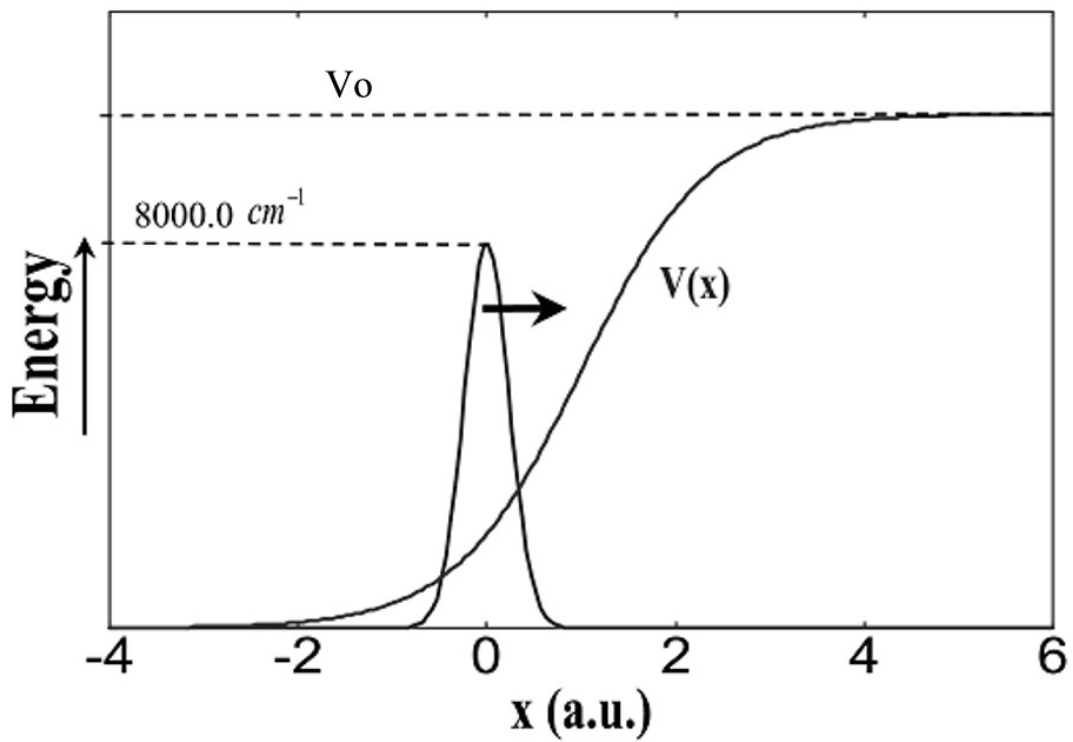


Figure 3.14. The initial Gaussian wave packet and the uphill ramp potential.

The initial parameters were as follows; $\sigma = 0.17$, $x_o = 0$, $m = 2000$, and translational energy = 8000 cm^{-1} . Time integration for both the QTM and the ALE method was done using the first order explicit Euler method with $dt = 0.085$. A total of 151 grid points were used with the initial uniform grid spacing $h = 0.01$. Spatial derivatives were obtained using radial basis function interpolation.

When the pure Lagrangian QTM was used to compute transmission probabilities for uphill ramp potentials of heights $V_o = 6000, 8000, 10000, \text{ and } 12000 \text{ cm}^{-1}$, computational breakdown occurred at $t = 76, 66, 56, \text{ and } 50 \text{ fs}$, respectively. Thus, as the height of the uphill ramp increases, the computational break down time of the Lagrangian QTM decreases. One explanation for this trend is that as the potential is increased, the wave packet is squeezed tighter (smaller width, larger amplitude) as it encounters the potential, and the particle compression is exacerbated. Also, as the height of the potential is increased, the magnitude and frequencies of the amplitude ripples in the reflected wave packet also increase. The consequences of these amplitude deformations are poor derivative approximation and eventual trajectory crossing.

Problems with break down were not encountered when the ALE/spring method was applied to the *same* uphill ramp models. Figure 3.15 is a plot of the transmission probability versus time for these ramp potentials using the ALE/spring method. All transmission probabilities were calculated by interpolating $\{\rho_i\}$ with piecewise cubic polynomials and integrating the polynomials for $x > 5$. Although the plot extends for only 400 fs (approximately 220,000 time steps), the transmission probabilities were

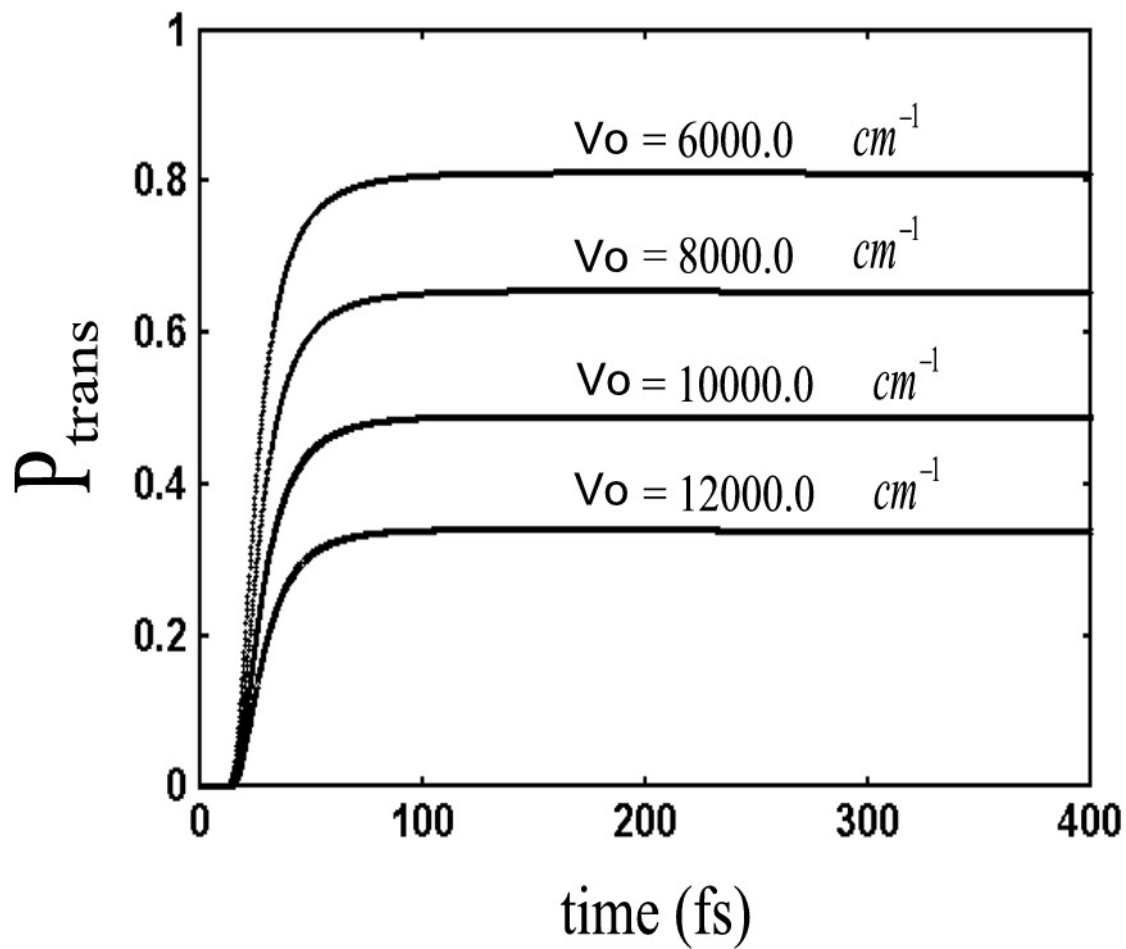


Figure 3.15. Transmission probabilities for the uphill ramp with four barrier heights calculated using the ALE/spring method. These values were obtained using an initial wave packet translation energy of 8000 cm^{-1} .

stable for *over one picosecond*. Such results are a profound improvement from the Lagrangian QTM.

Figure 3.16 displays the probability density at $t = 125$ fs. This figure provides one explanation of why the ALE/spring method yields computational results that are both accurate and stable for long times. The most important feature in this figure is the locations of the grid points. Although the grid points are allowed to adapt to regions of large curvature in the C-amplitude, the minimum separation parameter constrains the local grid point density to a maximum value and eliminates grid point clustering. In return, the grid points are spread throughout the domain, decreasing the chances of inflation near regions of low density. It is highly probable that the traditional Lagrangian QTM experienced most, if not all, of its computational difficulties when attempting to approximate spatial derivatives in the region of ripple formation in the reflected wave packet ($-16 < x < 0$). To obtain accurate approximations to the spatial derivatives of R and S in this critical region, the grid points must be properly positioned to capture the function's local oscillating behavior. Excessive inflation or compression in these regions will result in large-scale errors in the derivative approximations, and this is believed to have caused the numerical break down of the QTM after 76 fs into the computation. This is avoided in the ALE/spring algorithm, however, since the grid points are constrained to prevent over-clustering and excessive inflation.

Lastly, in Fig. 3.17 one can see how the accuracy of the probability density increases as the number of grid points in the ALE/spring method is increased from 151 to 251. In this figure, the probability density in the ripple region is plotted at $t = 110$ fs. The accuracy of the action and amplitude is predominantly governed by the errors in the

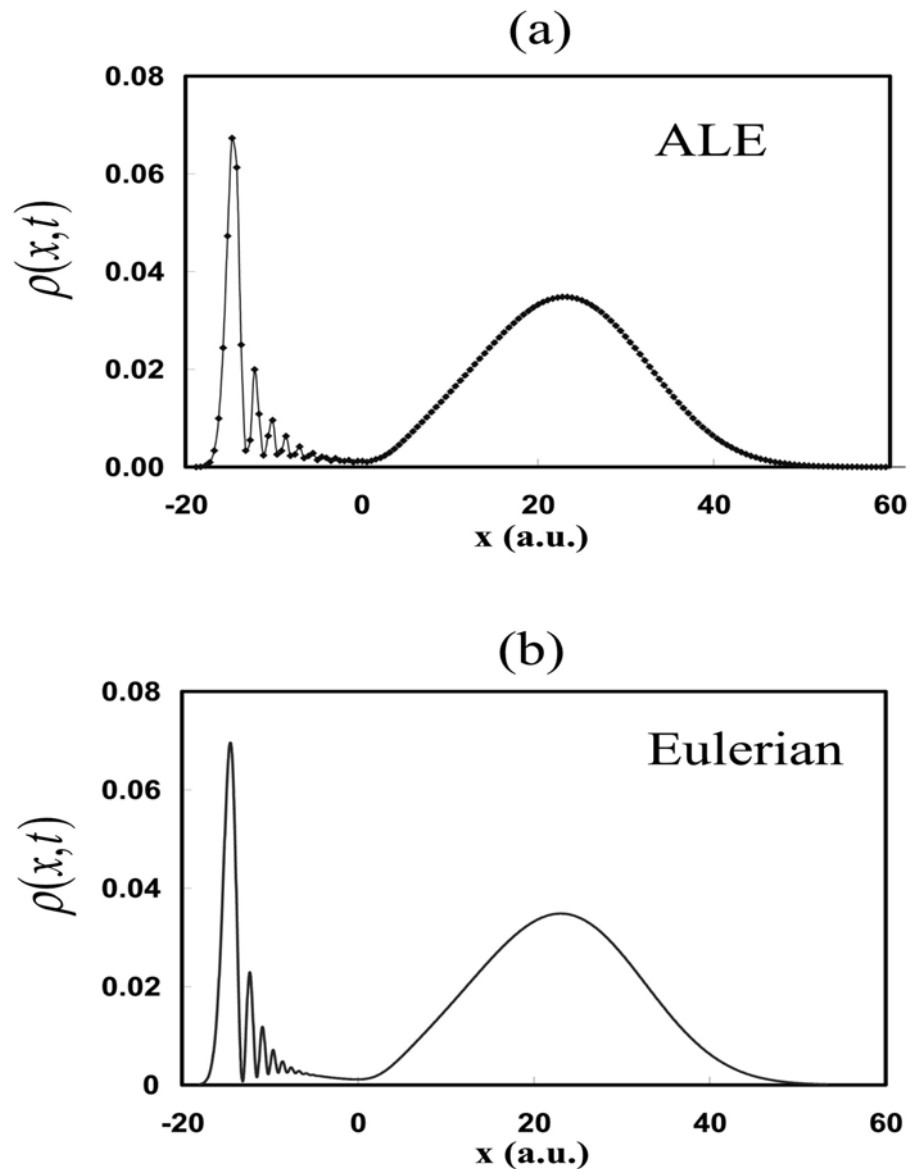


Figure 3.16. Density plots at $t = 125$ fs for the uphill ramp potential of maximum height 6000.0 cm^{-1} . Part (a) displays the results obtained with the ALE/spring method, while part (b) shows results obtained using the Eulerian (fixed-grid) method. The Eulerian results (solid line) were obtained using 4th order Runge-Kutta for time integration and 4th order finite differences for spatial derivatives. The circles connected by linear splines represent the results of the ALE/spring method and are the positions of the grid points at this time.

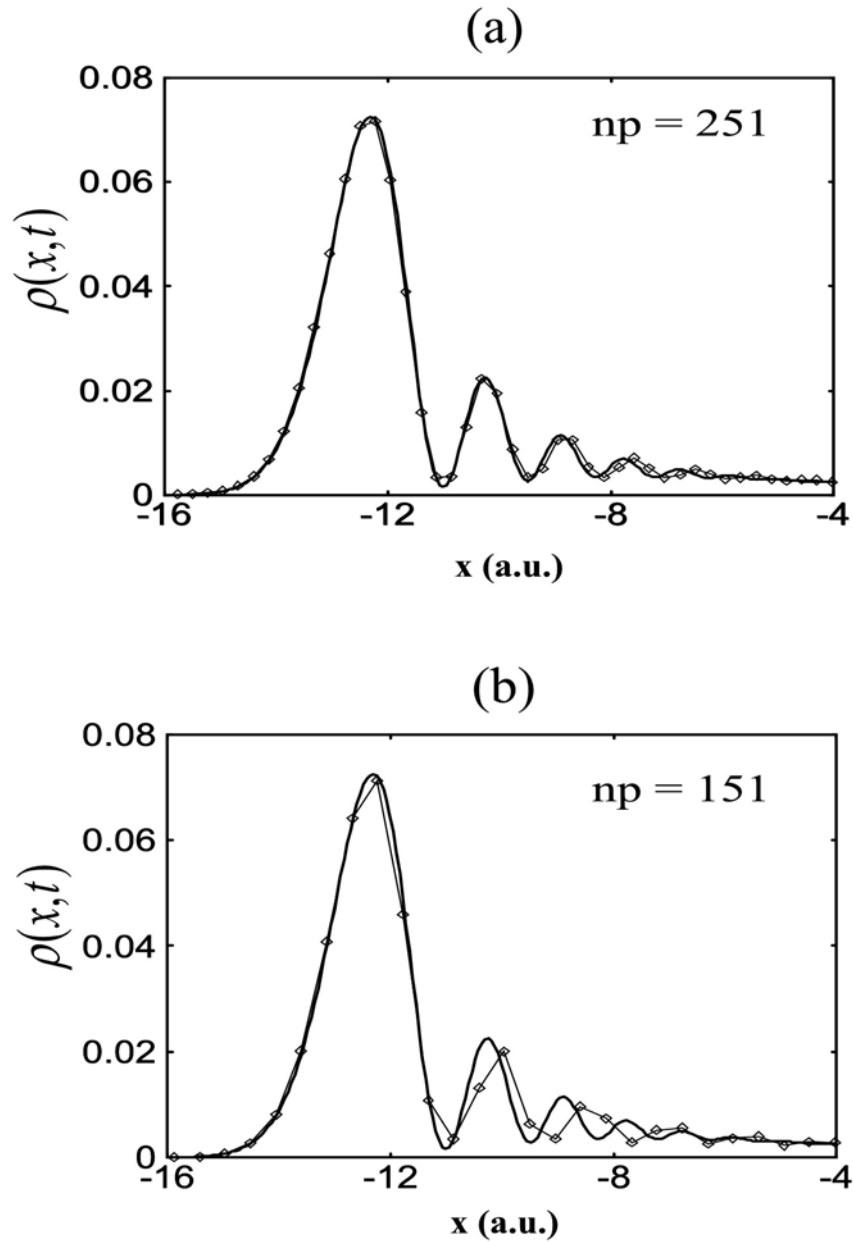


Figure 3.17. Density plots at $t = 110$ fs for the uphill ramp potential with a height of 6000 cm^{-1} . Part (a) shows the results for the ALE/spring method with 251 grid points, while part (b) displays the results for the ALE/spring method with 151 grid points. The solid line was calculated from a fixed-grid, finite difference method with 7,150 grid points.

interpolation routine, which are greatest in regions of large gradient/curvature. By increasing the number of grid points in these regions, interpolation errors are decreased and more accurate solutions can be obtained. It should be noted that, although the number of grid points in the ALE/spring method was increased to 251, this was still only a fraction of the total number of grid points used for the Eulerian fixed-grid results.

3.4.4. ALE discussion

The results of implementing the ALE/spring method on the uphill ramp potential confirm its superiority over both the Lagrangian QTM and the Eulerian ψ -propagator for this problem. It has been shown that the ALE method can provide accurate transmission probabilities for very long times when applied to the uphill ramp, whereas the QTM gives early computational break down. Also, the ALE/spring method requires only a fraction of the number of grid points of the Eulerian calculations while providing nearly the same accuracy in the solution. In two recent studies by B. Kendrick and D. Pauler at Los Alamos [57-58], this exact ALE algorithm was applied to the Eckart Barrier problem in one and two-dimensions. In addition, Kendrick added an artificial viscosity term to *smooth out singularities* in nodal regions. This combination of ALE and “artificial viscosity” had never been used before to solve the QHEM. Many trial wave packet energies were launched against the Eckart barrier, and excellent agreement was obtained when the time-dependent transmission probabilities were compared to that of a fixed-grid, ψ -propagator. Although the exact quantum potential was not solved for in this case (because of the artificial viscosity term), Kendrick’s results are very promising.

Although the ALE method can be utilized for some problems where QTM fails, it is to date, not fully capable of representing the *exact* solutions of R and S in nodal regions without spatial smoothing. In the end, the ALE method continues to have the same problems as the QTM, amplitude nodes and quasi-nodes. These QTM problems were elaborated on previously using an Eckart barrier example.

3.5. CHAPTER CONCLUSION

In this chapter, two numerical methods for solving the quantum hydrodynamic equations of motion were discussed. These methods are the quantum trajectory method and the arbitrary Lagrangian-Eulerian method. For wave function dynamics on simple potential energy surfaces (those without much interference), the QTM works wonderfully and the numerical benefits of solving the QHEM are overwhelming when compared to standard wave function propagators. However, in problems where nodes and quasi-nodes are encountered, the QTM quickly breaks down. If these nodal problems are aggravated by inflation and compression, the ALE method can be used. In some cases, such as the uphill ramp potential, the ALE method can greatly extend the survival time of the algorithm. Nevertheless, simply eliminating inflation and compression does not always solve the node problem. Today, many continue to advance these methods in hopes to one day circumvent the nodal problem.

In one such attempt, a series of hybrid methods using both the Schrödinger equation and the QHEM were developed. In the first of these methods, presented by Wyatt [25], moving external grid points follow Lagrangian trajectories calculated by the QTM. These particles constitute what is called a “frame”. Internal grid points, within

one or more “windows” follow *non-Lagrangian paths* of equal spacings between the Lagrangian frame (see Fig. 3.18). Within these windows, problems encountered with quantum trajectories near amplitude nodes are circumvented by solving the moving path transform of the Schrödinger equation,

$$i \hbar \frac{d\psi(\vec{r}, t)}{dt} = \left[-\frac{\hbar^2}{2m} \nabla^2 + V(\vec{r}, t) + i \hbar \dot{\vec{x}} \cdot \vec{\nabla} \right] \psi(\vec{r}, t). \quad (3.42)$$

(Note that if $\dot{\vec{x}} = 0$ in this equation, the standard fixed-grid Schrödinger equations is obtained.) Using this method, excellent results were obtained for the evolution of a wave packet in a double well potential.

In another similar study [28], Hughes and Wyatt used the same frame and window method. Only this time, a spatially and temporally smoothed equidistribution algorithm was used to guide the ψ – window grid points into regions where high wave function resolution was needed (inside the window). In addition, the ALE method was used to guide all *external* frame points to be equally spaced. The only Lagrangian points used were the first and last grid points. Good results were obtained when this method was applied to an Eckart barrier.

One setback in progression of these hybrid methods is that they are not trivially extended into multi-dimensions. While opening and closing windows is not a problem in 1D, it can be difficult on multi-dimensional grids. In addition, it is very difficult to “link” the QTM frame points with those in the ψ – window. This is because two different equations of motions are used, and they may not be accurately time integrated using the same time-step and methods of derivative approximation. However, the 1D results

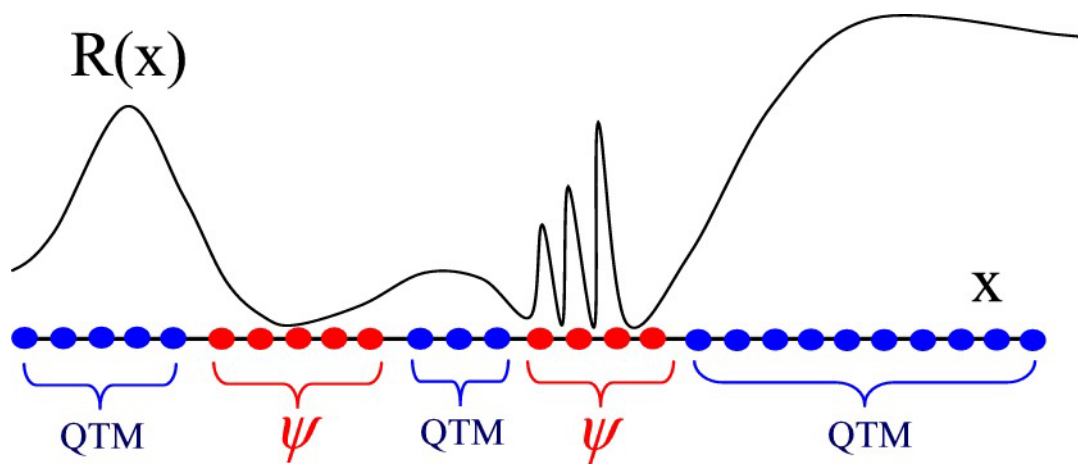


Figure 3.18. A pictorial description of the hybrid method used by Wyatt and Hughes to calculate wave packet dynamics in nodal regions. Particle grid velocities calculated using the QTM were Lagrangian (QHEM), while the particles velocities inside the ψ – windows were non-Lagrangian (TDSE).

obtained using these hybrid methods are very promising, and currently these algorithms are being further developed.

In the next chapter, yet another method for integrating the QHEM, called the derivative propagating method (DPM), will be described. In this method, the hydrodynamics fields, $R(C)$ and S , are propagated in time along with their spatial derivatives. In this manner, trajectories can be solved independently of one another and calculated *one at a time*. In the QTM and ALE method, the entire ensemble of particles must be propagated simultaneously, since the evolution of each trajectory depends algorithmically on its neighbors from the fitting routines.

Chapter 4: The Derivative Propagating Method (DPM)

4.1. DPM BACKGROUND

In chapter three, the quantum hydrodynamic equations of motion were derived and the QTM and ALE method were used to obtain their numerical solutions. In these methods, fitting or interpolation algorithms were utilized to calculate the spatial derivatives needed for substitution into the QHEM. Although these methods for derivative approximation can provide excellent results for some problems, it was shown that terminal problems can arise with their utilization. The first of these problems is encountered when fitting is required in a non-Eulerian propagation scheme. In moving frames, particles follow trajectories governed by a pre-determined equation of motion. If the propagation scheme is Lagrangian, for example, the particle velocities are the same as the flow velocity of the fluid, as discussed in chapter three. In time, these Lagrangian particles can form an unstructured mesh. The irregularity in the grid point locations increases the chances that terminal errors will occur in the derivative approximation methods. These errors, as previously discussed, are due to inflation and compression. In addition to this difficulty, fitting and interpolation methods are *algorithmically non-local*. This means that in order to accurately approximate derivatives at specific trajectory locations, information from nearby particles is needed. The problem created by this type of non-locality is that all particles must be propagated simultaneously as a correlated ensemble, and if one trajectory goes bad, the propagation of the entire ensemble is terminated. Lastly, these routines can consume a great deal of computational time, depending on the number of particles used and whether matrix decomposition is needed.

In this chapter, a new method for obtaining solutions to smooth, initial value PDEs is described. It is called the derivative propagating method (DPM). This method was first described by Trahan, Hughes, and Wyatt in 2003 [29]. In the DPM, equations of motion for both the PDE of interest and its spatial derivatives are propagated in time concurrently. The various orders of derivatives are coupled together in an infinite hierarchy, but low order truncations of this set can lead to useful and accurate approximations. An enormous benefit of the DPM is that *single quantum trajectories may be propagated, and fitting is no longer required to compute the spatial derivatives of the time-dependent PDE*. This in turn can lead to orders of magnitude reduction in the propagation time. In the next section the DPM will be described in detail.

4.2. DERIVATION OF THE DPM

In the DPM, the spatial derivatives are propagated in time along trajectories according to exact equations of motion. The equations of motion for these derivatives are easy to derive for any partial differential equation. As an example, the DPM will be formulated for a generic evolutionary equation given by

$$\frac{\partial W(q,t)}{\partial t} = F(q,t;W, \frac{\partial W}{\partial q}, \frac{\partial^2 W}{\partial q^2}, \dots). \quad (4.1)$$

To begin, both sides of Eq. (4.1) are spatially differentiated and the order of the q and t partial derivatives switched. By doing this, the *analytical equation of motion* for an arbitrary n th order spatial derivative becomes

$$\frac{\partial}{\partial t} \left(\frac{\partial^n W(q,t)}{\partial q^n} \right) = \frac{\partial^n F(q,t)}{\partial q^n}. \quad (4.2)$$

To demonstrate how this procedure leads to an infinite hierarchy of coupled equations, consider a one-dimensional diffusion equation of the form

$$\frac{\partial W(q,t)}{\partial t} = -\frac{\partial}{\partial q} \left(D(q) \frac{\partial W}{\partial q} \right) = -\frac{\partial D}{\partial q} \frac{\partial W}{\partial q} - D \frac{\partial^2 W}{\partial q^2}. \quad (4.3)$$

In order to apply the DPM and differentiate the products of functions in Eqs. (4.3), the Liebnitz theorem is used. This theorem gives the n th derivative of the product of two functions, $H(q) = F(q)G(q)$, as

$$H_n = \sum_{j=0}^n b(n,j) F_{n-j} G_j, \quad (4.4)$$

where $b(n,j)$ are called the binomial coefficients given by $b(n,j) = n!/[j!(n-j)!]$. (For the rest of this chapter, the order of each spatial derivative will be denoted by a subscript, i.e. $S_n = \partial^n S / \partial x^n$). As an example of this theorem, the fourth derivative of Eq. (4.4) is given by the sum of six terms,

$$H_4 = F_0 G_4 + 4F_1 G_3 + 6F_2 G_2 + 4F_3 G_1 + F_4 G_0. \quad (4.5)$$

Using this relation, the equations of motion for the spatial derivatives of Eq. (4.3) become

$$\partial_t W_n = -\sum_{j=0}^n b(n,j) D_{n-j+1} W_{j+1} - D W_{n+2}. \quad (4.6)$$

It can be seen from this equation that not only is there *up-coupling* to higher order derivatives, but there is also *down-coupling* in the summation. It is the up-coupling, however, that leads to the infinite hierarchy. For arbitrary evolutionary equations, this chain of equations is impossible to solve exactly, however, for a range of problems a suitable truncation can be imposed.

To illustrate the conditions under which truncation allows for accurate solutions, one can approximate the solution of Eq. (4.3) at a given location by the *local Taylor polynomial expansion*

$$W(q, t) \approx \sum_{k=0}^K \frac{1}{k!} W_k(t) (q - q_o)^k. \quad (4.7)$$

If the spatial dependence of the solution is smooth (non-oscillating), only a low-order polynomial is needed and the higher order spatial derivatives will be negligible. Approximating solutions as low-order polynomials to obtain spatial derivatives about a reference trajectory is a common task for those utilizing local least squares, interpolation, and finite-difference methods. In theory, as long as the solution can be fit or expanded to a local polynomial of order K in the spatial coordinate using any of these methods, the DPM can be accurately truncated so that the partial derivatives $\partial W^n / \partial q^n$ can be set to zero for $n > K$.

In our studies we have found that the DPM is not particularly sensitive to any specific genre of initial value PDEs. It was found, however, that certain initial conditions (especially those that are highly oscillatory in space, such as the complex-valued wave function) would not propagate with any order of the DPM. The reasons for this are still under investigation. However, as long as the PDE's solutions were smooth for all times, the DPM can be successfully used.

4.3. THE DPM AND THE QHEM

4.3.1. Derivation the DPM/QHEM

Recall the fixed-grid versions of the QHEM presented in chapter three,

$$\frac{\partial C}{\partial t} = -\frac{1}{2m}[S_2 + 2C_1 S_1],$$

$$\frac{\partial S}{\partial t} = -\frac{1}{2m}(S_1)^2 + \frac{\hbar^2}{2m}[C_2 + (C_1)^2] - V. \quad (4.8)$$

If the hydrodynamic solutions are Taylor expanded about x_o ,

$$C(x, t) = c_o(t) + c_1(t)\Delta x + \frac{1}{2}c_2(t)\Delta x^2 + \dots, \quad (4.9)$$

$$S(x, t) = s_o(t) + s_1(t)\Delta x + \frac{1}{2}s_2(t)\Delta x^2 + \dots,$$

(where $\Delta x = x - x_o$) substituted into Eqs. (4.8), and the limit is then taken as $\Delta x \rightarrow 0$, a hierarchy of coupled equations of motion for the expansion coefficients can be derived. If both expansions are truncated at the quadratic level, these equations are given explicitly by

$$\frac{\partial c_0}{\partial t} = -\frac{1}{2m}[s_2 + 2c_1 s_1], \quad \frac{\partial s_0}{\partial t} = -\frac{1}{2m}(s_1)^2 + \frac{\hbar^2}{2m}[c_2 + (c_1)^2] - V, \quad (4.10)$$

$$\frac{\partial c_1}{\partial t} = -\frac{1}{2m}[2c_1 s_2 + 2c_2 s_1], \quad \frac{\partial s_1}{\partial t} = -\frac{1}{2m}[2s_1 s_2] + \frac{\hbar^2}{2m}[2c_1 c_2] - V_1,$$

$$\frac{\partial c_2}{\partial t} = -\frac{1}{2m}[4c_2 s_2], \quad \frac{\partial s_2}{\partial t} = -\frac{1}{2m}[2(s_2)^2] + \frac{\hbar^2}{2m}[2(c_2)^2] - V_2.$$

These equations are rather simple in form and can be integrated extremely fast. Using the Liebnitz relation, the *generalized one-dimensional DPM equations of motion for the QHEM* are

$$\frac{\partial C_n}{\partial t} = -\frac{1}{2m} \left[S_{n+2} + 2 \sum_{j=0}^n b(n, j) S_{1+j} C_{1+n+j} \right], \quad (4.11)$$

$$\frac{\partial S_m}{\partial t} = -\frac{1}{2m} \left[\sum_{j=0}^m b(m, j) S_{1+j} S_{1+m-j} \right] + \frac{\hbar}{2m} \left[C_{m+2} + \sum_{j=0}^m b(m, j) C_{1+j} C_{1+m-j} \right] - V_m.$$

Again, both up-coupling and down-coupling are present in both equations. In these equations is not necessary that $n = m$. For example, zero order in C and first order in S will give a time-dependent WKB type approximation in which the particles follow a classical trajectory.

Equations (4.11) are a system of coupled, non-linear differential equations expressed in the Eulerian frame. To apply the DPM in the Lagrangian or ALE reference frames, the relation $d/dt = \partial/\partial t + \dot{x}(t)(\partial/\partial x)$ is substituted into these equations. Upon doing this, the DPM solutions along an arbitrary path $x(t)$ become,

$$\begin{aligned} \frac{dC_n}{dt} &= \frac{\partial C_n}{\partial t} + \dot{x}(t)C_{n+1}, \\ \frac{dS_m}{dt} &= \frac{\partial S_m}{\partial t} + \dot{x}(t)S_{m+1}. \end{aligned} \quad (4.12)$$

For the special but important case of a Lagrangian path, the path velocity is gradient driven and matches that of the fluid, $\dot{x}(t) = (1/m)S_1$.

With quadratic expansions for $C(x, t)$ and $S(x, t)$ the wave function synthesized around each fluid element is a local Gaussian. However, this does this imply that the *global* wave function is of the Gaussian form. Beginning with Heller's studies just over 25 years ago [59], frozen or thawed (fixed or variable width) Gaussians have been used in many semi-classical studies of time-dependent processes. A significant difference between the latter studies and this one is that in the DPM, quadratic expansions (or higher, if necessary) for the amplitude and phase of the wave function are propagated

along each trajectory, rather than for the global wave function. In this sense, the DPM is an extension of Heller's earlier studies.

Within the hydrodynamic formulation, a different infinite hierarchy of equations has been described [60-61]. In that study, position space equations of motion were derived for momentum moments of the Wigner function. For pure states, the hierarchy terminates at the second moment, but the formalism is also applicable to mixed states, where all moments are coupled. The hierarchy described in these studies is different from that developed in the DPM, since in this method, the spatial derivatives are propagated rather than momentum moments of a phase space distribution function.

The DPM may be readily extended to solve the QHEM in D-dimensions, although the resulting equations are more complicated than those presented earlier. For example, in two degrees of freedom, the partial derivative of the dot product of two gradients, $\vec{\nabla}S \cdot \vec{\nabla}C = S_{(1,0)}C_{(1,0)} + S_{(0,1)}C_{(0,1)}$, is given by

$$(\vec{\nabla}S \cdot \vec{\nabla}C)_{(n,m)} = \sum_{j=0}^n \sum_{k=0}^m b(n,j)b(m,k) [S_{(1+j,k)}C_{(1+n-j,m-k)} + S_{(j,1+k)}C_{(n-j,1+m-k)}], \quad (4.13)$$

where the following notation is used for the partial derivatives:

$S_{(n,m)} = \partial^n \partial^m S(x, y, t) / \partial x^n \partial y^m$. In terms of the derivative in Eq. (4.13), equations of

motion for the derivatives of C and S are

$$\partial_t C_{(n,m)} = -\frac{1}{2m} [S_{(2+n,m)} + S_{(n,2+m)} + 2(\vec{\nabla}S \cdot \vec{\nabla}C)_{(n,m)}], \quad (4.14)$$

$$\partial_t S_{(n,m)} = -\frac{1}{2m} (\vec{\nabla}S \cdot \vec{\nabla}S)_{(n,m)} + \frac{\hbar^2}{2m} [C_{(2+n,m)} + C_{(n,2+m)} + (\vec{\nabla}C \cdot \vec{\nabla}C)_{(n,m)}] - V_{(n,m)}$$

These equations, and their multi-dimensional extensions, can be readily programmed.

Of course, because of the increasing number of derivatives, the computational cost for each trajectory increases with dimensionality. For example, using quadratic expansions for C and S in D -dimensions, we can work out that there are $(D+1)(D+2)/2$ equations of motion for each function and its derivatives. As an example, in four dimensions C has 14 spatial derivatives that need to be propagated in time. These derivatives are

$$\begin{aligned}
& C_{(1,0,0,0)}, C_{(0,1,0,0)}, C_{(0,0,1,0)}, C_{(0,0,0,1)} \\
& C_{(2,0,0,0)}, C_{(0,2,0,0)}, C_{(0,0,2,0)}, C_{(0,0,0,2)} \\
& C_{(1,1,0,0)}, C_{(1,0,1,0)}, C_{(1,0,0,1)} \\
& C_{(0,1,1,0)}, C_{(0,1,0,1)} \\
& C_{(0,0,1,1)}
\end{aligned} \tag{4.15}$$

At the second order, there will thus be 15 equations of motion for C , those in Eq. (4.15) and the original C -equation.

For this reason, use of DPM expansions beyond the quadratic or cubic level may not be practical in high dimensionality, since a large number of derivatives must be propagated. However, implementation at the ‘cheap’ quadratic level dresses what would otherwise be a bare classical trajectory with an approximate quantum potential and its derivatives. Propagation at the quadratic level is feasible and, as an example, this approach has been implemented in a scattering code that handles *ten degrees of freedom!*

4.3.2. Implementation and DPM/QHEM

The following steps can be followed in order to build a computer code to run the DPM. To be specific, assume that we are operating at the quadratic level, so that the six functions and derivatives, denoted $\Phi = \{C, C_1, C_2, S, S_1, S_2\}$, are computed along each

trajectory at each time step. At $t = 0$, the start of the trajectory, these six quantities must be specified; we will return to the initial conditions at the end of this section. For now, assume that one trajectory has been followed for n time steps, where the time step is denoted Δt . At this time, the trajectory is located at position x , and it has the momentum $p = \vec{\nabla}S = S_1$. In order to advance one time-step, the following procedure can be followed (as taken from [120]).

1. Using information provided by the set Φ , compute the set of Eulerian time derivatives, $\partial\Phi/\partial t$. Equations (4.8) and (4.10) are used for this purpose.
2. Convert the time derivatives to the moving frame using Eqs. (4.12).
3. Using the current functions and their derivatives in the moving frame, update the set Φ . In the simplest integration scheme, first order Euler, this can be done using the equation $C_n(t + \Delta t) = C_n(t) + (dC_n/dt)\Delta t$. The same equation is used for the S update. (For more accurate solutions, a higher order time-integrator should be used.)
4. Update the trajectory. With an Euler integrator this can be done using the equations:

$$x_{new} = x_{old} + (p_{old}/m)\Delta t \text{ and } p_{new} = p_{old} + F_{old}\Delta t, \quad (4.16)$$

where $F_{old} = -(\partial V/\partial x)_{x_{old}}$. Again, a higher order integrator could be used for this update as well.

5. After both the trajectory and the set of functions and derivatives have been updated, the algorithm is returned to step 1, assuming that solutions are needed at

longer propagation times. This loop is repeated until the final propagation time is reached.

The conditions on the functions and derivatives at the start of the trajectory are determined from the initial wave function. Assume a normalized Gaussian wave packet given by

$$\psi(x,0) = \left(\frac{2\beta}{\pi}\right)^{1/4} \exp[-\beta(x-x_o)^2] \exp[ik(x-x_o)], \quad (4.17)$$

where $\beta = 1/(4\sigma^2)$. In this equation, the C and S amplitudes are given by

$$\begin{aligned} C(x,0) &= \ln(2\beta/\pi)^{1/4} - \beta(x-x_o)^2, \\ S(x,0) &= \hbar k (x-x_o). \end{aligned} \quad (4.18)$$

As a result, the only non-zero initial x -derivatives are

$$C_1 = -2\beta(x-x_o), \quad C_2 = -2\beta, \quad (4.19)$$

$$S_1 = \hbar k. \quad (4.20)$$

With the values given in Eqs. (4.19) and (4.20), the trajectory may be launched from position x at $t = 0$.

4.3.3. Applications of the DPM/QHEM

4.3.3.1. *The meta-stable well*

In order to demonstrate some features of the derivative propagation method, computational results will be presented for two model problems. The first of these concerns the decay of a wave packet launched from the quasi-bound region of the

potential $V(x) = (1/2)kx^2 - \gamma kx^3$. The force constant $k = 4.05 \cdot 10^{-3}$ is chosen so that the harmonic term reaches 2000 cm^{-1} when $x = 1.5$. (Once again, unless otherwise stated all units are atomic) In addition, the value $\gamma = 0.14$ was used. The resulting potential, see Fig. 4.1, displays a near-harmonic bowl around $x = 0$ and reaches a local maximum near $x = 2.4$, where the potential is 1680 cm^{-1} . The potential drops to zero at $x^* = 3.57$ and becomes increasingly negative as x increases. The center of the initial Gaussian distribution is $x_o = -0.5$, the width parameter $\beta = 6$, the initial translational energy is set to zero, and the mass is $m = 2000$.

In this example, the aim is to compute the time-dependent correlation function. This function measures the degree of overlap between the complex wave function and a predetermined test function, which will be centered at x^* . The correlation function is given in one-dimension by

$$C(t) = \langle \psi(x, t) | \phi(x) \rangle = \int_{-\infty}^{\infty} \psi(x, t) \phi(x) dx, \quad (4.21)$$

where $\phi(x)$, the test function, is chosen as a delta function at x^* for this application (i.e. $C(t) = \langle \psi(x, t) | \delta(x - x^*) \rangle = \psi(x^*, t)$). Correlation functions are often used in wave packet dynamics to obtain absorption spectra and energy resolved transmission probabilities.

Because the time dependence of the wave function was computed at a single fixed grid point, the hydrodynamic DPM equations of motion were integrated in the Eulerian, fixed in space, representation. Using the third order DPM, eight coupled equations of motion for C and S and their first three spatial derivatives were propagated. The resulting

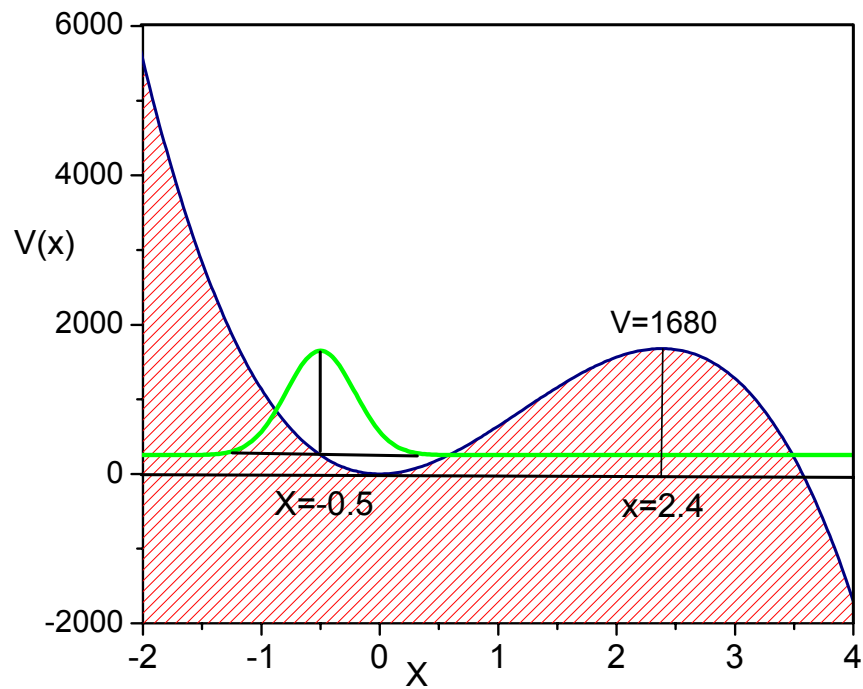


Figure 4.1. The cubic potential used to study the decay of a metastable state (the potential is in cm^{-1}). The initial Gaussian wave function (multiplied by 10^3 and then shifted up by 253 cm^{-1}) is also shown.

correlation function is shown in Fig. 4.2. It is in excellent agreement with results obtained when propagating the TDSE on a fixed grid of 3000 points. *Use of the DPM thus permitted the correlation function to be obtained through the ultimate compactification of the Eulerian grid to a single point!* This is quite an unbelievable accomplishment.

4.3.3.2. *The Eckart barrier*

The second application of the DPM concerns computation of the energy resolved transmission probability $P(E)$ from the time-dependent scattering of a wave packet off a repulsive barrier. Equations relating time-dependent scattering to energy resolved quantities were developed and applied by Tannor and Weeks [62]. This topic is also described in the books by Tannor [63] and by Zhang [64]. Tannor and Weeks showed that $P(E)$ may be computed from the Fourier transform of the cross-correlation function

$$P(E) = \left(\frac{k}{m}\right)^2 \sqrt{\frac{\beta}{2\pi}} \exp\left[\frac{(k-k_o)^2}{2\beta}\right] \left| \int_0^\infty C_{\alpha,\chi}(t) \exp[iEt] dt \right|^2, \quad (4.22)$$

where the wave number corresponding to translational energy E is given by $k = \sqrt{2mE/\hbar^2}$, k_o is the wave number corresponding to the initial wave packet translational energy E_o , and the width parameter for the initial Gaussian wave packet is denoted $\beta = 1/(4\sigma^2)$. The cross-correlation function, $C_{\alpha,\chi}(t)$, between the wave packet $\psi_\alpha^{(+)}(x,t)$ launched from the reactant region ($x \rightarrow -\infty$) and a stationary test function, $\phi_\chi^{(-)}(x) = \delta(x-x^*) \exp[-ikx]$, located at position x^* on the product side of the barrier (centered at $x=0$) is given by $\langle \psi_\alpha^{(+)} | \phi_\beta^{(-)} \rangle$. In this example, the Eckart potential

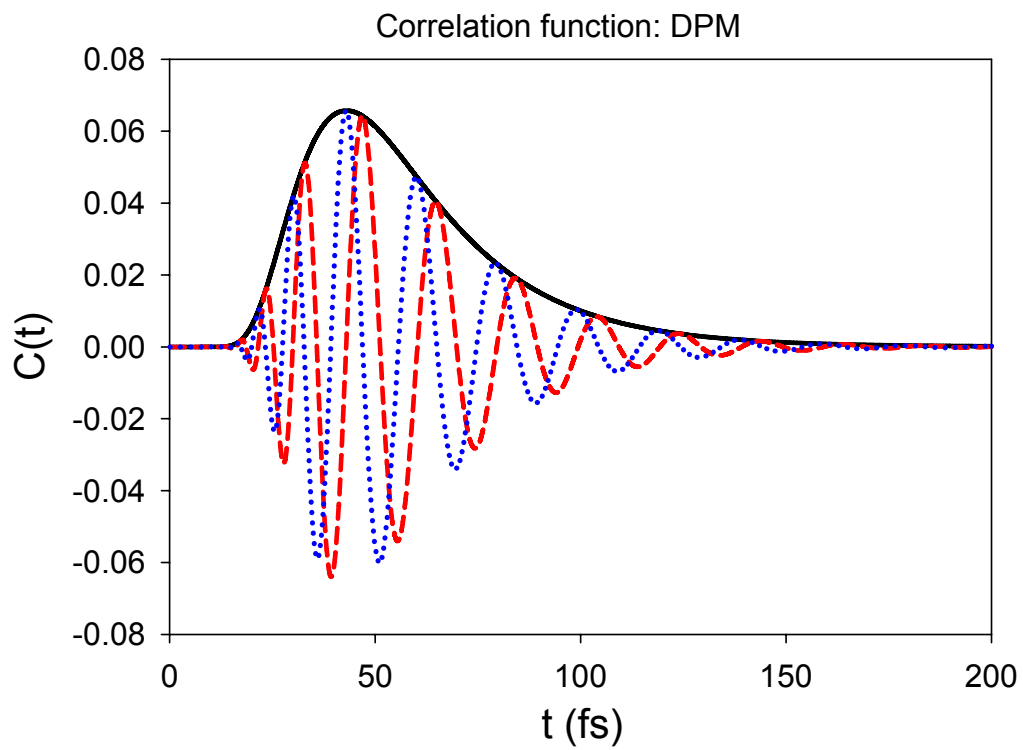


Figure 4.2. This figure displays the correlation function calculated at one point by the Eulerian version of the DPM for the cubic potential. The real and imaginary parts of $C(t)$ are shown by dashed and dotted lines, respectively.

$V(x) = V_o \sec^2(\kappa x)$ is used with a height $V_o = 3000 \text{ cm}^{-1}$ and width parameter $\kappa = 1.2$.

The initial Gaussian wave packet was given a translational energy $E_o = 3000 \text{ cm}^{-1}$ and was centered at $x_o = -6$. The test function used to monitor the wave function in the product region was located at $x^* = 5$.

Originally, many trajectories representing the whole initial wave packet were propagated in time. However, those DPM trajectories that were guided close to amplitude nodes in the reflected region did not survive. The reason for this failure is still under investigation. There are several possibilities. One possible explanation is that when a trajectory traverses close to a node or quasi-node, the hydrodynamic solutions may not only have large gradients and curvatures, but they may also have significant high-order derivatives not represented by a truncated low order DPM algorithm. In fact, these high-order derivatives could be quite large in magnitude. In addition to this, the truncated system of DPM differential equations for C and S and their derivatives may become stiff in these regions, with different scales and rates of change for the functions and their various derivatives. If this is the case, then special numerical integration algorithms for stiff systems (i.e., implicit integrators) should be used.

Because the reflected trajectories did not survive and were completely useless, a second attempt was made to follow only those trajectories transmitted into the product region, since this was the region of the test function, and the hydrodynamic solutions were quite smooth there. In this approach, quantum trajectories were fired, one-at-a-time, toward the barrier with initial position values in the interval $x_{back} \leq x \leq x_{front}$, where x_{front} is a point on the leading edge of the wave packet where the density is very low.

The starting point for each successive trajectory was then moved back, away from the barrier, until the bifurcation point x_{back} was found. For all starting positions $x > x_{back}$, the trajectories make it over the barrier. However, for starting positions $x < x_{back}$, the trajectories evolve to form the non-reactive portion of the wave packet. For these calculations, $x_{front} = -3.5$, and it was found that $x_{back} = -6.0001$.

Using second order DPM trajectories, the cross-correlation function over the time interval 14–147 fs was computed using the reactant trajectories and is shown in Fig. 4.3. The peak of the transmitted wave packet passes the monitor point in the product channel about 70 fs after launching the packet from the reactant side of the barrier. At this point, $P(E)$ was calculated using Eq. (4.22) and the Fourier transform of $C_{\alpha,\chi}(t)$. The analytical transmission probability for the Eckart barrier (this is worked out as an exercise in Landau and Lifshitz [65]) is shown in Fig. 4.4. This figure also shows the DPM results for both second and third order expansions. The DPM curves capture the energy dependence of the transmission probability, including the low-energy tunneling region, but the curve for second order DPM slightly over-estimates $P(E)$ in the energy range 3200–4500 cm^{-1} . However, the curve obtained using third order DPM is in good quantitative agreement with the analytic result. Some of the reactive quantum trajectories were propagated for long times, up to 2.5 ps, and they were completely stable.

4.3.4. DPM/QHEM discussion

In this section, it was demonstrated for the first time that quantum trajectories can be propagated one-at-a-time using a new method for wave packet propagation called the

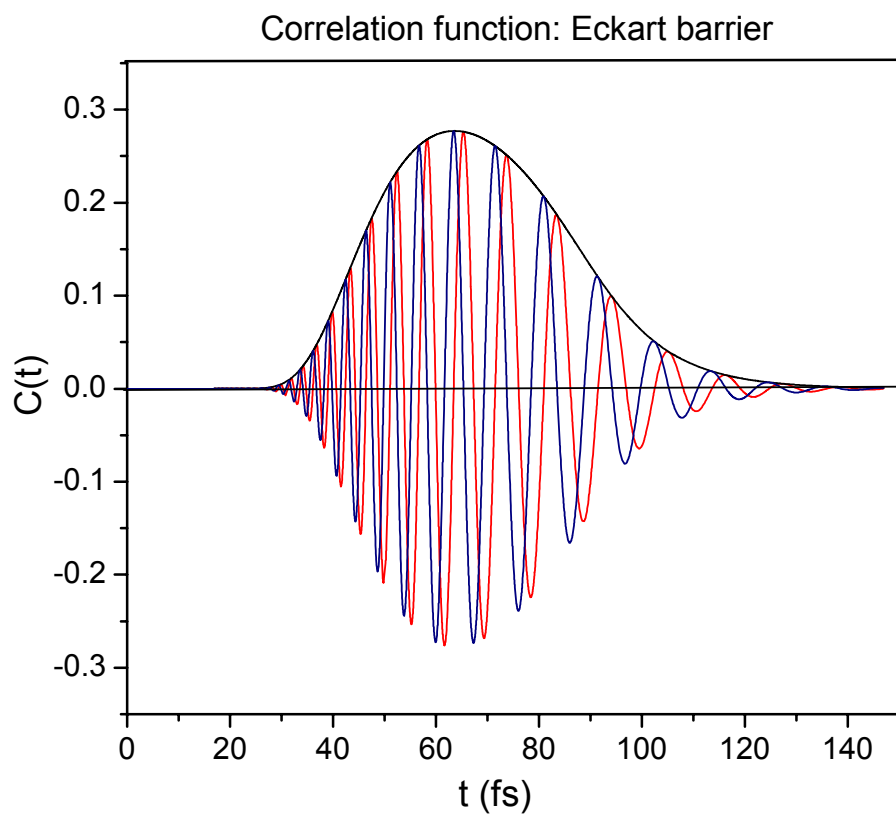


Figure 4.3. This figure displays the correlation function for the Eckart barrier. The real part of the correlation is in red, and the imaginary part is in blue.

derivative propagating method. Non-locality is introduced into the QHEM by propagating the spatial derivatives of the fields surrounding each quantum trajectory. Two one-dimensional examples were presented, one of which used a non-polynomial potential energy function which could not be naturally truncated. The results were in good agreement with solutions obtained from standard TDSE integrators. In addition to these examples, Bittner combined the DPM with an initial value representation to compute the autocorrelation and spectral functions for a wave packet in a Gaussian well [30].

The DPM, however, is not always able to calculate every trajectory for some potentials, even those represented by low order polynomials. For some problems, the solutions about specific trajectories become oscillatory and stiff, preventing low-order truncations from being accurate. This is because the surrounding fields are not brought in to all orders of derivative (or smoothness). The order of the DPM constrains the quantum potential and other spatial derivatives from being completely non-local. In affect, a ‘tube’ can be built around each trajectory that brings in a sort of *regional non-locality*. In regional non-locality, the particle is not aware of the hydrodynamic fields and their changes beyond a limited horizon. This is in contrast to full non-locality, where a particle at some position in space can be influenced by another particle extremely far away. In general, the higher the order of the DPM, the more truly non-local it becomes. An example that brings out one way that DPM trajectories can fail using low-order truncation is the familiar two-slit diffraction experiment.

At present, there is not a way to predict what order of DPM should be used to

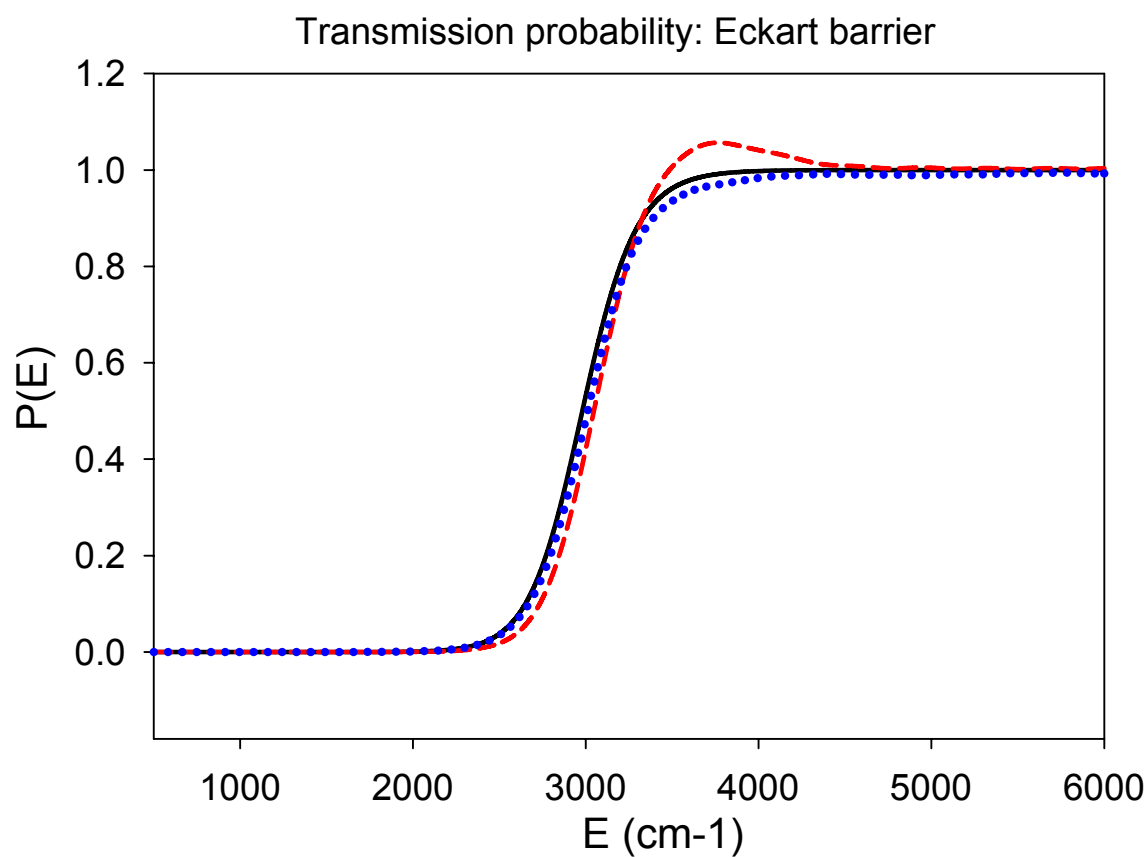


Figure 4.4. Energy resolved transmission probabilities for the Eckart barrier (barrier height $V_o = 3000 \text{ cm}^{-1}$). Second order (dashed red curve) and third order (dotted blue curve) DPM results are compared with the analytic result (solid curve).

generate acceptable results⁵. It would be useful to systematically investigate how the order of the DPM affects the results of some different problems. In addition, to increase the adaptability of the DPM algorithm, the order for each trajectory should be calculated on the fly by monitoring the solution smoothness in some manner. This could be done, for example, by monitoring the change in solutions as the DPM order is increased by one. If the solutions are the same in both orders, then the current approximation is fine. It may in fact be that for some trajectories, such as those encountered in the nodal regions of the Eckart barrier, it is not possible to truncate. In this case, a hybrid method should be developed to incorporate the DPM and the QTM, ALE, or TDSE. The combination possibilities are endless.

To end on a positive note, thousands of trajectories needed for multi-dimensional problems are now being calculated using parallel DPM codes. This process has never been so easy. In addition, in problems that require integration and solutions in regions where the hydrodynamic solutions are smooth, such as the Eckart barrier product region, the DPM can give excellent results. The QTM and ALE method for these problems fail, since blow-ups in the reflected regions terminate the entire algorithm. In the DPM, it does not matter if the trajectories in the reflected region are inaccurate, since they are completely decoupled from each other and those transmitted.

⁵ Fortunately, it is quite easy to physically see when trajectories blow-up, since these paths are erratic and incoherent.

4.4. THE DPM AND PHASE SPACE DYNAMICS

4.4.1. Phase space background

In the previous section of this chapter, the DPM was used to propagate solutions of the QHEM. Implementation of this method, however, is not limited to these equations of motion. In this section, the DPM will be applied to a completely different kind of initial value PDE. In this manner, the point is emphasized that the application of the DPM is not governed by a specific genre of PDEs, but rather the smoothness of their solution and initial conditions.

The time evolution of quantum systems is frequently computed and analyzed in position or configuration space. The quantum trajectories described in the preceding sections of this dissertation were developed in this way. For isolated systems, this is a natural way to proceed. However, for open quantum systems, or those coupled to an environment such as a thermal reservoir, equations of motion are often developed and solved in phase space. This is because in configuration space, the equations of motion are randomly fluctuating due to Brownian forces that arise from the thermal reservoir. These stochastic terms make numerical integration extremely difficult, since their corresponding solutions are erratic and non-smooth. It will be shown, that these indeterministic forces are averaged out, and deterministic solutions to the same problem can be propagated in phase space.

In phase space, a set of coordinates consists of all position and momentum degrees of freedom. For example, if the problem is one-dimensional in configuration space, a two-dimensional phase space distribution, $W(x, p, t)$, is needed. In two-dimensional configuration space, a four-dimensional phase space distribution must be

solved, corresponding to $W(x, y, p_x, p_y)$. This two-fold increase in dimensionality is one deterrent of phase space dynamics. However, two important advantages of phase space calculations over those in configuration space, other than these calculations being deterministic as opposed to stochastic, are that they provide a more detailed visualization of the underlying dynamics of a problem, and many more average values can be calculated directly in terms of $W(x, p, t)$.

There are many phase space equations of motion, depending on whether the distribution evolution is closed, open, classical, quantum, or in some cases, positive definite. For an *isolated classical system*, the Liouville equation describes the evolution of the distribution function. This equation and some characteristics of its phase space flow are described in the next section. When the classical system is allowed to interact through friction terms with a thermal bath, the distribution function evolves according to the Klein-Kramers (KK) equation. For an *isolated quantum system*, the Wigner equation is used to propagate phase space Wigner distributions. Because this function may develop negative basins, smooth positive semi-definite distributions, such as the Husimi function, are also frequently propagated. When the *quantum subsystem is coupled to an environment*, the equations of motion become more complicated. For this case, the Caldeira-Leggett evolutionary equation is widely studied. The derivation and study of those equations of motion for open systems remains an active area of research.

It has only been within the past few years that quantum trajectories have been used to solve phase space equations of motion. This area of research was stimulated when Donoso and Martens (DM) described a novel method for evolving both classical

and quantum phase space distributions using an ensemble of “entangled” trajectories [66-68]. These trajectories are entangled through coupling terms in the equations of motion that depend upon q and p derivatives of the phase space density riding along each trajectory. These coupling terms, in both classical and quantum mechanics, introduce non-locality and contextuality (dependence upon the initial state) into the equations of motion. In this respect, non-local terms in the phase space equations of motion are similar to density dependent terms that occur in the quantum potential of the QHEM. Because of this non-local interaction, the trajectory solutions evolve as a unified whole, with each part both influencing and dependent upon the dynamics of every other part.

Shortly after Donoso and Marten’s study, Trahan and Wyatt used the DPM to obtain Lagrangian trajectory solutions for the Klein-Kramers equation, the Husimi equation, and for a smoothed version of the Caldeira-Leggett equation derived by the Diosi [69]. Trajectory solutions for these equations of motion were obtained for the relaxation of an oscillator in contact with a thermal bath and for the decay of a metastable state. The DPM solutions for the Klein-Kramers and Caldeira-Leggett equations were compared to accurate fixed grid, finite-difference results in a follow-up study [70]. In addition to this, Hughes and Wyatt studied Eckart barrier transmission as a function of the friction coefficient and temperature for the modified Caldeira-Leggett equation and obtained excellent agreement when the DPM was compared to fixed-grid results [71].

In the proceeding sections of this chapter, the results of the DPM applied to the classical Klein-Kramers’ equation of motion will be reviewed. Before doing this, however, the Liouville, Langevin, and KK equations of motion will be described in more

detail. Although all details on these equations cannot be given here (that would take a whole text book!), they are summarized and their major characteristics discussed.

4.4.2. The Liouville, Langevin, and Klein-Kramers equations

In classical mechanics, the evolution of an ensemble of trajectories can be described in several ways. One way is by integrating the classical equations of motion to obtain the coordinate and momentum for each trajectory. These are $\{x(t), p(t)\}$ in one-dimensional configuration space. This trajectory can then be plotted in two-dimensional phase space with axes $\{x, p\}$. The orbit of each of the np trajectories are initiated at $t = 0$, with $\{x_0, p_0\}$, and can then be followed until a specified time t is reached. In a small box of area $\Delta x \Delta p$ around the point (x, p) , the number of trajectories at this time can be given as $\Delta np(x, p, t)$, and the fraction of the total trajectories located in this box is $\Delta np / np$. The probability density in phase space is then defined as

$$W(x, p, t) = \Delta np(x, p, t) / [np \cdot \Delta x \Delta p]. \quad (4.23)$$

Because of the way it is defined, the density is normalized at all times so that

$$\int_{-\infty}^{\infty} \int_{-\infty}^{\infty} W(x, p, t) dx dp = 1. \quad (4.24)$$

The flow of the classical probability density in phase space was addressed by Liouville. He derived an equation, now called the *Liouville equation* [72], for the rate of change in the density at a fixed point, (x, p) , given by

$$\frac{\partial W}{\partial t} = -\frac{p}{m} \frac{\partial W}{\partial x} + \frac{\partial V}{\partial x} \frac{\partial W}{\partial p}. \quad (4.25)$$

From the classical equations of motion, $\dot{x} = p/m$ and $\dot{p} = -\partial V/\partial x$, two components of the phase space velocity vector can be defined. These components are v_x and v_p . In addition, the gradient operator, $\vec{\nabla}$, has two components in 1D phase space, $\{\partial/\partial x, \partial/\partial p\}$. Using these relations, the Liouville equation may be written in the compact form as

$$\frac{\partial W}{\partial t} = -\vec{v} \cdot \vec{\nabla} W . \quad (4.26)$$

Equation (4.26) expresses the Liouville equation in the Eulerian frame. This equation can be converted into the Lagrangian frame using

$$\frac{dW}{dt} = \frac{\partial W}{\partial t} + v_x \frac{\partial W}{\partial x} + v_p \frac{\partial W}{\partial p} = \frac{\partial W}{\partial t} + \vec{v} \cdot \vec{\nabla} W . \quad (4.27)$$

If the Eulerian time-derivative, Eq. (4.26), is substituted into Eq. (4.27), it is found that *the density does not change along the flow*,

$$\frac{dW}{dt} = 0 , \quad (4.28)$$

or stated another way, the density at time t along the flow is the same value that was specified by the initial conditions, $W(t) = W(t_o)$.

Liouville's equation governs the evolution of the classical phase space density in an *isolated system*. We now turn to *open systems*, those which can exchange energy with the surroundings. One example is a system in contact with a '*heat bath*', which is always assumed to be maintained at a temperature T . A classical trajectory evolving in such a system is subject to friction forces that dampen its velocity. These forces are due to coupling between the system and the bath degrees of freedom. The friction force is defined as $F_{friction} = -\gamma m v$, where γ (units of *1/time*) is the phenomenological friction

coefficient. This term acting alone would cause the particle to settle to zero velocity in a minimum on the classical potential surface.

In addition to friction, the system evolves under the influence of the two other contributions to the total force. As usual, there is the classical force arising from the potential $V(x)$, plus an additional *random force* due to interaction with the bath. The latter is also called the *stochastic force*, $F(t)$. For an ensemble of trajectories evolving from the same initial position and momentum conditions, the ensemble average of the stochastic force is assumed to be zero, $\langle F(t) \rangle = 0$. However, the *two-time correlation function* (*force autocorrelation function*) is not necessarily zero,

$$\langle F(t) | F(t') \rangle = C(|t - t'|). \quad (4.29)$$

This expression states that the force at the time t' might be related to the force at some other time t . An important special case occurs when the correlation function is non-zero only when $t' = t$, so that the right side of Eq. (4.29) is proportional to a δ -function, $\langle F(t) | F(t') \rangle = \delta(t - t')$. It can be shown, for this case, that the friction coefficient and the correlation function are related through the *fluctuation-dissipation theorem*

$$\langle F(t) | F(t') \rangle = 2m\gamma k_B T \delta(t - t'), \quad (4.30)$$

where k_B is Boltzmann's constant. This theorem is discussed in textbooks on statistical mechanics [72] and will not be derived here. When the stochastic force is δ -correlated, it is referred to as *white noise* because the Fourier transform of Eq. (4.30) is flat in frequency space. *Colored noise* refers to the more general case where the correlation

function is not δ -spiked, so that the Fourier transform acquires some frequency dependence.

The *stochastic process* for a particle influenced by the three force terms mentioned previously is governed by the *Langevin equation*, which is used to describe Brownian motion in phase space. This equation is given by

$$m \frac{dv}{dt} = -\frac{\partial V}{\partial x} - \gamma m v + F(t). \quad (4.31)$$

One approach to modeling system-bath dynamics is to treat the fluctuating force in Eq. (4.31) as an additive Gaussian noise and solve this equation computationally for each member in an ensemble of np trajectories. Another approach to the stochastic dynamics of an ensemble of particles is to *propagate the density in phase space* using an appropriate equation of motion. By doing this, the stochastic term in the Langevin equation is replaced by a *deterministic* term proportional to the second-order derivative in momentum. In 1940, Kramers derived an important equation [73] that governs the phase space evolution of a subsystem in contact with a heat bath maintained at an equilibrium temperature T . To do this, Kramers invented a model for a condensed phase chemical reaction involving a particle moving in a one-dimensional potential with the remaining degrees of freedom for both the reacting and solvent molecules constituting a heat bath. With this description, he derived what is now called the Klein-Kramers equation given by⁶

$$\frac{\partial W}{\partial t} = -\frac{p}{m} \frac{\partial W}{\partial x} + \frac{\partial V}{\partial x} \frac{\partial W}{\partial p} + \gamma \frac{\partial}{\partial p} \left[p + mk_B T \frac{\partial}{\partial p} \right] W, \quad (4.32)$$

⁶ A straightforward derivation of this equation is given by Billing and Mikkelsen [74].

where the first of the two terms involving γ is the dissipative term and the second one leads to momentum diffusion. The first two terms on the right side are recognized as the convective terms from the Liouville equation. Kramers obtained steady state solutions to this equation for two limiting cases, weak and strong friction. In these limits, Kramers thoroughly investigated the double well potential and was able to analytically derive reaction rate constants for this problem. Since his work, a number of analyses have focused upon determination of the escape rate of a particle initially trapped in a metastable well as a function of both temperature and the friction coefficient. These and other results are described in a comprehensive review article [75].

4.4.3. The DPM/KK equations of motion

In the setup used by Donoso and Martens, phase space Lagrangian trajectories were used to calculate solutions to the KK equation of motion. In order to do this, the Lagrangian velocity vector is needed in phase space. To obtain this, Eq. (4.32) is written in the form of a continuity equation involving the divergence of the probability flux vector, $\vec{J}(x, p, t)$. This gives the equation

$$\frac{\partial W}{\partial t} + \vec{\nabla} \cdot \vec{J} = 0. \quad (4.33)$$

If Eq. (4.32) is substituted into Eq. (4.33), the divergence of the flux can be given by

$$\vec{\nabla} \cdot \vec{J} = \frac{p}{m} \frac{\partial W}{\partial x} - \frac{\partial V}{\partial x} \frac{\partial W}{\partial p} - \gamma \frac{\partial}{\partial p} \left(p + mk_B T \frac{\partial}{\partial p} \right) W. \quad (4.34)$$

From this equation, the flux vector can be easily deduced as

$$J_x = \frac{p}{m} W, \quad (4.35)$$

$$J_p = -\frac{\partial V}{\partial x}W - \gamma \left(p + mk_B T \frac{\partial}{\partial p} \right) W.$$

If the probability flux vector is defined as $\vec{J} = W \vec{v}$, where the velocity phase space vector is $\vec{v} = (v_x, v_p)$, the velocities can be given by

$$\vec{v}(x, p, t) = \frac{1}{W(x, p, t)} \vec{J}(x, p, t). \quad (4.36)$$

Upon substitution of Eqs. (4.35) into Eq. (4.36), the Lagrangian velocity components of the KK equation are found to be

$$\dot{x} = v_x = \frac{p}{m}, \quad (4.37)$$

$$\dot{p} = v_p = -\frac{\partial V}{\partial x} - \gamma \left(p + mk_B T \frac{1}{W} \frac{\partial W}{\partial p} \right).$$

The momentum velocity component in the above equation can be decomposed into a local classical and non-local density dependent part, giving

$$v_p = \frac{dp}{dt} = F_{local} + F_{nonlocal}(W). \quad (4.38)$$

In this equation, the local force term includes the classical force, $-\partial V / \partial x$, plus the dissipative term, $-\gamma p$. The non-local force in this equation involves derivatives of the density field, just as in the quantum potential.

After deriving the KK Lagrangian velocity components, a transformation from the fixed-grid equation, given in Eq. (4.32), to the Lagrangian frame can be made using the relation

$$\frac{dW}{dt} = \frac{\partial W}{\partial t} + \vec{v} \cdot \vec{\nabla} W = -\vec{\nabla} \cdot (\vec{v} W) + \vec{v} \cdot \vec{\nabla} W = -W \vec{\nabla} \cdot \vec{v}. \quad (4.39)$$

This equation can be integrated along the trajectory to give the updated density

$$W(x(t), p(t)) = \text{Exp} \left[- \int_0^t \vec{\nabla} \cdot \vec{v} dt \right] W(x(0), p(0)). \quad (4.40)$$

Equation (4.40) leads to non-Hamiltonian dynamics, in which the flow is generally compressible (expansive or contractive), with $\vec{\nabla} \cdot \vec{v} \neq 0$. There are two important non-crossing rules that follow directly from this equation (1) a trajectory cannot cross a surface on which the density is zero; (2) the sign of the density riding along the trajectory cannot change.

In the computational algorithm used by Donoso and Martens, the non-local density dependent force acting on a specific trajectory was calculated by fitting Gaussian functions to the known density values using a set of nearby trajectories. A moment method was employed to fit the parameters in the Gaussian exponent. From this fit, derivatives of the density were evaluated, and these were then used to calculate the non-local terms in the equations of motion for each of the entangled trajectories. Over the course of time, however, errors develop in the trajectories due to unavoidable inaccuracies arising from this fitting procedure. To help resolve these issues by completely eliminating the need for function fitting, the DPM was used to propagate DM's "interacting" trajectories.

Before doing this, however, the phase space density, $W(x, t)$, was transformed into C -space using the equation $C = \ln(W)$. In this manner, the initial Gaussian

distribution can be naturally truncated at third order⁷, since it is quadratic in this space.

Using this transformation, the KK equation of motion becomes

$$\partial_t C_{(0,0)} = -\frac{P}{m} C_{(1,0)} + V_{(1,0)} C_{(0,1)} + \gamma \left[1 + p C_{(0,1)} + m k_B T (C_{(0,2)} + C_{(0,1)}^2) \right]. \quad (4.41)$$

Here, the subscript notation described previously is used for the spatial derivatives. The C -transformed KK equation was propagated using the DPM instead of Eq. (4.32) directly. In addition to this equation of motion, the phase space partial derivatives were propagated as well. These were obtained by application of the operator $\partial^{(n+m)} / \partial x^n \partial p^m$ to Eq. (4.41), where n and m are positive integers taking on values up to the truncation order chosen. These equations were not coded explicitly; rather, they were generated directly within recursion loops. The DPM equation of motion for the n th x and m th p partial derivative in this frame is given by

$$\begin{aligned} \partial_i C_{(n,m)} = \sum_{j=0}^n \sum_{i=0}^m b(n,j) b(m,i) & \left(-\frac{P_{j,i}}{m} C_{(n-j+1,m-i)} + V_{(j+1,i)} C_{(n-j,m-i+1)} + \right. \\ & \left. \gamma P_{(j,i)} C_{(n-j,m-i+1)} + \gamma m k_B T C_{(j,i+1)} C_{(n-j,m-i+1)} - \right) + \gamma m k_B T C_{(n,m+2)} + \delta_{n=0,m=0} \gamma \end{aligned} \quad (4.42)$$

Using the velocity components given in Eq. (4.37), the phase space, DPM, Lagrangian equations of motions are given as

$$\frac{dC_{(n,m)}}{dt} = \frac{\partial C_{(n,m)}}{\partial t} + v_x C_{(n+1,m)} + v_p C_{(n,m+1)}. \quad (4.43)$$

The extra terms in Eq. (4.43) always cancel some of the terms in the Eulerian derivative, so that the Lagrangian equations of motion are actually simpler than those calculated by a

⁷ This does not imply that it will be naturally truncated at third order after the propagation has begun.

fixed observer. For example, for the KK equation, the Lagrangian time derivative of the C-density is given by

$$\frac{dC_{(0,0)}}{dt} = \gamma + \gamma m k_B T C_{(0,2)}. \quad (4.44)$$

This is much simpler than its Eulerian version.

To summarize the DPM procedure, Eq. (4.44) and Eqs. (4.43) were propagated in time for all derivative combinations up to a predetermined truncation value. In addition to this, Eqs. (4.37) were also propagated concurrently to update the fluid element/particle positions in time. Because no fitting is required in the DPM, the time-adaptive, Cash-Carp/Runge-Kutta time-integrator was used in the two applications discussed in the next section. This integrator is fourth order accurate in time and is able to adaptively adjust its time-step to decrease the chance of numerical ‘blow-ups’. In the two problems discussed, the DPM will be used to obtain phase space solutions that are comparable to those obtained in DM’s study.

4.4.4. DPM/KK applications

4.4.4.1. *The damped harmonic oscillator*

The first test case is the damped harmonic oscillator (frequency ω), which is frequently used to model vibrational relaxation in a thermal bath. An initial minimum uncertainty Gaussian distribution was constructed with position and momentum widths $\sigma_x(0) = \sqrt{\hbar/2m\omega}$ and $\sigma_p(0) = \sqrt{m\omega\hbar/2}$, a mean energy of $\langle E(t=0) \rangle = 1.0$, and a center at $x(0) = -3$, $p(0) = 0$. The bath temperature was defined to be $k_B T = 0.05$. A total of 625 trajectories were launched from randomly selected points in an ellipse

centered about the initial distribution. To compare with results presented in the DM study, a dimensionless friction constant $\gamma_0 = \gamma \tau_{vib}$ was used, where τ_{vib} is the period of the undamped harmonic oscillator, $\tau_{vib} = 2\pi / \omega$.

Figure 4.5 displays the energy decay of the initial density in the harmonic oscillator potential as a function of γ_0 . Both parts of this figure illustrate how the rate of energy decay is dependent upon the strength of the friction coefficient. The results obtained from the DPM in the low-friction (weakly damped) and high-friction (over-damped) cases were identical to those presented in the DM study.

In Fig. 4.6 the evolution of the non-equilibrium distribution was followed for 4,100 a.u. using $\gamma_0 = 100$. Due to the strong coupling constant in this high friction case, the distribution is expected to reach thermal (momentum) equilibrium with the bath on a very short time scale relative to its spatial relaxation. This can be seen from the figure in the large spread along the momentum axis after only 5 a.u. During this time interval, the motion along x is nearly frozen. As the distribution evolves to longer times, there is coordinate relaxation to the thermal distribution, where the packet is centered about the well minimum. After 4,100 a.u., the final equilibrium phase space distribution is reached.

The results obtained for this potential were most likely exact to machine precision. This is because, for a harmonic oscillator problem, the initial Gaussian distribution was Gaussian for all times, and could be accurately truncated in C-space at

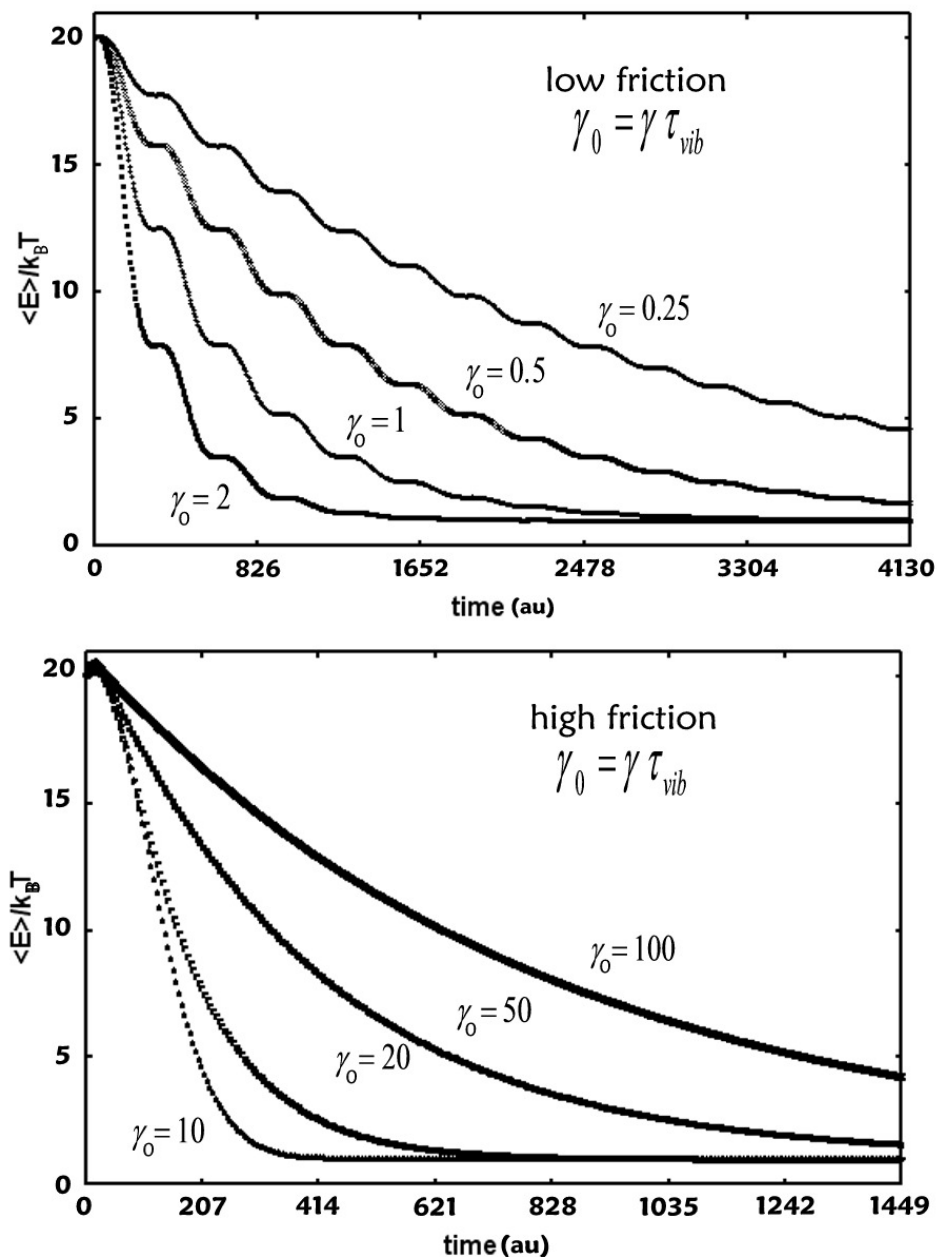


Figure 4.5. Mean energy decay for the Klein-Kramers harmonic oscillator problem. Part (a) displays the energy decay in the low friction limit as a function of the dimensionless friction parameter γ_o , and part (b) displays the same in the high friction limit.

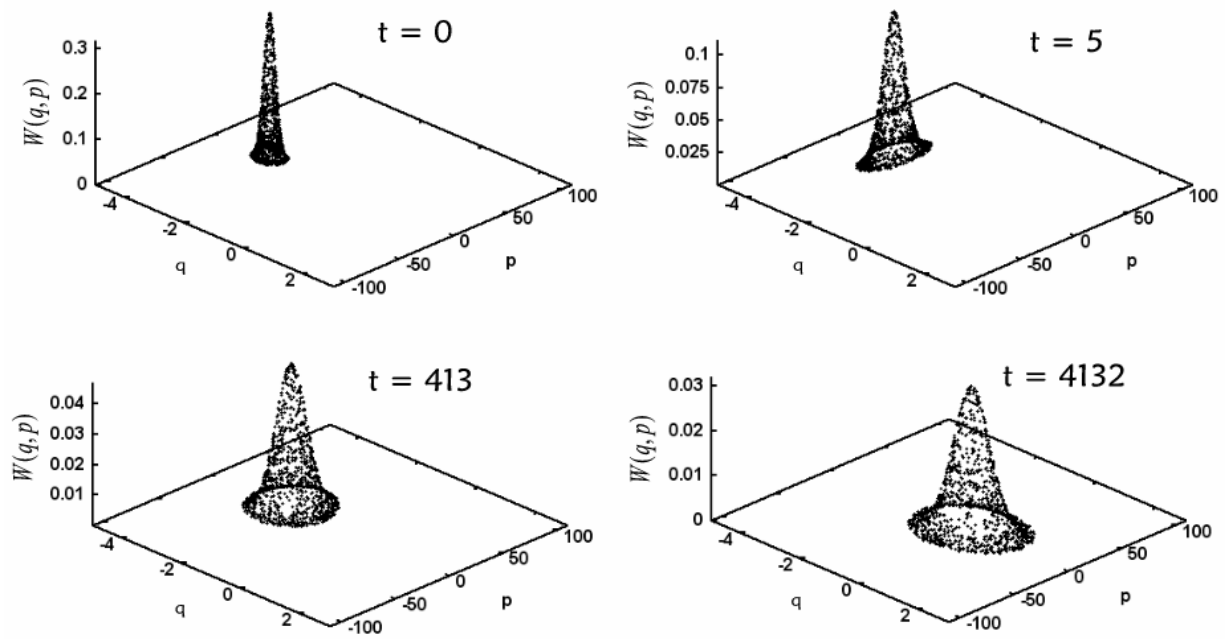


Figure 4.6. Density maps at four time steps for the DPM solution of the Klein-Kramers equation for a harmonic potential ($\gamma_0 = 100$).

third order (since in C-space a Gaussian is represented by a quadratic polynomial). In the next problem, however, this is not so. In fact, the evolving phase space density becomes quite complicated as time progresses.

4.4.4.2. The meta-stable well

This model concerns the thermally activated escape from a meta-stable potential well. It has been frequently used to simulate chemically and physically activated processes in condensed phase chemistry. Kramers [73] thoroughly studied the double well potential and found that the dependence of the escape rate from the potential well on the damping can be separated into three regions. For weak damping, the rate-determining step is the slow activation of the trajectories by the bath, and the rate constant is proportional to the friction constant. When the damping is large, energy is lost to the bath quickly due to the frictional force, and the trajectories move slowly in configuration space. In this case, the escape rate is inversely proportional to the friction constant. In the turnover region, the rate of escape reaches a maximum value. For double well potentials, Kramers derived equations for rate constants in the high and low friction limits under the restriction that the barrier height, V^* , satisfy the condition $V^* \gg k_B T$. These early results have been greatly extended in more recent studies [76-80]. In their study, DM used trajectories to solve the KK equation for the double well potential and obtained good results in comparison to Kramers' analytic derivation of the high and low friction limit rate constants.

In this problem, however, a different meta-stable potential of the form $V(x) = \alpha x^2 - \beta x^3$ will be investigated, with the parameter values $\alpha = 0.01$ and

$\beta = 0.0\bar{6}$. These values were chosen to insure that there is little probability of escape from the well when the interaction with the bath is turned off. This potential has a minimum at $q = 0$ and a barrier height of $V^* = 0.0\bar{3}$ at $x^* = 1$. The bath temperature, $k_B T = 0.035$, is only slightly higher than the barrier maximum. Initially, a minimum uncertainty phase space distribution centered at $(0,0)$ was used. A total of 10,000 trajectories were launched from initial positions selected randomly about the center of the distribution. Fifth-order DPM was used to propagate the equations of motion for a large range of friction coefficients. Using multiquadric radial basis function interpolation (see appendix D), the density within the well ($x < 1$) at each time step was interpolated onto a regular grid, where it could be integrated over p and x using the trapezoid rule.

The results for the low friction limit are displayed in Fig. 4.7 (a). In this limit, the rate of probability decay inside the well increases with increasing friction constant. In the high friction limit, part (b) of this figure, the escape rate decreases as the friction constant is increased, as expected. Because of the coherent motion of the wave packet inside the well, it was difficult to evaluate a rate constant using $W_{\text{well}}(t) = \exp(-k(t - t_o))$ for all times. The reason for this can be seen in Fig. 4.8. At early times, the packet is thermally excited by the bath and spreads in momentum space. After 150 fs, the wave packet has turned and a tail of particles has escaped from the well. After this time, the distribution rotates in phase space until the tail reaches the barrier maximum again. During the time it takes for the tail to reach the barrier again, few particles escape. There is not, therefore, a steady probability decay in time for this problem. For short times, however, the probability decay was exponential, and rate

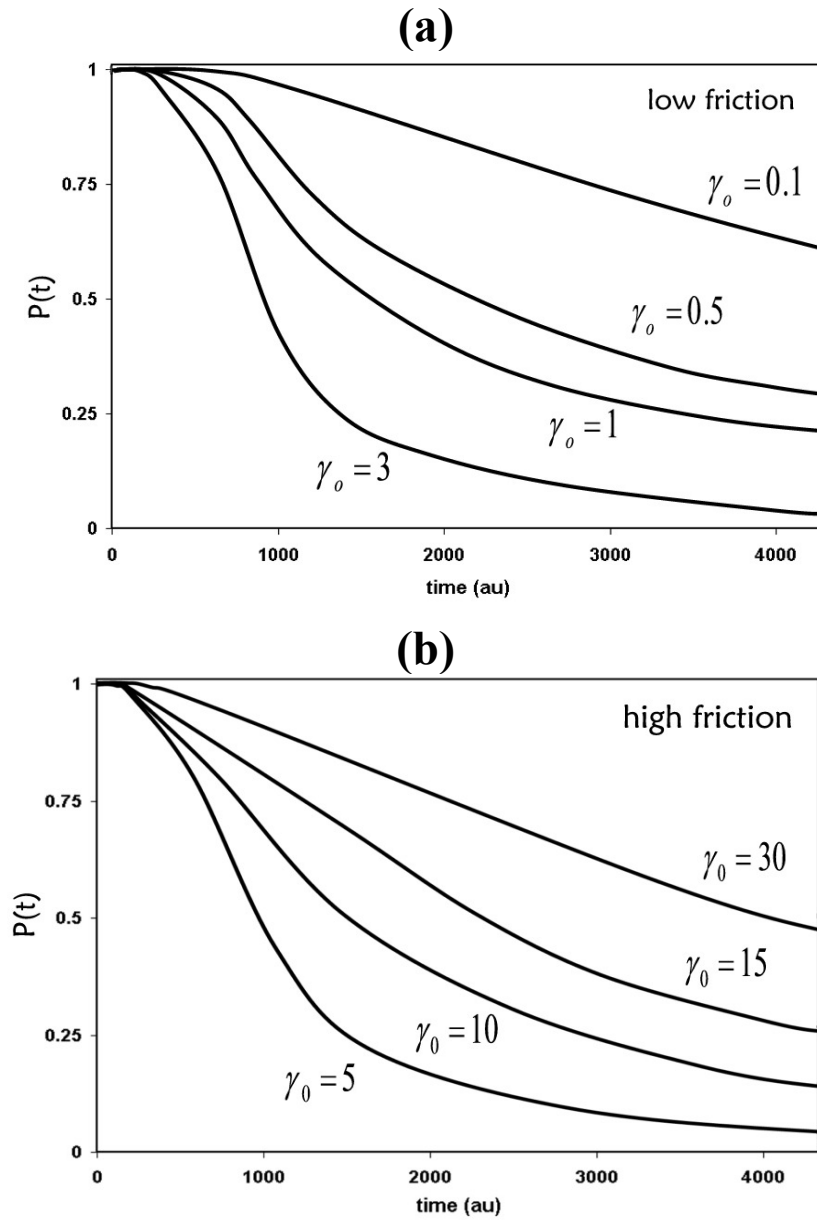


Figure 4.7. This figure displays the time decay of the probability inside the meta-stable well as a function of the dimensionless friction parameter γ_0 . In the low friction limit, the decay rate is *proportional* to the friction parameter as shown in plot (a). In the high friction limit, plot (b), the decay rate becomes *inversely proportional* to γ_0 .

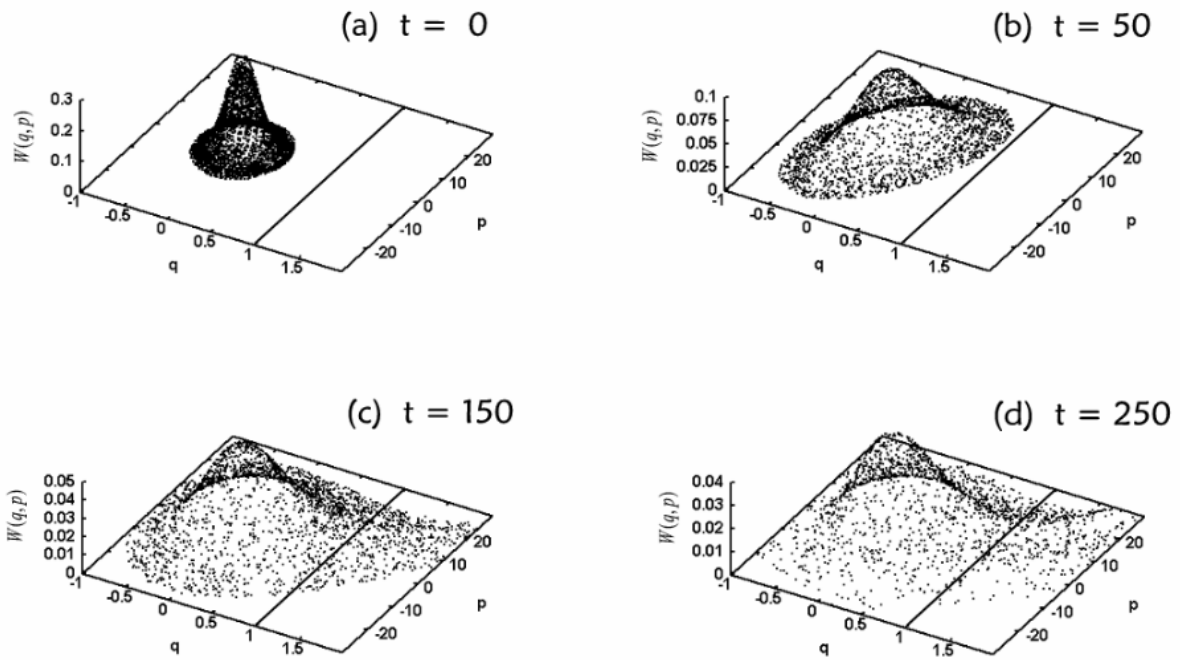


Figure 4.8. This figure displays the time evolution of a phase space Gaussian wave packet in a meta-stable well. The Gaussian is coupled to a thermal bath using a dimensionless friction parameter of $\gamma_0 = 10$. For these results, the DPM was used to integrate the Klein-Kramers equation.

constants were obtained that were reasonably comparable to Kramers' analytic equations (though the condition $V^* \gg k_B T$ was not satisfied). Figure 4.9 displays the exponentially fit rate constants as a function of the dimensionless friction parameter. From this figure it can be seen that the DPM was able to qualitatively capture Kramers' turnover in the unbound meta-stable potential. It should be noted that these calculations were carried out with the DPM for much longer times than 4,500 a.u., however, integration of the density within the well region became intractable, since most of the trajectories exit from the well at early times. At late times, all of the trajectories will eventually escape due to thermal fluctuations.

4.4.5. DPM/KK discussion

In this section a Lagrangian method, very similar to the QTM, was applied to the Klein-Kramers equation of motion for dissipative phase space dynamics. This method is entirely deterministic and provides an alternative to the Langevin method of integrating stochastic differential equations for the system coordinate. The randomness of the Langevin equation is replaced here by a non-local density dependent term that allows interactions between the individual trajectories. This term has similar properties to the quantum potential discussed in chapter three. In this approach, for example, particles are guided by local (classical and dissipative) and non-local forces just as in the QTM. Because of these non-local forces, the particles are allowed to interact, causing a breakdown in the otherwise classical statistical independence of the ensemble. Previously, Donoso and Martens solved the KK using what they called an "interacting

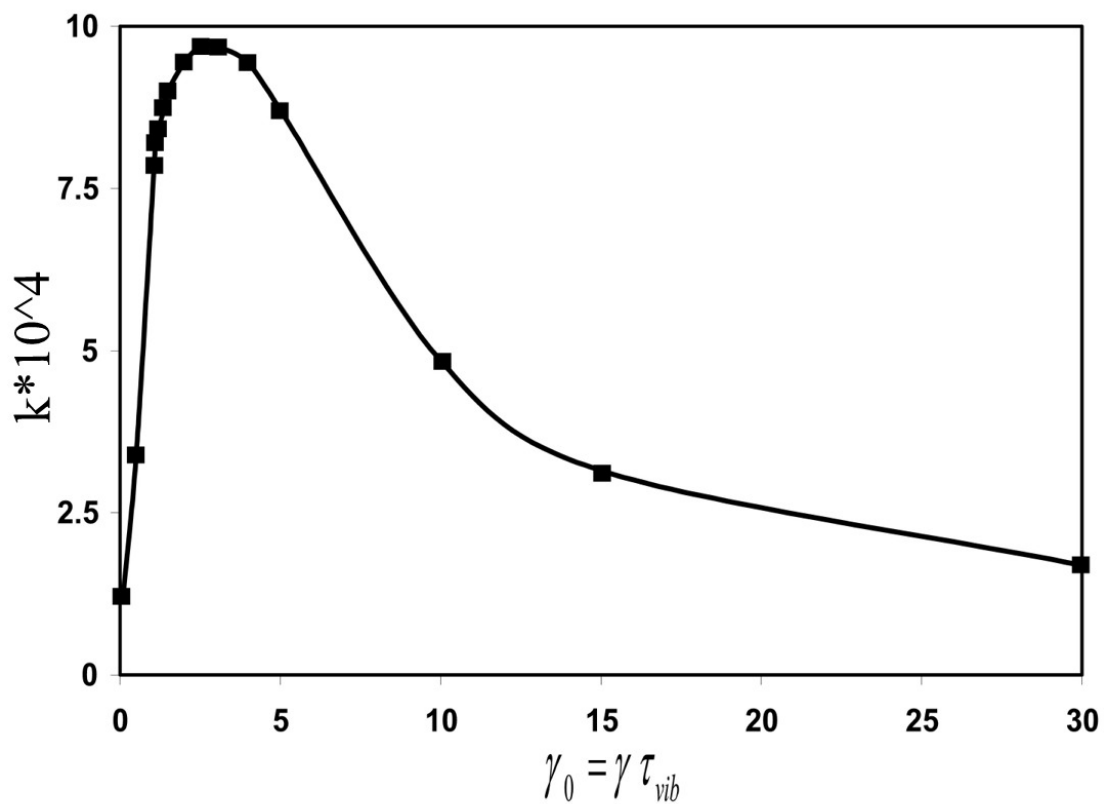


Figure 4.9. This figure plots the rate constant against the dimensionless friction parameter for the cubic potential. The DPM results are shown by solid squares, and the continuous curve is a fit through these points. Kramers' turnover occurs around $\gamma_0 = 2.5$.

trajectory” approach. To obtain the density derivatives needed in the non-local term of the KK, DM used a fitting method called density estimation which involved fitting local Gaussians to the discrete data set. This fitting method gave errors in regions of low density, however, and can be quite time-consuming in multi-dimensions.

As an alternative to DM’s method, the DPM was applied to the KK equation. In the DPM, the Lagrangian trajectories were calculated by solving equations of motion for the phase space density concurrently with its various partial derivatives. In this manner, fitting methods such as density estimation were no longer needed. Using the DPM, trajectories were computed for the relaxation of an oscillator and for the decay of a metastable state, both of which were in contact with a thermal bath. To test the accuracy of these results and other DPM applications to phase space equations of motion, a fixed-grid, finite difference method was recently developed for comparison [70]. Good agreement was achieved between the fixed-grid results and those obtained from the DPM for the KK applications studied in the chapter. Currently, the DPM is being extended to phase space dynamics in higher dimensionality.

4.5. CHAPTER CONCLUSIONS

Trajectory approaches to evolutionary partial differential equations are complicated by the presence of *algorithmic non-locality*. Because of this, spatial derivatives must be evaluated along the time-evolving trajectory. In this chapter, the derivative propagation method for evaluating these derivatives was presented. Rather than the lockstep propagation of an ensemble of linked trajectories, analytic equations of motion for the solution’s partial derivatives were derived, and these derivatives were

propagated along Lagrangian trajectories concurrently with the original PDE itself. In the DPM, the various orders of derivatives are coupled together in an infinite hierarchy, but low order truncations of this system yields useful and accurate approximations. The lowest-order spatial derivatives computed along the trajectory introduce *regional non-locality* into the dynamics. For smooth solutions, or those solutions that do not change much from region to region, this can provide accurate solutions. An enormous benefit of the DPM is that *single* trajectories may be propagated and function fitting is no longer required to compute spatial derivatives that are required in the equations of motion. A number of truncation schemes are possible, but only a limited number have yet to be explored.

In this chapter, the DPM was successfully used to solve the quantum hydrodynamic equations of motion and the classical phase space Klein Kramers equation. For the QHEM, a number of different problems involving different classical potentials have been solved using the QTM, though only two were given in this dissertation. For some of these problems, such as the Eckart barrier, the DPM trajectories ‘blow-up’, but stable trajectories in the product regions allow for calculation of density transmission probabilities. This cannot be done using the QTM or ALE method, since a blow-up in any region of the dynamics will cause the entire ensemble propagation to stop. In phase space, the DPM has been used to accurately solve the Wigner, Husimi, Caldeira-Legget, and modified Caldeira-Legget equations of motion. These examples display the robust ability of the DPM to solve many different initial value PDEs, as long as their solutions are smooth in time and space.

Chapter 5: Conclusions

Traditionally, quantum mechanical wave packet solutions have been calculated using the fixed-grid form of the time-dependent Schrödinger equation. When propagating the fixed-grid TDSE, a grid lattice must be constructed to cover the whole propagation domain. Because of this, the computational cost of numerically integrating the TDSE scales too rapidly with dimensionality and numerical solutions with over three or four degrees of freedom are nearly unsolvable for most problems. This scaling problem is exacerbated when wave function solutions are required in unbound problems, where the wave packet is free to propagate to large distances. In addition to this, if the wave packet has a large energy, a highly resolved lattice is needed to evaluate the kinetic energy operator in the Hamiltonian. This is opposed to low-energy calculations, where a relatively coarse lattice resolution is needed.

The purpose of this dissertation was to describe two new methods for wave packet propagation that alleviate the problems encountered with traditional wave function solvers. Ideally, a robust method should not have computational costs that increase too dramatically in large dimensionality, unbound, and high-energy problems. In addition, any physical insight that can be gained is an added bonus. It may be that more than just a new algorithm for solving the TDSE is required to remedy all of these issues. Indeed, a completely new formalism may be needed. In chapter three of this dissertation, Bohmian mechanics was introduced as a new perspective on an old problem. Although this formalism, in fact, is not really ‘new’, only recently, with the advent of the quantum trajectory method, has it been widely studied and applied. In the QTM, Lagrangian

trajectories are used to integrate the quantum hydrodynamic equations of motion, derived exactly from the TDSE. These trajectories follow regions of significant probability density, thus eliminating the need to calculate solutions in unimportant regions. Also, in Bohmian mechanics, the highly oscillating wave function is not propagated. Instead, the real-valued amplitude and phase functions, governed by the QHEM, are solved. Because these functions are *generally* much smoother in space and time than the wave function, fewer grid points are needed to capture their form. In addition, the Lagrangian trajectories used in the QTM can be analyzed for insight into quantum phenomenon such as barrier tunneling. For example, classical descriptions such as ‘forces’, ‘momentum’, and ‘position’ can be used to describe these moving particles.

The solutions of the QHEM, however, are not always so smooth and easily calculated. In chapter three it was shown that amplitude nodes create singularities, and that in regions around these nodes, the hydrodynamic equations become stiff in time. In addition to this problem, inflation and compression can create inaccuracies in derivative approximations. The results of both of these are termination of the entire ensemble’s propagation. For the first problem, that of stiff time-dependence, better time integrators are needed (maybe implicit ones). The inflation and compression problems, on the other hand, are impossible to handle using the Lagrangian QTM. However, later in this chapter the first novel method was described called the arbitrary Lagrangian-Eulerian method. In this method, particle trajectories are completely governed by the user. Equations of motion for the particle velocities can be derived that guide the particles wherever they are needed. The particles can, for example, flow to regions of large amplitude gradients and curvatures to decrease fitting and interpolation errors. In most cases, however, the ALE

method has been used to sweep out trajectories of equal grid spacings, so that a uniform grid of expanding or contracting spacings is propagated. To move the grid, the edge point velocities are assigned to be completely Lagrangian. This new method was used to solve an uphill ramp problem for which the QTM fails. Although by using the ALE method, all compression and inflation problems are resolved, problems still persist in nodal regions. Since node singularities are not encountered when the TDSE is solved, several hybrid methods have been developed that combine the ALE and quantum trajectory methods with a TDSE propagator. The results presented in these studies seem very promising.

In chapter four of this dissertation, another new method for solving the QHEM was described, the derivative propagating method. In this method, the time-evolution of the phase and amplitude can be computed along discrete trajectories *without requiring explicit input from surrounding points*, even though spatially non-local terms are present in the quantum potential of the QHEM. This is done by propagating the spatial derivatives in time according to their own equations of motion, and this method can be readily applied in either Lagrangian (moving grid) or Eulerian (stationary grid) schemes. The advantage of this approach is that individual trajectories can be propagated, one-at-a-time, and function fitting is not required to evaluate the non-local terms. Regional non-locality can be incorporated at various levels of approximation to ‘dress’ what would otherwise be ‘thin’ locally propagating trajectories.

To show that this method is robust and can be used to solve many evolutionary PDEs, the DPM was used to obtain trajectory solutions to the dissipative, phase space Klein-Kramers equation later in the chapter. Trajectory solutions in two-dimensional

phase space were obtained for the relaxation of an oscillator in contact with a thermal bath and for the decay of a meta-stable state. In addition to this phase space equation of motion, the DPM has been used to propagate the Wigner, Husimi, Caldeira-Leggett, and smoothed Caldeira-Leggett equations of motion. Accurate solutions were obtained for each of these for some simple models.

The three methods discussed in this dissertation share one common theme: nodal problems. This problem is intrinsic to the QHEM, and it cannot be resolved with any propagation method. When nodal regions develop in the QTM and ALE method, breakdown is sure to follow, and the entire propagation is halted. Results past this point cannot be obtained. The same problems occur in the DPM, only in this method, single trajectories that pass this region blow-up, the others remain unaffected. All three of these methods work very well, however, when nodes are not present. Unfortunately, the goal here is to produce an algorithm that will robustly calculate wave packet dynamics on any potential energy surface, with nodes or without, since it is impossible to know if nodal regions will occur beforehand.

The ALE method and DPM are still embryonic, each less than a year old. Currently, these methods are being further developed and extended into higher dimensions. In addition to this, hybrid methods combining the QTM, ALE, DPM, and TDSE are now being developed. Other variables, such as Kendrick's artificial viscosity are being studied as well. Many advances to these methods are being made from a wide range of disciplines. As the algorithms are advanced, increasing attention is given to the numerical advantages and physical insight to be gained from solving the QHEM.

Although the future of these two new methods is uncertain, they will surely serve as stepping-stones for future progress in quantum nuclear dynamics.

Appendix A: Numerical Integration of the Time-Dependent Schrödinger Equation

One of the oldest and most traditional ways of solving for the evolution of a quantum system is to integrate the time-dependent Schrödinger equation directly using a grid-based numerical method. In such routines, the wave function, $\psi(x,t)$ in one-dimension, is represented on a discrete set of np points, $\{x_j\}$, which define a spatial grid (or lattice in multi-dimensions). This spatial grid is usually fixed for all times. After the wave function's initial conditions are given, it is propagated on the grid according to the TDSE. At each time step, a second order spatial derivative is needed for substitution into the kinetic energy term of the Hamiltonian, $-(\hbar^2/2m)\partial^2\psi/\partial x^2$. This second order derivative is often approximated using finite difference (see Appendix B) or finite element methods. If a one-sided difference is used for the time derivative, corresponding to the Euler integrator discussed in section 3.3.2.2, and a second order difference is used for the spatial derivative, the differenced TDSE becomes

$$\frac{\psi_j^{i+1} - \psi_j^i}{\Delta t} = \frac{i\hbar}{2m} \left[\frac{\psi_{j+1}^i - 2\psi_j^i + \psi_{j-1}^i}{(\Delta x)^2} \right] - \frac{i}{\hbar} V_j \psi_j^i, \quad (\text{A.1})$$

where Δx is the constant spacing between adjacent grid points, Δt is the time step used for propagation, and $V_j = V(x_j)$ is the classical potential. In this equation, the subscripts indicate the grid point's position in space, $\psi_j = \psi(x_j)$, and the superscripts indicate the time step of evaluation, $\psi_j^i = \psi(x_j, t_o + i\Delta t)$. By solving Eq. (A.1) for ψ_j^{i+1} , each spatial grid point can be updated by one time step. To evaluate this equation at the grid edges,

suitable boundary conditions must be imposed, since Eq. (A.1) uses centered finite differences for the spatial derivative. A commonly used boundary condition applied to the TDSE is to set the wave function equal to zero at the grid edges (Dirichlet boundary conditions). As long as the grid is sufficiently large enough so that all of the wave function's density remains inside the grid, these boundary condition will be valid. Unfortunately, to enforce these conditions, very large fixed-grids are required, especially for unbound problems.

When the predetermined grid lattice is too small, the edges act as artificial barriers that will cause reflections in the wave function amplitude. In this case, the solutions obtained do not truly reproduce the evolution of the system. Instead, contain unwanted numerical artifacts. To solve this problem, and subsequently use smaller grids, the TDSE is often solved using an *absorbing potential* at the grid edges. In this case, any significant amplitude that reaches the grid edges will be 'eaten'. Of course, the total density probability is no longer conserved with the use of these boundary conditions.

Equation (A.1) can be a stable propagator, depending on the chosen values for Δx and Δt . However, this equation is not unitary, meaning that it does not conserve the systems total probability. To properly difference the TDSE so that it does conserve probability, other time-integrators, such as the implicit Crank-Nicolson [39], should be used. These integrators require the decomposition of a $np \times np$ matrix, where np is the total number of grid points. In two-dimensions, a $np^2 \times np^2$ matrix must be decomposed, and so on. Because of this exponential scaling, implicit methods like the Crank-Nicolson are difficult to apply in multi-dimensional problems.

Throughout this dissertation, many of the results obtained from numerically integrating the QHEM are compared to fixed-grid, wave function solutions of the TDSE. These solutions are very accurate and easy to obtain for one and two-dimensional problems. In our studies, we found that if a high-order explicit time integrator is used, such as the Cash-Carp time-adaptive Runge-Kutta integrator, the total grid probability was conserved to machine precision. This may not be true for all problems, however. In addition to the time adaptive integrator, fourth order finite-differences were used to approximate the kinetic energy's second order spatial derivative for all fixed-grid results presented.

Appendix B: The Finite Difference Method

One of the most widely used methods for solving differential equations on an Eulerian, fixed-grid is the finite difference method. This method, although it can be applied to many types of problems, is especially useful for *regular grids with small spacings*. The advantage of the finite difference method is that matrix solutions are not needed. This is opposed to interpolation and least squares methods, where LU decompositions of coefficient/collocation matrices are often required. In the finite difference method, each of the derivatives in the differential equation are approximated by the appropriate difference equation and solved for explicitly. This is generally an extremely fast procedure.

Assume a set of np discrete function values, $\{f(x_i), i = 1, 2, \dots, np\}$, is given on a one-dimensional grid, $\{x_i\}$, of constant spacing $h = \Delta x$. To obtain the difference equations for the first order spatial derivative of an arbitrary function at grid point x_i , the solution can be expanded in a Taylor series to the nearest neighbor grid points,

$$f(x_{i+1}) = f(x_i) + \frac{\partial f(x_i)}{\partial x} h + \frac{1}{2} \frac{\partial^2 f(x_i)}{\partial x^2} h^2 + \frac{1}{6} \frac{\partial^3 f(x_i)}{\partial^3 x} h^3 + O(h^4), \quad (\text{B.1})$$

$$f(x_{i-1}) = f(x_i) - \frac{\partial f(x_i)}{\partial x} h + \frac{1}{2} \frac{\partial^2 f(x_i)}{\partial x^2} h^2 - \frac{1}{6} \frac{\partial^3 f(x_i)}{\partial^3 x} h^3 + O(h^4). \quad (\text{B.2})$$

If the two expansions are subtracted from one another and subsequently divided by $2h$, a finite difference representation of the first derivative is obtained,

$$\frac{f(x_{i+1}) - f(x_{i-1}))}{2h} = \frac{\partial f(x_i)}{\partial x} + O(h^2). \quad (\text{B.3})$$

If the two expansions are added and divided by h^2 , a finite difference representation for the second order derivative is obtained,

$$\frac{f(x_{i+1}) - 2f(x_i) + f(x_{i-1}))}{h^2} = \frac{\partial^2 f(x_i)}{\partial x^2} + O(h^2). \quad (\text{B.4})$$

In both of these difference equations, the approximations are accurate to second order, since the leading error term is proportional to h^2 . These low order approximations can give excellent results for high-resolution grids or extremely smooth solutions. However, for more accurate approximations, higher order finite differences should be used. These high order schemes require more stencil points to obtain more accurate approximations than those obtained using lower order differences. Throughout this dissertation, fourth order differences will often be used. If the appropriate linear combinations of Eqs. (B.1) and (B.2) are taken, then the fourth order centered difference for the first and second derivatives are

$$\frac{\partial f(x_i)}{\partial x} = \frac{1}{12h} (f(x_{i-2}) - 8f(x_{i-1}) + 8f(x_{i+1}) - f(x_{i+2})) + O(h^4), \quad (\text{B.5})$$

$$\frac{\partial^2 f(x_i)}{\partial x^2} = \frac{1}{12h^2} (-f(x_{i-2}) + 16f(x_{i-1}) - 30f(x_i) + 16f(x_{i+1}) - f(x_{i+2})) + O(h^4).$$

When applying the finite difference method to a differential equation, two common boundary conditions are used. In the first of the two, called Dirichlet boundary conditions, a function is assigned a constant value at the edge points for all times. When this function is assigned to be zero, the conditions are called homogeneous Dirichlet. This condition is the easiest to apply, and it was used for all finite difference applications

in this dissertation. In the second type of boundary condition, the edge points are assigned constant derivatives. This condition will not be used.

Given Dirichlet boundary conditions, the second order finite difference method can be directly applied. However, since the fourth order scheme requires more function values (a representation of its nonlocal character), an asymmetric difference equation is needed for the function values at locations x_2 and x_{np-1} . The difference equations at these locations are given by

$$\frac{\partial^2 f(x_2)}{\partial x^2} = \frac{1}{12h} (10f(x_1) - 15f(x_2) - 4f(x_3) + 14f(x_4) - 6f(x_5) + f(x_6)), \quad (\text{B.6})$$

$$\frac{\partial^2 f(x_{np-1})}{\partial x^2} = \frac{1}{12h} (10f(x_{np}) - 15f(x_{np-1}) - 4f(x_{np-2}) + 14f(x_{np-3}) - 6f(x_{np-4}) + f(x_{np-5})),$$

$$\frac{\partial f(x_2)}{\partial x} = \frac{1}{12h^2} (-3f(x_1) - 10f(x_2) + 18f(x_3) - 6f(x_4) + f(x_5)),$$

$$\frac{\partial f(x_{np-1})}{\partial x} = \frac{1}{12h^2} (3f(x_{np}) + 10f(x_{np-1}) - 18f(x_{np-2}) + 6f(x_{np-3}) - f(x_{np-4})).$$

These equations, along with the centered-difference formulas given in Eq. (B.5) constitute all that is needed to apply the fourth order finite-difference method when Dirichlet boundary conditions are given.

Appendix C: The Moving Weighted Least Squares Method (MWLS)

Many methods of function approximation involve fitting low order polynomials to a discrete set of function values. One of these is the polynomial least squares method. To describe this method, consider a one-dimensional grid, $\{x_i\}$, with np grid points. In this scheme, the function at grid point x_j is expanded to another grid point x_i by the equation,

$$f(x_i) \approx \sum_{j=1}^{nb} a_j p_j(x_i - x_j). \quad (\text{C.1})$$

In the above equation, p_j are the polynomial basis functions centered at x_j , a_j are the coefficients for this basis set, and nb is the total number of basis functions used in the expansion. To solve for the coefficients of Eq. (C.1), a group of $np \geq nb$ grid points closest to the expansion point is chosen. This group of points is called an expansion stencil.

After the stencil is chosen, a least squares analysis [39] is then used to minimize the square of the error between the np expansions and the actual stencil function values to give a maximum likelihood approximation. The minimization equations for this approximation are of the form,

$$\frac{d}{da} \sum_{i=1}^{np} \left\{ \sum_{j=1}^{nb} [a_j p_j(x_i - x_j) - f(x_i)]^2 \right\} = 0. \quad (\text{C.2})$$

The above equation can be given in matrix notation by,

$$(\underline{\underline{P}}^t \underline{\underline{P}}) \underline{\underline{a}} = \underline{\underline{P}}^t \underline{\underline{f}}. \quad (\text{C.3})$$

The coefficients of Eq. (C.3) can then be solved using one of the many linear algebra solvers. One important feature of this matrix equation is that when $\underline{\underline{P}}$ is square, all of the stencil function values are exactly recovered. This procedure is called interpolation. On the other hand, when $np > nb$, the matrix is rectangular and the function values are only approximately fit at the stencil point locations.

For a polynomial least squares method, the one-dimensional truncated Taylor basis

$$B_{1D} = \left\{ 1, \xi, \frac{1}{2}\xi^2, \frac{1}{6}\xi^3, \dots \right\}, \quad (C.4)$$

is frequently used, where $\xi = x - x_i$ and x_i is the expansion point. In two-dimensions, this basis (expanded about (x_i, y_i)) is

$$B_{2D} = \left\{ 1, \xi, \eta, \frac{1}{2}\xi^2, \xi\eta, \frac{1}{2}\eta^2, \frac{1}{6}\xi^3, \dots \right\}, \quad (C.5)$$

where $\eta = y - y_i$. It is easy to formulate a D-dimensional basis using the appropriate Taylor series.

Occasionally all of the particles inside the expansion stencil are not given the same weight when calculating their contribution to the least squares approximation. When different weights are assigned to each particle inside the stencil, the routine is called moving weighted least squares. In this case, the least squares equations are

$$\frac{d}{da} \sum_{i=1}^{np} w(r_{i,j}) \left\{ \sum_{j=1}^{nb} [a_j p_j(x_i - x_j) - f(x_i)]^2 \right\} = 0, \quad (C.6)$$

and the corresponding matrix equation is

$$(\underline{\underline{P}}' \underline{\underline{W}} \underline{\underline{P}}) \underline{a} = (\underline{\underline{P}}' \underline{\underline{W}}) \underline{f}, \quad (\text{C.7})$$

where $\underline{\underline{W}}$ is the diagonal weight matrix. In Eq. (C.6), $r_{i,j}$ is the radial distance between two particles and is given in D-dimensions by

$$r_{i,j} = \sqrt{\sum_{k=1}^D (x_i^k - x_j^k)^2}. \quad (\text{C.8})$$

It is an important fact that in the case of MWLS, square matrices do not interpolate as they do in regular least squares algorithms.

When the MWLS method was used to obtain spatial derivatives in this dissertation, it is called once for every particle, and a stencil of nb particles was used. For each call, a $np \times nb$ matrix was decomposed. The weights used are calculated according to the exponential function,

$$w(r_{i,j}) = \exp(-\gamma r_{i,j}), \quad (\text{C.9})$$

where γ is calculated to give a specific weight at the edge of the stencil.

Appendix D: Radial Basis Function Interpolation

In the last decade or so, radial basis function interpolation has attracted considerable interest due to its ability to interpolate multivariate scattered data relatively accurately [81-118]. In the typical interpolation scenario, a set of np discrete function values, $\{f(\vec{r}_i), i = 1, 2, \dots, np\}$, is given at scattered grid point locations. For a D -dimensional grid, these points are defined as $\{x_i^1, x_i^2, \dots, x_i^D\}, i = 1, 2, \dots, np \in \mathbf{R}^D$. Any interpolation procedure requires that

$$F(\vec{r}_i) = f_i \text{ for } i = 1, 2, \dots, np. \quad (\text{D.1})$$

Here, $F(\vec{r}_i)$ is called the interpolate of the data set $\{f_i\}$. According to Eq. (D.1), the interpolate should exactly represent the function values at the grid point locations. This is opposed to least squares routines, which may only approximately fit function values at these locations.

In radial basis function interpolation (RBF), the interpolate has the form

$$F(\vec{r}_i) = \sum_{j=1}^{np} a_j \phi(\|\vec{r}_i - \vec{r}_j\|), \quad (\text{D.2})$$

where $\|\cdot\|$ denotes the Euclidean norm, and $\phi(\|\vec{r}_i - \vec{r}_j\|)$ are the radial basis functions. The coefficients of Eq. (D.2), \vec{a} , are found by solving the linear system

$$\underline{\underline{\Phi}} \vec{a} = \vec{f}, \quad (\text{D.3})$$

where $\underline{\underline{\Phi}}$ is a collocation matrix with elements $\phi_{ij} = \phi(\|\vec{r}_i - \vec{r}_j\|)$. A few examples of the some well-known RBFs are

$$\begin{aligned}
\phi(r) &= (-1)^m (\delta^2 + r^2)^{\beta/2}, \quad (2m - 2 < \beta < 2m) && \text{multiquadrics,} \\
\phi(r) &= (\delta^2 + r^2)^{-\beta/2}, \quad (\beta > 0) && \text{inverse multiquadrics,} \\
\phi(r) &= (-1)^m r^{2m-2} \ln(r) && \text{thin-plate splines,} \\
\phi(r) &= (-1)^m (\delta^2 + r^2)^{m-1} \ln(\delta^2 + r^2)^{1/2} && \text{shifted thin-plate splines,} \\
\phi(r) &= e^{-(\delta r)^2} && \text{gaussians.} \tag{D.4}
\end{aligned}$$

One of the most popular of these is the multiquadric (MQ) developed by Hardy [92]. Micchelli [103] has proved that the multiquadric is always solvable for distinct data, and that the MQ coefficient matrix of rank np has one positive real eigenvalue and $(np - 1)$ negative real eigenvalues. The multiquadric with $\beta = 1$ is the most widely used and has the form

$$\phi(\|\vec{r}_i - \vec{r}_j\|) = (r_{ij}^2 + \delta^2)^{1/2}, \tag{D.5}$$

where

$$r_{ij} = \left(\sum_{k=1}^d (x_i^k - x_j^k)^2 \right)^{1/2}, \tag{D.6}$$

and where, for the purposes of this dissertation, δ is a parameter that is independent of the basis function. Because the multiquadrics have exponential convergence properties [102] and have been ranked the best in accuracy of all RBFs according to Franke's review paper [86], it was the RBF of choice when this interpolation method was applied.

It is well known that the choice of the parameter in Eq. (D.5) has a large influence on the interpolation ability of the RBF basis [115]. To examine how the δ parameter

affects the shape of the multiquadric basis function, the limit of the multiquadric function can be taken as $\delta \rightarrow \infty$ and $\delta \rightarrow 0$. It can be seen that as δ increases, so does the relative smoothness of the basis function. However, at relatively large values of δ , the function becomes linear near the center and begins to “wash out” the coordinate dependence of the basis function. This can lead to difficulties when trying to obtain distinct entries in the coefficient matrix for better conditioning. On the other hand, as $\delta \rightarrow 0$ the multiquadric begins to have the shape of a cone with a cusp or discontinuous derivative at the center. It is, therefore, easy to visualize why extremely small shape parameters do not give very smooth interpolates and are generally not preferred. Understanding these features and how they relate in the collocation-like scheme of RBF interpolation is vital when considering optimization of the free parameter RBFs. Tarwater [115] has shown that the RMS errors of the interpolates decrease with increasing δ until an optimum value is obtained, and that beyond this optimum value the collocation matrix becomes extremely ill-conditioned, resulting in increasing errors. This optimum shape parameter thus represents the best compromise between the smoothness of the interpolate and the conditioning of the coefficient matrix. Obtaining δ_{opt} continues to be an active area of investigation in RBF interpolation, and many papers have been written on circumventing the ill-conditioning of the coefficient matrix to assuage this task (see [99]). A few of the proposed methods for determining good shape parameters include the following: Hardy’s use of the equation $\delta = 0.815d$, where d is the average distance between the i – th data point and its nearest neighbor [92], Foley’s scheme for selecting δ by minimizing the average root-mean square (RMS) difference between the

multiquadric and inverse multiquadric [85], Kansa and Carlson's method of selecting local shape parameters (shape parameters that are basis function dependent) [98], and lastly, Rippa's method of "cost" minimization [105], which is similar to Goldberg's method of cross-validation [87]. When RBF interpolation was used in this dissertation, the shape parameter was optimized using the initial conditions of the system, and this parameter was used constantly throughout the propagation.

Appendix E: Atomic Units

Oftentimes, it is convenient to use atomic units to describe nuclear motion. These units have been chosen such that all of the fundamental electron properties are equal to one. Given below is a listing of the appropriate atomic unit conversion factors used throughout this dissertation.

Atomic Units and Their SI Equivalents

Quantity	Conversion Factor	Name
Mass	$1 \text{ au} = 9.10939 \times 10^{-31} \text{ kg}$ $= 5.48580 \times 10^{-4} \text{ g/mol}$	Electron mass
Charge	$1 \text{ au} = 1.60218 \times 10^{-19} \text{ C}$	Electron charge
Length	$1 \text{ au} = 5.29177 \times 10^{-11} \text{ m}$	Bohr radius
Energy	$1 \text{ au} = 4.35975 \times 10^{-18} \text{ J}$ $= 27.2114 \text{ eV}$ $= 219475 \text{ cm}^{-1}$ $= 2625.50 \text{ kJ/mol}$ $= 2 \text{ Rydbergs}$	Hartree
Angular Momentum	$1 \text{ au} = 1.05457 \times 10^{-34} \text{ J}$ s/rad	
Time	$1 \text{ au} = 2.42 \times 10^{-17} \text{ s}$	

Using this list, the mass of a proton (1.6726×10^{-27} kg) in atomic units is 1836.15 au, and the reduced mass of the hydrogen molecule (0.503913 g/mol) is 925.260 au. These units are frequently used to simplify the Schrödinger equation. For example, the Hamiltonian for an electron in the Hydrogen atom is given in atomic units by $\hat{H}_{electron} = -(1/2)\nabla^2 - 1/r$. Most of the quantities used in this dissertation are presented in atomic units.

Appendix F: Example QTM Code

Program QTM
Implicit none

```
!-----!  
! This codes numerically integrates the quantum hydrodynamic equations of motion. !  
! For time-integration, the first order Euler method is used. An Eckart barrier !  
! potential is used. !  
! !  
! np = the total number of particles !  
! ntime = maximum number of time steps to propagate !  
!-----!
```

```
integer, parameter :: np = 63, ntime = 150000  
integer i,j,k  
real(kind=16)  
delv(np),c(np),d1x(np),d2x(np),quantum(np),pot(np),x(np),rho(np),vx(np),phase(np)  
real(kind=16) dt,x0,beta,energy,conv,am,vb,xb,wx,xmin,xmax,h,pi,anorm,total_density  
real(kind=16) kinetic_energy,lagrange
```

```
!----- Defining Initial Wave Packet and External Potential Parameters -----!
```

```
! Time step in au  
dt = 0.5d0  
! Center of Gaussian Distribution  
x0 = 0.d0  
! Width of Gaussian Distribution ( $\beta = 1/(4\sigma^2)$ )  
beta = 9.d0  
! Initial translational energy of Wave Packet in  $cm^{-1}$   
energy = 8000.d0  
! Conversion factor from  $cm^{-1}$  to au  
conv = 219474.6d0  
! Translational energy in au  
energy = energy/conv  
! System mass in au  
am = 2000.d0  
! Eckart barrier height in  $cm^{-1}$   
vb = 8000.d0  
! Eckart barrier height in au  
vb = vb/conv
```

```

! Center of Eckart barrier
xb = 6.d0
! Width parameter for Eckart barrier
wx = 5.d0

! Initial grid minimum and maximum
xmin = -0.6d0
xmax = 0.6d0
! Initial particle spacings
h = (xmax - xmin)/dble(np-1)
! Initial particle positions
do i = 0,np-1
  x(i+1) = xmin + i* h
enddo

!----- -- Initializing Wave Packet Propagation -----!

! Normalization for the initial Gaussian distribution
pi = 4.d0*atan(1.d0)
anorm = (2.d0*beta/pi)**(1.d0/4.d0)

! Building Initial Wave Packet
do i = 1,np
  R(i) = anorm*exp(-beta*((x(i) - x0)**2))
  rho(i) = R(i)**2
enddo

! Initial particle velocities (all particles are initially the same velocity)
! These velocities are obtained from the equation  $E_{trans} = \frac{1}{2}mv^2$ .
do i = 1,np
  vx(i) = sqrt(2.d0*energy/am)
  delv(i) = 0.d0
enddo

! Initial phase (action function) for each particle
do i = 1,np
  phase(i) = sqrt(2.d0*am*energy)*x(i)
enddo

! Total initial grid density
total_density = sum(rho)*h

!----- ----- Time Propagation -----!

```

```

do k = 1,ntime
  ! Time in au.
  time = dble(k)*dt
  ! Conversion from au to fs
  tfs = time*0.0242d0

! Defining C -amplitude
do i = 1,np
  c(i) =log(sqrt(rho(i)))
enddo

! Calling subroutine for C – amplitude spatial derivative approximations
call fit_it(np,x,c,d1x,d2x)

! Calculating quantum and classical potentials
do i = 1,np
  ! Quantum Potential.
  quantum(i) = -1.d0/(2.d0*am)*(d2x(i) + d1x(i)**2)
  ! Classical Eckart Potential.
  pot(i) = vb*sech(wx*(x - x0))**2
enddo

! Calculating phase (S) using potentials (Quantum Lagrangian: T-(V+Q))
do i = 1,np
  kinetic_energy = 0.5d0*am*vx(i)**2
  lagrange = kinetic-(pot(i)+quantum(i))
  phase(i) = phase(i) + lagrange*dt
enddo

! Updating particle positions
do i = 1,np
  x(i) = x(i) + vx(i)*dt
enddo

! Calling subroutine for S – amplitude spatial derivative approximations
call fit_it(np,x,phase,d1x,d2x)

! Updating velocities and probability density
do i = 1,np
  vx(i) = (1.d0/am)*d1x(i)
  delv(i) = (1.d0/am)*d2x(i)
  rho(i) = rho(i)*exp(-delv(i)/2.d0*dt)
enddo

```

!----- End Time Propagation -----!
ENDDO

END PROGRAM QTM

Bibliography

1. M. H. Beck, A. Jackle, G. A. Worth, and H. D. Meyer. Phys. Rep. **324**,1 (2000).
2. T. N. Truong, B. Lesyng, D. K. Hoffman, J. Chem. Phys. **96**, 2077 (1992).
3. W. H. Miller, J. Phys. Chem. A. **105**, 2942 (2001).
4. V. E. Madelung, Z. Phys. **40**, 322 (1926).
5. L. de Broglie, C. R. Acad. Sci. Paris. **183**, 447 (1926).
6. D. Bohm, Phys. Rev. **85**, 166 (1952); **85**, 180 (1952).
7. R. E. Wyatt, Chem. Phys. Lett. **313**, 189 (1999).
8. R. E. Wyatt, J. Chem. Phys. **111**, 4406 (1999).
9. R. E. Wyatt, D. J. Kouri, and D. K. Hoffman, J. Chem. Phys. **112**, 10730 (2000).
10. R. E. Wyatt and K. Na, Phys. Rev. E. **65**, 016702-1 (2001).
11. R. E. Wyatt, C. L. Lopreore, and G. Parlant, J. Chem. Phys. **114**, 5113 (2001).
12. C. Lopreore and R. E. Wyatt, Phys. Rev. Letters. **82**, 5190 (1999).
13. C. Lopreore and R. E. Wyatt, Chem. Phys. Letters. **325**, 73 (2000).
14. C. Lopreore and R. E. Wyatt, J. Chem. Phys. **114**, 5113 (2001).
15. C. Lopreore and R. E. Wyatt, J. Chem. Phys. **116**, 1228 (2001).
16. E. R. Bittner and R. E. Wyatt, J. Chem. Phys. **113**, 8888 (2000).
17. E. Bittner, J. Chem. Phys. **112**, 9703 (2000).
18. K. Na and R. E. Wyatt, Phys. Lett. A. **306**, 97 (2002).
19. C. Trahan and R. E. Wyatt, J. Comput. Phys. **185**, 27 (2003).
20. F. Sales Mayor, A. Askar, and H. A. Rabitz, J. Chem. Phys. **111**, 2423 (1999).
21. X. Hu, T. Ho, H. Rabitz, A. Askar, Phys. Rev. E. **61**, 5967 (2000).
22. D. Babyuk, R. E. Wyatt, J. H. Frederick, J. H. John, J. Chem. Phys. **119**, 6482 (2003).
23. D. Nerukh, J. H. Frederick, Chem. Phys. Letters. **332**, 145 (2000).
24. R. K. Vadapalli, C. A. Weatherford, I. Banicescu, R. L. Carino and J. Zhu, Int. J. Quantum Chem. **94**, 1 (2003).
25. R. E. Wyatt, J. Chem. Phys. **117**, 9569 (2002).

26. C. Trahan, R. E. Wyatt, *J. Chem. Phys.* **118**, 4784 (2003).
27. K. H. Hughes, R. E. Wyatt, *Chem. Phys. Letters.* **366**, 336 (2002).
28. K. H. Hughes, R. E. Wyatt, *Phys. Chem. Chem. Phys.* **5**, 3905 (2003).
29. C. Trahan, K. H. Hughes, R. E. Wyatt, *J. Chem. Phys.* **118**, 9911 (2003).
30. E. R. Bittner, *J. Chem. Phys.* **119**, 1358 (2003).
31. J. Z. H. Zhang, *Theory and Application of Quantum Molecular Dynamics* (World Scientific, Singapore, 1999).
32. M. Jammer. *The Philosophy of Quantum Mechanics* (Wiley, New York, 1974).
33. P. R. Holland, *The Quantum Theory of Motion: An Account of the de Broglie-Bohm Causal Interpretation of Quantum Mechanics* (Cambridge University Press, New York, 1993).
34. D. Bohm and B. J. Hiley, *The Undivided Universe: An ontological interpretation of quantum theory* (Routledge, London/New York, 1993).
35. E. J. Kansa, *Comput. Math. Applic.* **19**, 127 (1990).
36. S. Garashchuk, V. A. Rassolov, *Chem. Phys. Lett.* **364**, 562 (2002).
37. S. Garashchuk, V. A. Rassolov, *Chem. Phys. Lett.* **118**, 2482 (2003).
38. S. Garashchuk, V. A. Rassolov, *Chem. Phys. Lett.* **376**, 358 (2003).
39. W. H. Press, S. A. Teukolsky, W. T. Vetterling, and B. P. Flannery, *Numerical Recipes in FORTRAN 90*, (Cambridge, University Press, 1996)
40. H. Braess and P. Wriggers, *Comput. Methods Appl. Mech. Engrg.* **190**, 95 (2000).
41. T. Belytschko and D. Flanagan, *Comput. Methods Appl. Mech. Engrg.* **33**, 669 (1982).
42. J. Donea, S. Giuliani, and J. P. Halleux, *Comput. Methods Appl. Mech. Engrg.* **33**, 689 (1982).
43. C. Hirt, A. Amsden, and J. Cook, *J. Comput. Phys.* **14**, 227 (1974).
44. T. Hughes and W. K. Liu, *Comput. Methods Appl. Mech. Engrg.* **29**, 329 (1981).
45. C. Farhat, C. Degand, B. Koobus, and M. Lesoinne, *Comput. Methods Appl. Mech. Engrg.* **163**, 231 (1998).

46. D. Kershaw, M. Prasad, M. Shaw, and J. Milovich, *Comput. Methods Appl. Mech. Engrg.* **158**, 81 (1998).
47. J. Koo and E. Fahrenthold, *Comput. Methods Appl. Mech. Engrg.* **189**, 875 (2000).
48. W. K. Lui, H. Chang, J. S. Chen, and T. Belytschko, *Comput. Methods Appl. Mech. Engrg.* **68**, 259 (1988).
49. T. Nomura and T. Hughes, *Comput. Methods Appl. Mech. Engrg.* **95**, 115 (1992).
50. B. Palmerio, *Computers in Fluids.* **23**, 487 (1994).
51. B. Palmerio, *Comput. Methods Appl. Mech. Engrg.* **71**, 315 (1988).
52. C. Degand and C. Farhat, *Computers and Structures.* **80**, 305 (2002).
53. C. Farhat, M. Lesoinne, and N. Maman, *Int. J. for Numerical Methods in Fluids.* **21**, 807 (1995).
54. P. A. Gnoffo, *AIAA Journal.* **21**, 1249 (1983).
55. K. Nakahashi and G. Diewert, *AIAA Journal.* **24**, 948 (1986).
56. K. P. Singh, J. C. Newman, and O. Baysal, *AIAA Journal.* **33**, 641 (1995).
57. B. K. Kendrick, *J. Chem. Phys.* **119**, 5805 (2003).
58. D. K. Pauler and B. K. Kendrick, in press
59. E. J. Heller, *J. Chem. Phys.* **62**, 1554 (1975).
60. I. Burghardt and L. S. Cederbaum, *J. Chem. Phys.* **115**, 10303 (2001).
61. I. Burghardt and L. S. Cederbaum, *J. Chem. Phys.* **115**, 10312 (2001).
62. D. J. Tannor and D. E. Weeks, *J. Chem. Phys.* **98**, 3884 (1993).
63. D. J. Tannor, *Introduction to Quantum Mechanics: A Time-Dependent Perspective* ("XYZ", New York, 2004).
64. J. Z. H. Zhang, *Theory and Application of Quantum Molecular Dynamics* (World Scientific, Singapore, 1999).
65. L. D. Landau, E. M. Lifshitz, *Quantum Mechanics: Non-relativistic theory* (Pergamon Press, London, 1958)
66. A. Donoso and C. C. Martens, *Phys. Rev. Lett.* **26**, 223202 (2001).
67. A. Donoso and C. C. Martens, *Int. J. Quantum Chem.* **90**, 1348 (2002).

68. A. Donoso and C. C. Martens, *J. Chem. Phys.* **116**, 10598 (2002).
69. C. Trahan and R. E. Wyatt, *J. Chem. Phys.* **119**, 7017 (2003).
70. C. Trahan and R. E. Wyatt, (in press ??)
71. K. H. Hughes and R. E. Wyatt, *J. Chem. Phys.* (to be submitted).
72. D. A. McQuarrie, *Statistical Mechanics* (Harper & Row, New York, 1973).
73. H. A. Kramers, *Physica* **VII**, 284 (1940).
74. G. D. Billing and K. V. Mikkelsen, *Molecular Dynamics and Chemical Kinetics* (Wiley Interscience, New York, 1996).
75. P. Hanggi, P. Talkner, and M. Borkovec, *Rev. Mod. Phys.* **62**, 251 (1990).
76. E. Pollak, *J. Chem. Phys.* **85**, 865 (1986).
77. E. Pollak, H. Grabert, and P. Hanggi, *J. Chem. Phys.* **91**, 4073 (1989).
78. E. Pollak and P. Talkner, *Phys. Rev. E* **47**, 922 (1993).
79. E. Pollak, A. M. Berezhkovskii, and Z. Schuss, *J. Chem. Phys.* **100**, 334 (1994).
80. A. Arnold, J. A. Carrillo, I. Gamba, and C. W. Shu, to be published.
81. M. D. Buhmann, *Math. Comp.* **70**, 307 (2001).
82. R. E. Carlson and B.K. Natarajan, *Comput. Math. Applic.* **27**, 99 (1994).
83. R. E. Carlson and T. A. Foley, *Comput. Math. Applic.* **24**, 27 (1992).
84. R. E. Carlson and T. A. Foley, *Comput. Math. Applic.* **21**, 29 (1991).
85. T. A. Foley, *J. Appl. Sci. Comput.* **1**, 54 (1991).
86. R. Franke, *Math. Comput.* **48**, 181 (1982).
87. M. A. Goldberg, C. S. Chen, and S. R. Karur, *Eng. Anal. With Boundary Elements.* **18**, 9 (1996).
88. R. L. Hardy, *Comput. Math. Applic.* **41**, 1043 (2001).
89. R. L. Hardy, *Comput. Math. Applic.* **24**, 81 (1992).
90. R. L. Hardy, *Comput. Math. Applic.* **24**, xi (1992).
91. R. L. Hardy, *Comput. Math. Applic.* **19**, 163 (1990).
92. R. L. Hardy, *J. Geophys. Res.* **176**, 1905 (1971).
93. T. Hastie, R. Tibshirani, and J. Friedman, *The Elements of Statistical Learning: Data Mining, Inference, and Prediction* (Springer, New York, 2001).

94. W. Haussmann, K. Jetter, and M. Reimer (eds.), *Recent progress in multivariate approximation. Proceedings of the 4th International Conference on Multivariate Approximation held at the University of Dortmund* (Birkhäuser Verlag, Basel, 2001).
95. E. J. Kansa, *Comput. Math. Applic.* **19**, 127 (1990).
96. E. J. Kansa, *Comput. Math. Applic.* **19**, 147 (1990).
97. E. J. Kansa, *Comput. Math. Applic.* **43**, 501 (2002).
98. E. J. Kansa and R. E. Carlson, *Comput. Math. Applic.* **24**, 99 (1992).
99. E. J. Kansa and Y. C. Hon, *Comput. Math. Applic.* **39**, 123 (2000).
100. W. R. Madych, *Comput. Math. Applic.* **24**, 121 (1992).
101. W. R. Madych and S. A. Nelson, *Math. Comput.* **54**, 211 (1990).
102. W. R. Madych and S. A. Nelson, *J. Approxim. Theory.* **70**, 94 (1992).
103. C. A. Micchelli, *Constr. Approx.* **2**, 11 (1986).
104. N. J. D. Powell, *A review of methods for multivariable interpolation at scattered data points: The state of the art in numerical analysis* (Oxford Univ. Press, New York, 1997).
105. S. Rippa, *Adv. Comput. Math.* **11**, 193 (1999).
106. R. Schaback, *J. Comput. Appl. Math.* **121**, 165 (2000).
107. R. Schaback and Holgar Wendland, *Numer. Algorithms.* **24**, 239 (2000).
108. R. Schaback, *Math. Comp.* **68**, 201 (1999).
109. R. Schaback, *Constr. Approx.* **12**, 331 (1996).
110. R. Schaback, *Creating surfaces from scattered data using radial basis functions. Mathematical methods for curves and surfaces* (Vanderbilt Univ. Press, Tennessee, 1995), p. 477.
111. R. Schaback, *Adv. Comput. Math.* **3**, 251 (1995).
112. R. Schaback, *J. Approx. Theory.* **79**, 287 (1994).
113. R. Schaback, *Native Hilbert spaces for radial basis functions. I. New developments in approximation theory* (Birkhäuser, Basel, 1999).
114. R. Schaback, *J. Comput. Appl. Math.* **121**, 165 (2000).
115. A. E. Tarwater, UCRL – 54670, (1985).

116. Wu, *Solving differential equations with radial basis functions. Advances in computational mathematics* (Dekker, New York, 1999), p. 537.
117. M. Zerroukat, *Eng. Anal. with Bound. Elem.* **23**, 201 (1999).
118. X. Zhang, K. Z. Song, M. W. Lu, and X. Liu, *Comput. Mech.* **26**, 333 (2000).
119. T. Takabayasi, *Prog. Theor. Phys.* **8**, 143 (1952).
120. R. E. Wyatt and R. J. Bittner, *Quantum Dynamics with Trajectories: Introduction to Quantum Hydrodynamics* (being edited).

VITA

Corey Jason Trahan was born in Port Author, Texas on December 1, 1976. He is the son of Alice Marie Trahan and Jerry Lee Trahan. He is one of three children, having two sisters Ashley Rose Trahan and Jerri Lea Trahan. After completing his work at Nederland High School, Nederland, Texas in 1995, he was admitted into Lamar University, where he studied for four years and obtained a Bachelor of Science in both chemistry and physics. In the fall of 1999, Corey entered the Graduate School of Chemistry at the University of Texas. From 1999 until 2003, Corey has worked under his advisor Robert E. Wyatt and has, to date, five publications concerning new numerical methods for solving problems in quantum dynamics.

Permanent address: 1416 Travis Avenue, Nederland, Texas 77627

This dissertation was typed by the author.